



Faculty of Bioscience Engineering

Academic year 2013-2014

Enhanced spatio-temporal modelling of basal water flow beneath ice sheets

Anton Gistelinck

promotors: dr. ir. Jan Baetens & Prof. dr. Philippe Huybrechts

Master thesis submitted in fulfilment of the requirements for the degree of
Master of Science in Bioscience engineering: Land and Water Management

The author and promotors give the authorisation to consult and to copy parts of this work for personal use only. Every other use is subject to the copyright laws. Permission to reproduce any material contained in this work should be obtained from the author.

Ghent, June 2014

The promotor,

The promotor,

The author,

Dr. ir. Jan Baetens

Prof. dr. Philippe Huybrechts

Anton Gistelinck

Dankwoord

Ik kon mijn fascinatie voor ijs van in het begin kwijt bij prof. dr. Philippe Huybrechts en dr. Jan Baetens. Bedankt voor jullie enthousiasme en de begeleiding, de verlichtende gesprekken en de to-do lijstjes. In Oostenrijk, waar mijn passie voor ijs ontstond, groeide ook het idee voor deze thesis, en na EGU was ik verkocht aan de glaciologie. Ik kreeg de kans naar het mooie IJsland te trekken voor de SVALI summer school en werd verder ondergedompeld in de wonderlijk mooie wereld van subglaciale waterstroming met mede-enthousiastelingen. Ook Zwitserland was een hoogtepunt, veldwerk op de Morteratsch en Pers gletsjer, van op het ijs en in de lucht, het mooiste bureau ter wereld. Jonas, Matthias, Harry, Oleg en Heiko, vielen Dank. Heiko, in het bijzonder zou ik jou graag een volledige ijskap cadeau doen voor de hulp bij het modelleren, aan de praat krijgen van ijsmodellen, of de interessante babbels tussendoor. Wouter was dan weer onmisbaar voor het ontwarren van LaTeX, Mathematica en het goede buurmanschap. Voor het waardig vormen van een ingenieur land-en waterbeheer: prof. dr. Marc van Meirvenne, Bernard de Baets, Kris Verheyen en Niko Verhoest, ontzettend bedankt. Aan alle vrienden en familie die deze thesis verlichtten en waarmee ik de mooiste 5 jaar afsluit, merci!



Summary

Basal water flow is a well-known phenomenon under small-scale glaciers and has been shown to be an important factor in steering ice flow through basal sliding and/or sediment deformation, with large-scale ice sheet models accounting for this only recently. In this thesis, an introduction to basal water physics and ice sheet modelling is given. Next, basal water flow under the Antarctic and Greenland ice sheets is modelled through an established basal water model, linked with ice sheet model output, and this on different resolutions. For Antarctica, only basal melting produces water, whereas in Greenland also surface meltwater can reach the bed. At the bed, basal water is assumed to flow in a thin 'Weertman film' layer. This requires a hydraulic potential field without depressions, derived from geometric datasets of the ice sheets with a resolution of 1 km. First of all, these datasets have to be made consistent, which in this case was still a required step for Antarctica. Before applying the basal water model, filling hydraulic depressions has shown to be a particular point of attention. Next, assumptions and effects of resolution or routing algorithms in the basal water model are evaluated, including eventual coupling with ice sheet models. If possible, realistic estimations are made for the water flow under both ice sheets. Finally, a different approach for simulating basal water flow is proposed by setting up a spatially explicit model, which could prove a valuable alternative in the exciting, but still largely uncertain world of modelling ice sheet basal hydrology.

Samenvatting

Basale waterstroming onder ijs is een gekend fenomeen onder kleinere gletsjers en speelt een belangrijke rol voor ijsbeweging, via basaal glijden en vervorming van het onderliggend sediment. Deze kennis wordt echter pas recentelijk meegenomen in ijskapmodellering op grote schaal. In deze thesis wordt een inleiding gegeven tot basale waterstroming en ijskapmodellering. Vervolgens wordt basaal water onder de Groenlandse en Antarctische ijskap gemodelleerd, aan de hand van een reeds ontwikkeld model voor basale waterstroming, en resultaten van een ijskapmodel, en dit op verschillende resoluties. Op Antarctica zorgt enkel basaal smelten voor waterproductie, terwijl op Groenland eveneens smeltwater, gevormd aan het oppervlak, dit basale water kan aanvullen. Een ‘Weertman film’ wordt aanvaard als het mechanisme achter basale waterstroming. Hiervoor wordt de hydraulische potentiaal (zonder depressies) uitgerekend, aan de hand van datasets met de geometrie van de ijskap tot op 1 km resolutie. Deze data dienen eerst consistent gemaakt te worden, wat hier nog diende uitgevoerd te worden voor Antarctica. Nadien bleek het opvullen van depressies in de hydraulische potentiaal een belangrijk aandachtspunt. Vervolgens worden enkele veronderstellingen en effecten van resolutie en routing algoritmes van het water besproken, aangevuld met realistische voorspellingen waar mogelijk. Tenslotte wordt een nieuwe kanaal-gebaseerde aanpak voor het modelleren van basale waterstroming belicht, hiervoor wordt een nieuw ruimtelijk expliciet model opgesteld. Dit is potentieel een interessant alternatief voor de boeiende, maar grotendeels onbekende wereld van de basale hydrologie van ijskappen, en de modellering ervan.

Contents

Dankwoord	i
Summary	iii
Nederlandse samenvatting	v
Contents	ix
List of Symbols	xi
List of Abbreviations	xiii
List of Figures	xiii
List of Tables	xvi
1 Introduction	1
1.1 Problem statement	2
1.2 Outline	2
2 Geography, physics and modelling	5
2.1 Geography of ice sheets	5
2.1.1 Antarctica	5
2.1.2 Greenland	7
2.2 Physics of basal hydrology	9
2.3 Coupling ice flow and basal hydrology	11
2.3.1 Basal sliding	12
2.3.2 Sediment deformation	13
2.4 Thermomechanical ice sheet models	14
2.4.1 Modelling ice flow	14
2.4.2 Huybrechts ice sheet model	15

2.4.3	Modelling ice flow	15
2.4.4	Modelling ice temperature profiles	16
2.5	Basal water model	18
2.5.1	Setup	18
3	Antarctica: basal water model applications	21
3.1	Dataset and processing	21
3.1.1	Geometric data: Bedmap 2	21
3.1.2	Modelled data: basal melting rate	26
3.2	BWM experiments and results	27
3.2.1	Hydraulic depressions: improvements and potential lakes?	28
3.2.2	Fluxes: resolution effect	33
3.2.3	Cold vs. warm-based ice	36
3.2.4	Coupling with ISM	36
3.2.5	Realistic estimations and validation	38
4	Greenland: basal water model applications	41
4.1	Dataset	41
4.1.1	Geometric data: Bamber 2013	41
4.1.2	Modelled data: basal melting rate and surface runoff	43
4.2	BWM experiments and results	44
4.2.1	Hydraulic depressions: potential lakes?	47
4.2.2	Effect of stress partitioning and surface positive feedback	47
4.2.3	Fluxes: resolution and partitioning basal melt and surface runoff	50
4.2.4	Coupling with ISM	53
5	Spatially explicit channel model	55
5.1	Introduction	55
5.2	Implementation	56
5.2.1	Network formation	56
5.2.2	Selection of the growth direction	57
5.2.3	Macroscopic variables	58
5.3	Proof of concept	59
5.4	Channel flow under Central West Greenland	65
6	Discussion and outlook	71
6.1	Discussion	71
6.1.1	Weertman film approach and ISM coupling	71
6.1.2	Antarctica	72
6.1.3	Greenland	72

6.1.4	Spatially explicit model: a new approach to channelized subglacial water flow?	73
	Bibliography	75

List of Symbols

d water film depth (Weertman film)

d_l lake depth

d_{vostok} lake Vostok depth

$\dot{\epsilon}$ ice deformation rate

$\dot{\epsilon}_s$ sediment deformation rate

G geothermal heat flux

H ice thickness

c_i heat capacity of ice

k_i heat conductivity of ice

k_i ice thermal conductivity

L_f latent heat

\dot{M}_b basal melting rate

\dot{M}_s surface mass balance

N effective pressure ($P_i - P_w$)

P_i ice overburden pressure

P_w water pressure

ϕ hydraulic potential

ρ_i ice density
 ρ_o ocean water density
 ρ_w fresh water density
 T temperature
 T_{pmp} pressure melting point
 τ_b basal shear stress/basal drag
 τ_d driving stress
 τ_s shear stress on sediment
 \bar{U} vertically averaged ice velocity
 U_b basal ice velocity or basal sliding speed
 U_s ice surface velocity
 u_w water flow velocity (Weertman film)
 z_b bedrock elevation
 $z_{b,grl}$ grounding line bedrock elevation
 z_s ice surface elevation

List of Abbreviations

ADI Alternating direction implicit (numerical method)

AIS Antarctic ice sheet

BWM Basal water model

EAIS East Antarctic ice sheet

GHF Geothermal heat flux

GrIS Greenland ice sheet

IPCC Intergovernmental Panel on Climate Change

ISM Ice sheet model

LGM Last Glacial Maximum

NEGIS North-East Greenland ice stream

PDD Positive degree day

PDF Probability distribution function

PIG Pine Island glacier (WAIS, Amundsen Coast)

pmp Pressure melting point

SEM Spatially explicit model

SIA Shallow ice approximation

SLR Sea level rise

SMB Surface mass balance

WAIS West Antarctic ice sheet

List of Figures

1.1	Satellite images of Antarctica and Greenland	2
2.1	Ice flow and glaciers in Antarctica	7
2.2	Ice flow and glaciers in Greenland	8
2.3	Film-based continuous vs. discrete channelized water flow	10
2.4	Scheme of stresses acting in ice sheets	12
2.5	Overview and components of the Huybrechts ISM	17
3.1	BEDMAP2: improvements and coverage	22
3.2	BEDMAP2: adaptations at Lambert glacier	25
3.3	ISM experiments output, Antarctica	26
3.4	Basal melt rate, Antarctica (Shapiro GHF)	27
3.5	Basal water model output, 20 km, Antarctica, uniform basal melt	28
3.6	Routing: 4 vs. 8 neighbours	30
3.7	Planchon depression filling algorithm	31
3.8	Depression filling problem at Lake Vostok	32
3.9	Potential lakes under Antarctica	34
3.10	Fluxes on different resolutions, Antarctica	35
3.11	Water fluxes: warm vs. cold-based ice	37
3.12	ISM geometries in BWM	38
3.13	ISM geometries in BWM	38
4.1	Greenland geometric data: Bamber 2013 data and mask	42
4.2	ISM experiments output, Greenland	43
4.3	Runoff and basal melt rate (Shapiro GHF) Greenland	44
4.4	Basal water model output, 1 km, Greenland, uniform basal melt	46
4.5	Potential lakes under Greenland, focusing on the North-East	48
4.6	Smoothed surface vs. original	50
4.7	Fluxes on different resolutions, Greenland	52

4.8	ISM geometries in BWM	54
5.1	Intersection algorithm: procedure and convergence	57
5.2	Testing intersection algorithm	58
5.3	Sampling directions in the SEM	59
5.4	Linear slope, uniform sampling, effect of angular tolerance	61
5.5	Linear slope, PDF sampling, effect of r	62
5.6	Other test geometries, PDF sampling	64
5.7	Study area: Central West Greenland	65
5.8	SEM sampling experiments, Central West Greenland	67
5.9	SEM output Central West Greenland, PDF, radius 2 km	69
5.10	BWM output, Central West Greenland	70

List of Tables

3.1	Improvements for filling depressions in the hydraulic potential, 20 km resolution, Antarctica.	31
3.2	Depression-filling results and further improvements for all resolutions, Antarctica	32
3.3	Total potential water flow under cold-based ice for different resolutions, Antarctica	36
4.1	Depression-filling results and further improvements for all resolutions, on Greenland	47

CHAPTER 1

Introduction

The cryosphere encloses all components of the Earth's surface where frozen water is present, contributing directly to the global water cycle and climate. It is also a sensitive indicator of climate change through melt, changing snowfall patterns and positive albedo feedback loops. According to the Intergovernmental Panel on Climate Change (IPCC), the last three decades, air temperatures have been the highest since 1850, and might have risen from the coldest to the warmest levels of the Holocene within the past century (Marcott et al., 2013), causing major changes for the cryosphere. In alpine regions, the natural water towers are melting or lacking snowfall, whilst in the Arctic, polar bears are losing their frozen habitat (Lenaerts et al., 2013; Abermann et al., 2009). With an average 20th century glacier and ice sheet mass loss of over $650 \cdot 10^{12}$ kg/year, large meltwater production and thermal ocean expansion have risen sea levels up to 0.19 m since 1901, with a current rate of 3.2 mm/year (IPCC, 2013). The two major components of the cryosphere are the Antarctic ice sheet (AIS) and Greenland ice sheet (GrIS), together covering $15 \cdot 10^6$ km² and housing a potential 63 m of sea level rise (SLR) (Fig. 1.1). Due to their longer response time, the ice sheet mass losses will get more significant in the future. Hence, improving our understanding of the physics of the cryosphere was never more important.

Subglacial hydrology describes the processes in the presence of water beneath ice masses. Mechanisms behind the flow of basal water and the interaction with the ice above often remain uncertain, although they can impact ice flow and thus mass balances significantly through space and time (Fudge et al., 2009; Harper et al., 2005; Sundal et al., 2011). Recent progress in the field of remote sensing and data collection via boreholes, together with theoretical process-based modelling can help to better understand these fascinating basal processes (Irvine-Fynn et al., 2011). This thesis aims at summarizing and improving this understanding through modelling, focusing on basal water flow beneath large-scale ice sheets.

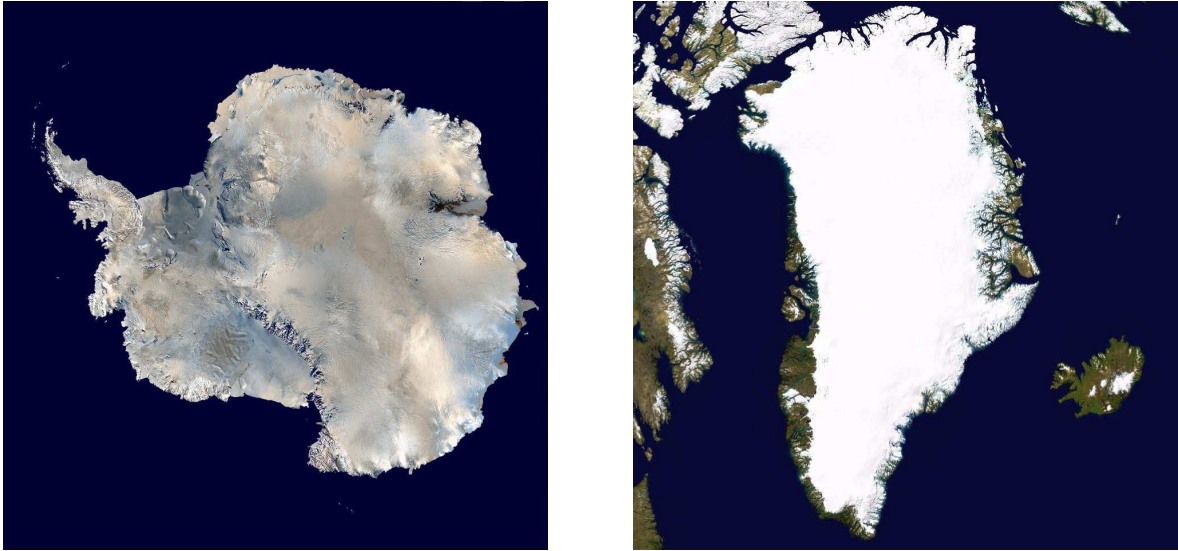


Figure 1.1: Satellite images of Antarctica (2006) and Greenland (2005) (courtesy of NASA).

1.1 Problem statement

The physics of basal hydrology under ice sheets is known through some observations and experiments. In modelling, basal hydrology has only recently raised interest. Long before, large scale ice sheet models (ISMs) had proven useful in mimicking the dynamics of the AIS and GrIS, and they still play a major role in climate and sea-level projections (IPCC, 2013). On a continental scale, only a handful attempts have been made to couple ISMs with basal hydrology, most of them empirically based. With new theoretical insights and bedrock elevation data available, this thesis aims at finetuning an existing basal water model (BWM) for the Antarctic (AIS). Furthermore, it is adapted and applied to the Greenland ice sheet (GrIS) for the first time. This is done keeping in mind a potential coupling with large scale ice sheet models (ISMs). Since much uncertainty still surrounds subglacial hydrology on an ice-sheet scale, a spatially explicit model was set up as a basis to model subglacial channel formation under ice sheets.

1.2 Outline

In Chapter 2, an overview will be given of the dynamics of the Greenland and Antarctic ice sheets, including their relevant subglacial processes. After a brief introduction in the general physics of basal hydrology, the Huybrechts ISM and the BWM used here are introduced. Chapter 3 treats the Antarctic ice sheet and starts with an overview of the data. Some corrections had to be done before applying the BWM. Experiments were done ranging from the setup of the BWM to validation. In Chapter 4, Greenland is treated similarly, with an

overview of the data and first applications of the BWM, including some test scenarios and realistic simulations. Finally, Chapter 5 sets out a new approach to basal water flow, based on spatially explicit modelling of network formation. This approach is applied on Central West Greenland.

CHAPTER 2

Geography, physics and modelling

2.1 Geography of ice sheets

An ice sheet is a continental-scale body of ice where ice flow is determined through the geometry of the ice sheet itself. This distinguishes ice sheets from glaciers, whose ice flow is governed by the underlying topography (Marshall, 2011). The Antarctic and Greenland ice sheets are governed by surface, englacial and basal processes, whereby the relative importance of these processes differs between both ice sheets. Whilst their surface mass balance (SMB, \dot{M}_s) is relatively well studied, in and under a typical 2000 m of ice, far less is known about key processes. Expression on the ice surface of subglacial channels and lakes or local stick-slip behaviour, as well as recently observed large scale events, such as stoppage, acceleration or rapid thinning of ice streams demand better understanding of basal physics. In general, as more meltwater is produced and outlet glaciers that are currently governing mass balances are retreating, basal hydrology might play an increasingly important role for the AIS and GrIS, and future sea level rise (Joughin et al., 2013; Cuffey and Paterson, 2006).

2.1.1 Antarctica

The Antarctic ice sheet (AIS) covers $13.924 \cdot 10^6 \text{ km}^2$, with a total ice volume estimated at $26.92 \cdot 10^6 \text{ km}^3$, corresponding to a potential SLR of 58.3 m. Grounded ice is surrounded with $1.6290 \cdot 10^6 \text{ km}^2$ of floating ice shelves (Fretwell et al., 2013). With circumpolar winds and ocean currents isolating the continent, stability in a warming world is more likely than for Greenland. Except for some coastal regions, Antarctica receives only a few cm of snow annually, making it largely a desert. 80 % of grounded ice drains to ice shelves (Fig. 2.1), causing calving and basal melting to be the dominant factors in its mass balance (Pritchard et al., 2012). This basal melting produces basal water, the dominant process of the AIS in the light of this thesis. Currently, the AIS is losing ice at $160 \cdot 10^{12} \text{ kg/year}$, causing 0.43 mm of SLR

in the last 3 years (McMillan et al., 2014). Although precipitation is estimated to increase over the next century, the net ice loss will likely increase (Joughin et al., 2014).

In general, Antarctica is divided in a land-based East Antarctic ice sheet (EAIS) with a mean bed elevation of 15 m and a marine-based West Antarctic ice sheet (WAIS) with a mean bed elevation of -440 m, roughly separated by the Transantarctic mountains (Rignot and Thomas, 2002; Cuffey and Paterson, 2006).

The larger and more homogeneous EAIS lies largely above sea level, separated from warm ocean water, holding 53.3 m of potential SLR. Ice flow is largely dependent on topography, with faster ice streams in some topographic throughs (Siegert, 2008). Ice thickness averages around 2100 m, with a maximum of 4776 m at the Astrolabe Subglacial Trench. Under the smooth ice surface, large bed depressions can collect water and form subglacial lakes, with the most famous one, Lake Vostok, covering 15690 km². Some of these lakes, like Lake Vostok for example are hydrologically isolated since they were formed during inception of the ice sheet, and might give important insight into early life forms. Others are hydraulically connected via periodic drainage, up to catastrophic floods scouring landscapes such as the ice-free Labyrinth in Victoria Land (estimated discharge up to $2 \cdot 10^6$ m³/s) (Bell et al., 2007; Lewis et al., 2006). The WAIS exhibits more clearly the link between basal water and ice flow and has a bigger influence on AIS mass balance, whilst only housing 4.3 m of SLR. The WAIS has been shown to be inherently more unstable than the EAIS, mainly because of its topography below sea level, some retrograde bedrock slopes and its proximity to warm ocean currents, making it very sensitive to ocean temperature changes (Siegert, 2008; Rignot and Thomas, 2002; Gudmundsson et al., 2012). Of the 160 10^{12} kg loss every year, the WAIS accounts for 134 10^{12} kg (McMillan et al., 2014). Ocean-induced basal melting of buttressing ice shelves at the grounding line causes ice loss to be transmitted inland through fast flowing outlet glaciers. The grounding line is defined as the transition line between grounded and floating ice. A retreat of outlet glaciers means a retreat of the grounding line. This ocean-induced dynamic thinning of outlet glaciers is responsible for most WAIS mass loss (Pritchard et al., 2009, 2012). The Amundsen sea sector, exhibiting a retrograde bed, has been shown to be particularly sensitive to this ocean-induced melting, with an irreversible retreat for big ice streams like Thwaites and Pine Island glacier (Fig. 2.1) likely on the way, as shown by both observations and modelling (Joughin et al., 2014; Rignot et al., 2014).

Most WAIS ice streams have a fully thawed bed, but basal water might not be the dominant trigger in dynamic thinning since this would thicken the ice shelves as more ice would be carried to the ocean. However, highly pressurized basal water was observed in boreholes, and the existence of channels has been shown under WAIS ice streams. Furthermore, lakes in the WAIS can initiate ice streams like the Recovery Glacier, whilst hydraulic pathways and their migrations could stop ice streams, which might have happened under Kamb Ice Stream, in turn activating neighbouring ice streams (Wel et al., 2012).

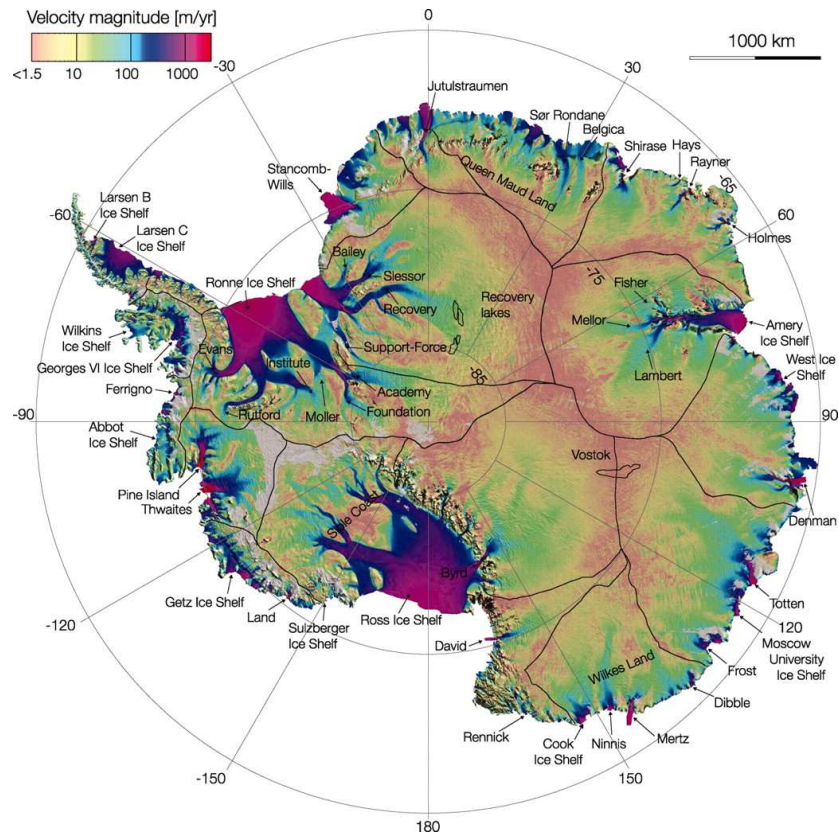


Figure 2.1: Ice flow velocities and glaciers in Antarctica (Rignot et al., 2011) Circled in red are the rapidly dynamically thinning Thwaites and Pine Island Glacier

2.1.2 Greenland

Greenland houses about $2.96 \cdot 10^6 \text{ km}^3$ of ice, or 7.36 m of potential SLR, mainly stored in the Greenland ice sheet (GrIS). The climate is strongly affected by nearby land masses and ocean currents like the Gulf Stream and the North Atlantic circulation, giving rise to an average accumulation rate of about 0.3 m/year. With a fairly constant annual precipitation and increasing summer melting occurring up to over 90 % of the ice-sheet, ice is lost primarily through seasonal surface runoff and ice discharge (van den Broeke et al., 2009). Like the WAIS, Greenland has dynamically thinning outlet glaciers such as the Jakobshavn Glacier (Fig. 2.2), where stresses are rapidly transferred up to 100 km inland (Joughin et al., 2008). Furthermore, 2% of the GrIS lies below sea level, and an unstable and larger ocean thermal forcing (compared to Antarctica) poses uncertainty for the future of the GrIS. Currently, Greenland is losing mass at $215 \cdot 10^{12} \text{ kg/year}$.

Greenland exhibits a different basal hydrology than the AIS, with more seasonal variation (Sundal et al., 2011). Next to meltwater produced at the bed, surface meltwater can flow englacially through moulins or crevasses to the bedrock (Kohler, 2007; Irvine-Fynn et al.,

2011). The drainage of supraglacial lakes can lubricate the bed on a large spatial extent and cause sudden glacier surges (Joughin et al., 2013). Subglacial lakes on the other hand are rare, as a consequence of steeper surface slopes pushing the water out (Bamber et al., 2013b). Just as the for the AIS, some ice streams might be governed by basal hydrology on their onset, which could be the case for the Petermann Glacier and the North-East Greenland Ice Stream (NEGIS) (Fig. 2.2).

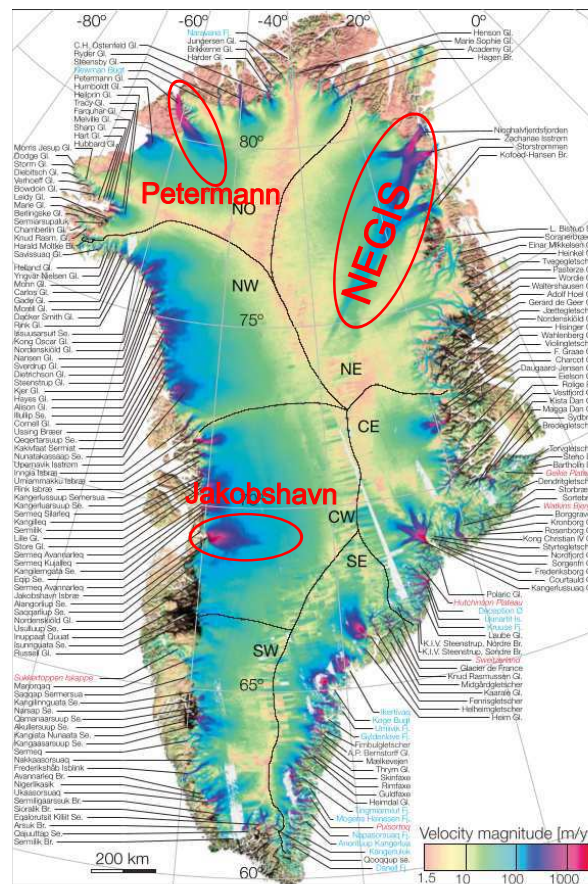


Figure 2.2: Ice flow velocities and glaciers in Greenland (Rignot and Mouginot, 2012)

New findings show evidence of potential water pathways under both the AIS and GrIS. For Greenland, high resolution radio-echo sounding detected lakes even under cold-based ice, where temperatures are too low to melt water (Palmer et al., 2013). In Northern Greenland, a 200 km long canyon ending near Petermann Glacier was recently observed, and might have been draining water from far inland for millennia (Bamber et al., 2013b). In Antarctica, on the Filchner-Ronne ice shelf, a 250 m high melt plume cavity was seen through surface expression (Fig 3.14b). The cavity originated from a meltwater channel a few m wide reaching the grounding line (Le Brocq et al., 2013). These phenomena are just some examples, indicating the urge for a better physical understanding of basal hydrology and its dynamics under large scale ice sheets.

2.2 Physics of basal hydrology

On ice sheets, water is naturally present in its solid form, so heat is required to obtain liquid water. Heat originates through heat sources, including latent and geothermal heat, the latter related to the Earth's crust thickness. Another heat source can be supra-or englacial water reaching the bed via moulins, crevasses and hydrofracturing, but this is negligible. This heat transferred through advection (negligible in this base layer) and conduction. Together, these processes lead to the following equation for the basal melt rate \dot{M}_b at the ice-bed interface:

$$\dot{M}_b = - \left(\left(\frac{\partial T}{\partial z} \right)_b \frac{k_i}{L_f} - \frac{G}{L_f} - \frac{\tau_b \mathbf{U}_b}{L_f} \right), \quad (2.1)$$

with T temperature [K], z the depth in the ice column [m], k_i the ice thermal conductivity [W/mK], L_f the latent heat of melting [J/kg], G the geothermal heat flux [W/m²], τ_b the basal shear stress [Pa] and \mathbf{U}_b the basal sliding velocity [m/s]. The minus sign is there since melting requires heat. The temperature gradient considered is between the ice at the bed and the temperature of the water, assumed to be at pressure melting point (T_{pmp}), given by

$$T_{pmp} = 273.15\text{K} - C_T \rho_i g H, \quad (2.2)$$

with $C_T = 0.0742 \cdot 10^6 \text{K/Pa}$, ρ_i the ice density [kg/m³], g the acceleration of gravity (9.81m/s²) and H the ice thickness [m]. Beds are classified as either warm, where sufficient heat is present to melt water, or cold, where temperature remains below T_{pmp} and available water can re-freeze.

Once formed, subglacial water flows in the direction of the hydraulic potential ϕ [Pa] (Shreve, 1972):

$$\phi = \rho_w g z_b + P_w, \quad (2.3)$$

with ρ_w fresh water density [kg/m³], z_b the bedrock elevation [m] and P_w the water pressure [Pa]. Since water pressure is only relevant when compared to ice overburden pressure P_i , the effective pressure N [Pa] is commonly used:

$$N = P_i - P_w \quad (2.4)$$

This parameter has a great importance in drainage morphology and possibly ice flow. For large scale applications, N is often considered to be 0 Pa, meaning that $P_w = P_i = \rho_i g H$. This has also been observed under some WAIS ice streams (Clarke, 2005). Calculating the gradient of the hydraulic potential $\nabla \phi$ and considering $N = 0$ Pa, the surface slope ∇z_s exerts a 10 times stronger influence, when compared to bedrock slope ∇z_b :

$$\nabla \phi = (\rho_w - \rho_i) g \nabla z_b + \rho_i g \nabla z_s, \quad (2.5)$$

It therefore requires large backsloped beds to trap water in subglacial reservoirs and, as a consequence, ice sheets tend to expel subglacial water rather than store it.

The assumption of $P_w = P_i$ only implies an upper bound on water pressures. Higher water pressures would lift the base of the ice, which can only happen during short-period outbursts. A lower bound, $P_{w,min}$, can be found by assuming water has to reach the glacier terminus at the grounding line bedrock elevation ($z_{b,grl}$) and flow out into ocean water with density ρ_o [kg/m^3] (Van der Veen, 2013):

$$P_{w,min} = -\rho_w g z_b + g z_{b,grl} (\rho_w - \rho_o) \quad (2.6)$$

The real value of N strongly depends on the architecture of the drainage system, where two classes are commonly described in literature. On the one hand, a diffuse or continuous approach consisting of cavities, films or aquifers, and on the other hand, a discrete approach involving channels or canals (Fig. 2.3) (Cuffey and Paterson, 2006). They are further split up into:

1. Channels, varying between two end-members: R channels (Röthlisberger), incised into the ice and N channels (Nye), incised into the bedrock.
2. Canal flow through soft sediment beds, similar to overland meandering
3. Sheet flow in a thin water film
4. Linked cavities, where small cavities are linked through orifices
5. Groundwater flow in the soft sediment



Figure 2.3: Morphology of film-based continuous water flow vs. discrete channelized water flow

An important feature is that R channels lead to an arborescent network, where larger channels collect water from smaller channels. This is because higher discharges cause more melting of channel walls, and the increase in ice creep closure needed to balance this growth requires lower water pressures resisting the ice creep. In contrast, N-channels and cavities give rise to a stable network (higher discharge=higher pressure) (Wingham et al., 2006; Creyts and Schoof, 2009).

Which mechanism dominates depends on the properties of the bed, the ice flow and the water flow itself. Canals and aquifer flow are found in soft beds, whilst hard beds facilitate

film and channel flow. A high bed roughness can cause cavity formation in the presence of sufficient ice flow (around 10 m/year) to keep the cavities open. Water flow will counter ice creep closure through melting of channel walls or sediment erosion. The water pressure P_w could temporarily lift the ice (hydraulic jacking) and create a continuous film flow (Schoof, 2010; Irvine-Fynn et al., 2011). Interaction with overlying ice in turn depends strongly on the drainage morphology again.

Finally, on alpine glaciers, a transition has been observed in the melting season from a diffuse to a more efficient discrete transport on a daily and seasonal timescale (Mair et al., 2002). Icelandic subglacial floods or jökulhlaups also show both fast-rising discharge hydrographs, indicating discrete drainage, or slowly rising continuous drainage hydrographs (Magnusson et al., 2007). As such, which mechanism is dominating not only varies through space, but also through time. Such a time-dependency might be important in Greenland, whereas less seasonality is expected in Antarctica. Time-dependency might be on a multi-year to millennial time scale. Drainage switches in key sectors like Siple Coast (AIS) and the NEGIS (GrIS) have been modelled and might be crucial in understanding historic and future ice flow dynamics (Le Brocq et al., 2009). The approach used here involves a steady-state Weertman-film, or a thin continuous water film.

In some regions, where the potential gradient shows depressions, basal water can stagnate and form subglacial lakes. In Greenland, the bed is often too rough and surface slopes too steep for large water bodies to accumulate. In Antarctica however, especially the EAIS, subglacial lakes are common and well studied. Based on the hydraulic potential ϕ (Eq. 2.3), about 4% of the bed could be covered with subglacial lakes, whereas the latest inventory showed 379 lakes (Wright and Siegert, 2012). For the GrIS, only 0.9% could potentially be a subglacial lake (Bamber et al., 2013b). For both ice sheets, modelling of the Last Glacial Maximum (LGM, -21000 years) and the subsequent deglaciation indicates an increased number of lakes under a retreating ice sheet, possibly because of smoother surface gradients (Livingstone et al., 2013).

2.3 Coupling ice flow and basal hydrology

Ice movement consists of internal ice deformation $\dot{\epsilon}$ (given by Glen's flow law 2.17), basal sliding \mathbf{U}_b and sediment deformation $\dot{\epsilon}_s$. Both deformation terms here indicate a rate or deformation per time unit, expressed in m/ms. Resistance to ice flow is provided by basal drag or basal shear stress τ_b [Pa](global and local sticky spots), side-valley drag and longitudinal drag or horizontal elasticity of the ice (Fig. 2.4). The presence and properties of basal water can lower the basal shear stress τ_b and contribute to ice movement through increasing basal sliding and/or sediment deformation.

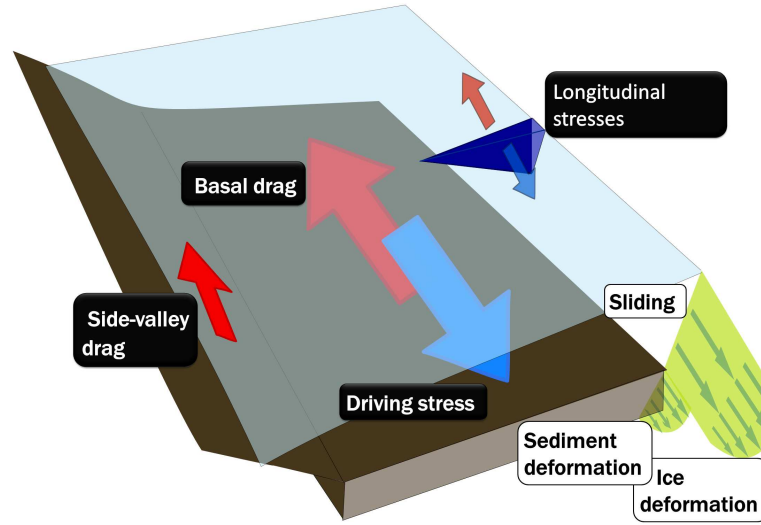


Figure 2.4: Scheme of stresses acting in large-scale ice sheet flow

2.3.1 Basal sliding

The first mechanism by which basal water contributes to ice movement is through lowering the resistance against basal sliding, i.e. the basal drag τ_b [Pa], by lubricating the ice-bed interface. For basal sliding, basal drag is the steering variable, and will link sliding speeds and basal water properties in a sliding law. Unfortunately, basal drag is difficult to measure and assumptions often need to be made. Large scale ice sheet models (ISMs) often rely on a Shallow Ice Approximation (SIA, for equations see section 2.4.1), which is based on the assumption of lamellar ice flow. In the SIA, longitudinal and side valley stress gradients are neglected and the gravitational driving stress τ_d equals the basal drag τ_b , meaning all resistance to ice flow is caused by the bed (and no longitudinal and/or side valley drag). As such, large scale ice flow is only driven by local thickness and ice surface slope. Basal drag or driving stress τ_d is then given by:

$$\tau_b = \tau_d = -\rho_i g H \nabla z_s \quad (2.7)$$

Although some ice streams are confined, causing significant side valley drag, most ice flows in Greenland or Antarctica are sufficiently vast to fulfill the SIA assumptions.

The basal drag τ_b is then linked to ice velocities through a sliding law. After the first simultaneous measurements of ice velocity and basal water pressure in the 1980s on Trapridge Glacier (Canada) and Storglaciären (Sweden), the first sliding laws that accounted for basal water were in the form of:

$$\mathbf{U}_s \propto N^{-p} , \quad (2.8)$$

with U_s the horizontal ice surface velocity [m/s] and p a parameter [-] (Van der Veen, 2013; Cuffey and Paterson, 2006). High effective pressures ($P_i > P_w$) and low surface velocities are linked to efficient drainage, low effective pressures ($P_i \approx P_w$) trigger high surface velocities. Such observation-based sliding laws only account for local phenomena whereas ISMs requires a global sliding law that is valid over a large spatial extent to determine basal sliding velocities. Moreover, surface velocities \mathbf{U}_s and basal sliding velocities \mathbf{U}_b differ significantly, as ice deformation takes place in the ice column. Therefore, current large-scale applications that couple basal water with ice flow compute basal sliding velocities directly, for example using the empirical equation:

$$\tau_b \stackrel{SIA}{=} \tau_d = B \mathbf{U}_b^q N^r, \quad (2.9)$$

with B a parameter [s/m], q and r dimensionless parameters, τ_b the basal shear stress [Pa] and \mathbf{U}_b the basal sliding speed [m/s] (Le Brocq et al., 2009).

The most advanced sliding law, the Coulomb friction law, developed by Schoof, sets a maximum for basal drag, based on friction with the steepest objects at the bed. This sliding law should not be used in SIA since driving stresses might become larger than this upper boundary (Pimentel et al., 2010; Creyts and Schoof, 2009). Experiments using the Coulomb friction law showed significantly different spatio-temporal behaviour between SIA and higher-order solutions, in both obtained ice geometries and effective water pressure N (Pimentel et al., 2010).

Lakes deserve special attention again here, as they do not only provide lubricating water for the ice, but also smoothen the basal thermal gradient by acting as a thermal source. As such, subglacial lakes might cause a wide front of enhanced sliding downstream (Kohler, 2007; Bell, 2008). On the other hand, when little water is entrained, lakes can also buttress ice flow downstream. Historic lakes can be conserved through establishing a stable ice-surface flattening feedback. As the ice flows over a subglacial lake, in essence floating, its upper surface flattens out, causing the ice surface gradients to weaken and the water to remain in the lake configuration, despite continuous ice flow.

2.3.2 Sediment deformation

When the bed is soft, such as the thawed bed found under the WAIS, water pressures might also affect the sediment deformation rate $\dot{\epsilon}_s$, the second basal component of ice flow. Most of this work is based on laboratory measurements. Water pressure N is used to lower the overall basal shear stress, or the yield strength of the sediment. Driving stresses exceeding these low yield stresses can lead to high basal ice velocities again. However, these driving stress must be countered again by side valley drag, longitudinal stresses or local sticky spots with high τ_b . Consequently, the SIA assumptions are no longer valid when considering $\dot{\epsilon}_s$. It is unknown whether a local thin water film interacts with sediment deformation system,

or whether sliding and deformation mechanisms interact with ice flow separately (Le Brocq et al., 2009; Clarke, 2005; Cuffey and Paterson, 2006).

2.4 Thermomechanical ice sheet models

As seen in Eq. 2.4.3, basal ice temperatures must be known in order to predict a basal melting rate \dot{M}_b . For this reason, only thermomechanical ice sheet models will be covered here, simulating ice thickness H evolution and ice temperature T profiles simultaneously. Thermomechanical ISMs offer valuable insights for predicting sea level changes and interpreting ice cores, providing estimations about the past, present and future evolution of large scale ice sheets.

2.4.1 Modelling ice flow

In their most complex form, ice flows can be described through the Navier-Stokes equations, assuming incompressible flow.

$$\rho \left(\frac{\partial \mathbf{v}}{\partial t} + \mathbf{v} \cdot \nabla \right) = -\nabla \mathbf{p} - \nabla \mathbf{T} + \mathbf{f} , \quad (2.10)$$

with \mathbf{v} the three-dimensional ice velocity vector, \mathbf{p} and \mathbf{T} the orthogonal and shear stresses respectively, and \mathbf{f} the external force field. For large scale modelling, accelerations may be neglected, making the left-hand-side of Eq. 2.10 disappear. However, most ISM formulate the force balance in terms of a stress tensor, including 9 components of shear and stress components, and the only external force considered being gravity.

$$\frac{\partial \tau_{x,x}}{\partial x} + \frac{\partial \tau_{x,y}}{\partial y} + \frac{\partial \tau_{x,z}}{\partial z} = 0 \quad (2.11)$$

$$\frac{\partial \tau_{y,x}}{\partial x} + \frac{\partial \tau_{y,y}}{\partial y} + \frac{\partial \tau_{y,z}}{\partial z} = 0 \quad (2.12)$$

$$\frac{\partial \tau_{z,x}}{\partial x} + \frac{\partial \tau_{z,y}}{\partial y} + \frac{\partial \tau_{z,z}}{\partial z} = \rho_i g , \quad (2.13)$$

with $\tau_{i,j}$ [Pa] normal stresses when $i = j$ and shear stresses when $i \neq j$. Models using the full Navier-stokes equations or calculating all stresses from Eq.2.13 are called higher-order ice sheet models. Examples include the Community Ice Sheet Model project (CISM) or the Elmer ISM. For the ISM, a new higher-order scheme was recently introduced, considering longitudinal stresses in the force balance, and applied on Greenland (Fürst, 2013). Comparative studies between higher-order ISMs were done using benchmark experiments for known flowline geometries like the Arolla glacier. These inter-comparisons showed close agreement between higher order model predictions (Pattyn et al., 2008).

Simplified ISM's using the SIA, often operating on larger scales, assume shear stress on side walls $\tau_{x,y}$ to be 0, and the longitudinal stress deviators $\tau_{z,y}$ and $\tau_{z,x}$ to be negligible compared to the other shear stresses ($\tau_{z,z}, \tau_{y,y}, \tau_{x,x}$). Simplified SIA models also show qualitative agreements again in comparative studies (Payne et al., 2000).

Most modelling difficulties arise in defining large-scale boundary conditions. Temperature equations for example, require air temperature at the ice-atmosphere interface and a basal temperature gradient, mostly determined through a geothermal heat flux G . For the geometry, grounding lines can be static or dynamic after setting an initial geometry (Vaughan and Arthern, 2007). Finally, for the conservation of mass, surface mass balance \dot{M}_s should be known. Basal sliding can also be seen as a boundary condition which is time-varying and impacts ice flow greatly, posing a major challenge in ISMs. The sliding laws put forward in section 2.3.1, involving water pressure for example, have only rarely been used in continental ice sheet modelling efforts (Pimentel et al., 2010).

2.4.2 Huybrechts ice sheet model

The ISM used in this thesis was developed by Huybrechts from 1986 onwards. After being developed on a conceptual geometry, and later expanded to cover the entire GrIS and the AIS. Up to this day, the Huybrechts ISM produces one of the most comprehensive appreciations of glacial-interglacial ice-sheet fluctuations for both the GrIS and AIS, illustrating for example the topography-based differences between the stable EAIS and the unstable WAIS (Huybrechts, 2002). Specifically, for the Huybrechts model, the stress tensor, continuity, flow law and thermodynamic equations are solved simultaneously using an Alternating Direction Implicit integration method (ADI), with a spatial resolution up to 5km grid sizes so far. The vertical coordinate is normalised relative to ice thickness, and a staggered grid is used in the horizontal direction to improve stability of the solution. The simplified stress tensor solved here, following the SIA, is given below:

$$\frac{\partial \tau_{x,x}}{\partial x} + \frac{\partial \tau_{x,z}}{\partial z} = 0 \quad (2.14)$$

$$\frac{\partial \tau_{y,y}}{\partial y} + \frac{\partial \tau_{y,z}}{\partial z} = 0 \quad (2.15)$$

$$\frac{\partial \tau_{z,z}}{\partial z} = \rho_i g \quad (2.16)$$

2.4.3 Modelling ice flow

Generally, one is interested in ice flow variables, whilst variables in the solved equations are based on stresses. Ice flow or ice velocities are calculated as a deformation or strain rate $\dot{\epsilon}$ [1/s]. Since ice is a non-Newtonian fluid, the relationship between stresses τ and strain rates $\dot{\epsilon}$ is non-linear and is given by Glen's flow law (Van der Veen, 2013; Cuffey and Paterson,

2006):

$$\epsilon_{i,j} = mA(T)\tau_*^{(n-1)}\tau'_{i,j}, \quad (2.17)$$

with $\epsilon_{i,j}$ [1/s] the components of the strain rate, m (specific for this ISM) a tuning factor, $A(T)$ [Pa⁻ⁿ/s] the temperature-dependent flow law coefficient and n the flow law exponent, usually $n = 3$. T is the ice temperature, τ_* the effective stress (all components assembled) and $\tau'_{i,j}$ the deviatoric stress is given by

$$\tau'_{i,j} = \tau_{i,j} - \frac{\delta_{i,j}\tau_{kk}}{3} \text{ for } i, j, k = x, y, z \quad (2.18)$$

with $\delta_{i,j}$ the Kronecker delta (being 0 if $i \neq j$, and 1 otherwise). A 's temperature dependency is given by Arrhenius relation, where warm ice deforms more than cold ice (Huybrechts, 1986; Payne et al., 2000).

Finally, these strain rates $\epsilon_{i,j}$ are related to the three-dimensional velocity vector ($\mathbf{v} = (u, v, w)$) gradients $\frac{\partial u}{\partial x}$, $\frac{\partial v}{\partial y}$ and $\frac{\partial w}{\partial z}$. Using the obtained ice flow velocity field, the conservation of mass requires a continuity equation for ice:

$$\frac{\partial H}{\partial t} = -\nabla \cdot (\bar{\mathbf{U}}H) + \dot{M}_s - \dot{M}_b, \quad (2.19)$$

with $\bar{\mathbf{U}}H$ the flow divergence, $\bar{\mathbf{U}}$ the vertically averaged 2-dimensional velocity vector \mathbf{U} , \dot{M}_s surface mass balance [m/year] and \dot{M}_b is basal melting rate. The two last variables are calculated using meteorologic data and simulated ice temperature profiles, obtained hereafter. Although basal melt rates are given through Eq. , for practical use in the ISM, they are calculated as the heat required to bridge the temperature difference between the basal ice layer and the pressure melting point.

2.4.4 Modelling ice temperature profiles

The following thermodynamical equation describes the temperature evolution within the ice:

$$\frac{\partial T}{\partial t} = \frac{1}{\rho_i c_i} \frac{\partial T}{\partial z} \left(k_i \frac{\partial T}{\partial z} \right) - \mathbf{V} \cdot \nabla T + \frac{2\epsilon_* \tau_*}{\rho_i c_i} \quad (2.20)$$

with k_i ice heat conductivity [W/mK], c_i ice heat capacity [J/kgK] and \mathbf{V} the three-dimensional ice velocity vector (Cuffey and Paterson, 2006; Van der Veen, 2013).

As such, model coupling of temperature with ice flow in a thermodynamical ice sheet model is done through a temperature dependent flow parameter A in the flow law (Eq. 2.17), and a flow dependent heat advection and production in the thermodynamical equation (Eq. 2.20). Basal sliding is implemented as a boundary condition:

$$\mathbf{U}_b = -\frac{A_{sl}\tau_d}{Z}, \quad (2.21)$$

with $A_{sl} = 1.810^{-10} N^{-3} year^{-1} m^8$ and Z a reduced basal traction, given by

$$Z = H \text{ if } z_b > 0 \tag{2.22}$$

$$Z = H + \frac{\rho_w z_b}{\rho_i} \text{ if } z_b < 0, \tag{2.23}$$

causing faster sliding for outlet glaciers in deep throughs for example. Note that this sliding is independent on any water flow variables. Finally, other components include a surface mass balance \dot{M}_s model based on positive degree days (PDD) and an isostatic adjustment model based on a elastic lithosphere (Huybrechts, P., Payne, 1996; Huybrechts and De Wolde, 1999). A general overview of the Huybrechts ISM is given in Fig. 2.5.

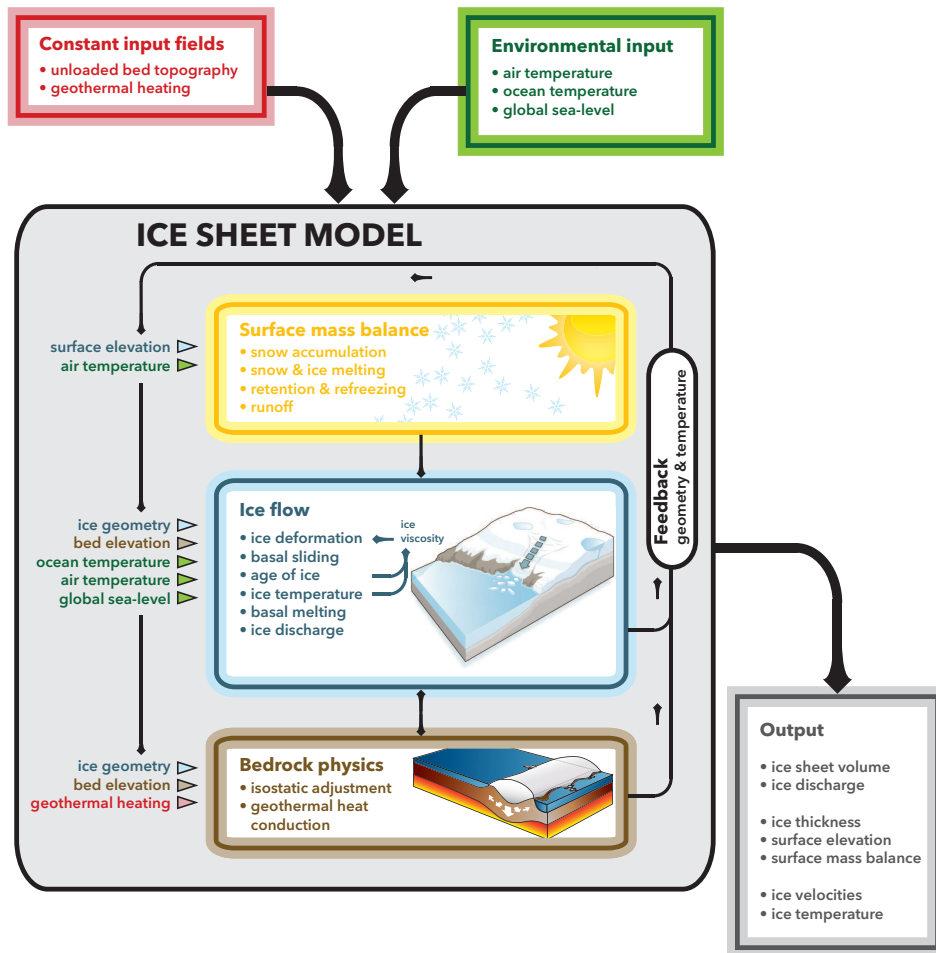


Figure 2.5: Overview and components of the Huybrechts ISM: Initial and boundary conditions are given outside the rectangle. Considered processes are surface mass balance (SMB), ice flow and bedrock physics, with the included variables given with triangles. Output is given on the right (Fürst, 2013).

2.5 Basal water model

In the relatively new branch of modelling subglacial hydrology, the Weertman film assumptions seem to hold for large-scale modelling applications and have been applied over Antarctica by several authors (Johnson, 2002; Le Brocq et al., 2009). Since then, more inclusive bottom-up approaches have also been used, where the assumption of $P_i = P_w$ may be discarded. These are still to be applied on continental scales, but are promising since they comprise more realistic, local assumptions. Flowers (2002) and Pimentel et al. (2010) use a multi-layered approach, considering water in the ice, on the bedrock and in the sediment, as well as interaction between these three layers. Schoof (2010) set up a model mimicking the transition between channelized and film flow and was able to capture seasonal effects in this way.

2.5.1 Setup

In the basal water model (BWM) applied here, water is formed through basal melting and routed in a thin Weertman film, assuming $N = 0$, or $P_i = P_w$. In a first step, hydraulic potential ϕ is calculated (Eq.2.3). To ensure drainage all the way to the coast, local potential depressions are filled, meaning a grid cell that has no neighbours with a lower hydraulic potential is changed to the average potential of the 4 or 8 surrounding grid cells. When identical values between these updated potentials arise, a small random factor is added. This method has been shown to perform well for previous AIS datasets (Bedmap1, Albmap) up to a 5 km resolution. A balance flux algorithm is used to route an increasing amount of basal water, from a high to a low potential. Balance fluxes means fluxes are calculated Φ per unit width of a cell, thus Φ is given in m^2/year . Eventually, every cell (i, j) for which basal melt rate $\dot{M}_b > 0$ mm/year produces an outgoing flux Φ^{out} of water:

$$\text{outflow} = \text{inflow} + \text{basal water production} \quad (2.24)$$

$$\Phi^{out} = \Phi^{in} + \dot{M}_b \Delta r^2, \quad (2.25)$$

with Δr the dimension of a grid cell in km. In the case of 4 neighbours (Warner algorithm, using North, East, South and West), incoming water Φ^{in} is derived from the outgoing fluxes Φ^{out} of 4 surrounding cells with potential $\phi_{\text{neighbour}}$. Similarly, 8 neighbours are used in the Quinn routing algorithm (Le Brocq et al., 2006). The difference in our application will be illustrated (Fig. 3.6).

$$\Phi^{in} = \frac{(\phi - \phi_{\text{neighbour}})}{\sum_{N,S,E,W} \Delta\phi} \Phi_{\text{neighbour}}^{out} \quad (2.26)$$

In this way, each of the surrounding cells can flow into the central cell, with contributions relative to the potential difference $\Delta\phi$. The outgoing flux Φ^{out} can be converted to a balance flux field Φ :

$$\Phi = \frac{\Phi^{out}}{\Delta r (|\sin \theta| + |\cos \theta|)} \quad (2.27)$$

with θ the angle of flow direction relative to the x direction (Le Brocq et al., 2006). Additionally, grid sizes are also corrected for map projection errors in the data.

In order to calculate water velocities, a continuous Weertman film flow is assumed, similar to laminar flow between two parallel plates. The water layer thickness d in this approach is given by

$$d = \sqrt[3]{\frac{12\mu\Phi_{\text{out}}}{|\nabla\phi|}} \quad (2.28)$$

with μ the viscosity of water. The depth-averaged water velocity $\overline{\mathbf{u}_w}$ is given by

$$\overline{\mathbf{u}_w} = -\frac{d^2}{12\mu}\nabla\phi, \quad (2.29)$$

where the minus sign indicates flow from high to low hydraulic potential. On a large scale, a Weertman film is commonly assumed since $P_i \approx P_w$, and the resolution of the ISM is too coarse to resolve more local features. The water model is, unlike the ice sheet model, not time dependent and a steady state with the input geometry is assumed. Considering the different time scales between ice dynamics (centuries to millennia) and basal water flow (hours to weeks), this is a reasonable assumption for a given geometry of the ice sheet. In the following, the BWM will be run with BEDMAP2 data, and some effects will be discussed. Next, the model is adapted to work for Greenland.

CHAPTER 3

Antarctica: basal water model applications

3.1 Dataset and processing

3.1.1 Geometric data: Bedmap 2

The BEDMAP project, coordinated by the British Antarctic Survey, produced BEDMAP1 in 2001, followed by BEDMAP2 in 2013. Compared to the last data compilation in 2010 by LeBrocq (ALBMAP), a larger ice volume and a lower bed is presented over the continent. These balance each other out, causing only a small difference in overall potential SLR contribution, from 57 m previously (ALBMAP), to an estimated 58 m in the BM2 dataset (Fretwell et al., 2013). In mountaineous regions like the Gamburtsev and Transantarctic mountains, a higher level of detail is presented in BEDMAP2 relative to previous compilations. Large deepening can be seen around Recovery Glacier and Lambert Glacier, deep throughs eroded by ice streams (Fig. 3.1a). The new BEDMAP2 dataset (further referred to as BM2) was derived from $25 \cdot 10^6$ datapoints, mainly obtained through ICE-SAT satellite altimetry, MODIS images, airborne and over-snow radar surveys, gravimetry and some synthetic thickness data. Although the dataset is provided at a spatial resolution of 1 km, data points were originally gridded on a 5 km resolution, and in reality only 83 % of the Antarctic surface is within 20 km of a measured thickness point, thus requiring substantial interpolation (Fig. 3.1b).

Next to surface elevation z_s [m], bed elevation z_b [m] and ice thickness H [m], BM2 data are accompanied with a mask delineating Lake Vostok contours (from which the depth of the lake d_{vostok} was derived), and masks, delineating ice shelves and bare rock. The amount of data also allows for both data and gridding uncertainties to be mapped, both depending on used techniques, roughness and degree of coverage. Ice thickness uncertainties in well-sampled, rough regions like the Gamburtsev mountains range between 100 – 150 m. Smooth sections like Siple Coast have accurate ice thickness up to 50 m or less, whilst the scarcely sampled

areas using gravimetry derived ice thickness exhibit uncertainties up to 1000 m, for example between Recovery and Support Force Glacier (Fig. 3.1b).

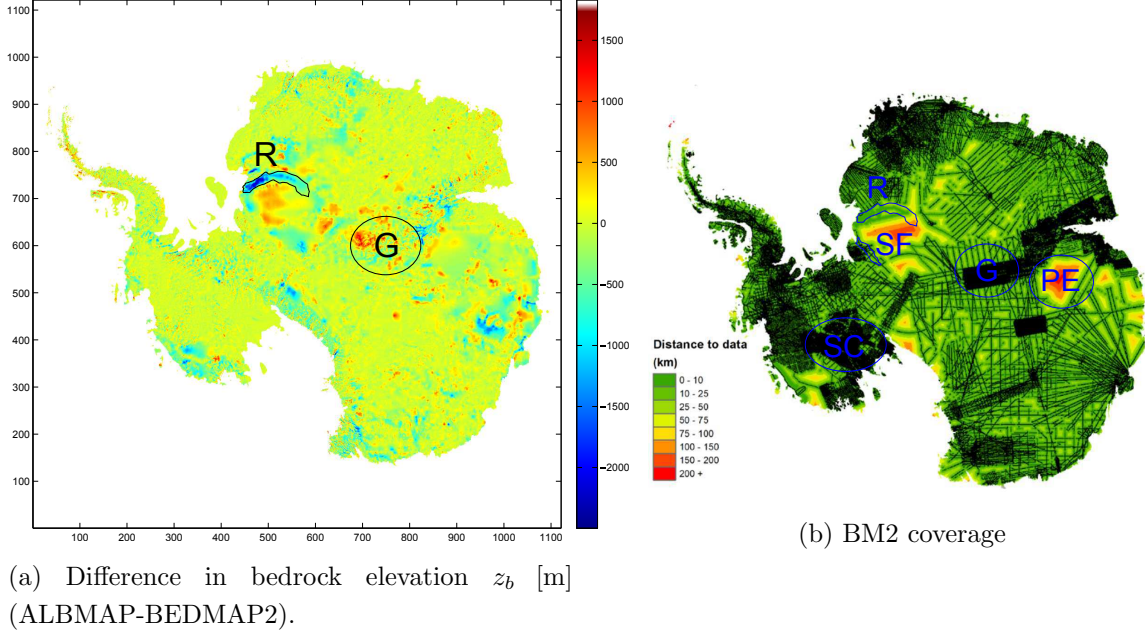


Figure 3.1: BM2: improvements relative to ALBMAP (2010, 5 km resolution and data coverage).

PE=Princess Elisabeth land, SF=Support Force glacier, SC=Siple Coast, G=Gamburtsev mountain range, R=Recovery glacier.

Adaptations for ISM and BWM applications

In order to use the BM2 data in the Huybrechts ISM, some corrections had to be made. For the BWM simulations, ice shelves need not to be considered. However, some ISM applications take into account ice shelf dynamics, thus they had to be represented in the best possible way for future applications. Using the fixed ice and ocean densities assumed in the ISM ($\rho_i = 910 \text{ kg/m}^3$, $\rho_o = 1028 \text{ kg/m}^3$), ice thickness H and correct floatation should be ensured. For this, the under-water part of the floating ice shelf was chosen as a reference value, since both surface elevation z_s and ice thickness H are well measured, and the density of the underwater ice is likely to be fairly constant.

If we would assume the surface elevation of the ice shelf to be correct, the ice shelf would have to gain ice thickness to ensure floating under assumed densities, since in reality, the density of the upper layers of ice shelf is lower than the ρ_i because of firn layers (accumulated snow in an intermediary state of compaction). Considering hydrostatic equilibrium, a thicker shelf would place the ice deeper in the ocean (since z_s is constant) and require a lower bed elevation z_b in order to ensure correct floating or grounding. This bed deepening could create

unrealistically deep canyons, especially near thick floating sections. The same problem arises when ice thickness H would be chosen as a reference value: the less dense upper ice and snow layers would cause a general sinking of the shelf, and again require a lowering of z_b to stay afloat.

Instead, the underwater part of the ice shelves was assumed to be correct using ice density ρ_i and ρ_o . Ice thickness H and surface elevation z_s over the ice shelf were then adapted according to Archimedes' law:

$$\hat{H} = (H - z_s) \frac{\rho_o}{\rho_i} \quad (3.1)$$

$$\hat{z}_s = \hat{H} \left(1 - \frac{\rho_i}{\rho_o}\right), \quad (3.2)$$

with \hat{H} and \hat{z}_s the adapted ice thickness and surface elevation of the ice shelves [m] respectively. For grounded ice, potential gaps between bedrock and the lower ice surface are closed, for example Lake Vostok, delineated explicitly in a separate data field

$$\hat{H} = z_s - z_b - d_{vostok}, \quad (3.3)$$

with \hat{H} the new ice thickness over grounded ice and d_{vostok} the depth of Lake Vostok [m]. The change in H and z_s can be seen as a realistic firm correction, compaction of the less dense upper layer of firm on the ice shelves to ensure a fixed density $\rho_{i,ISM}$ over the total ice column. The values for these corrections, about 30 m on average (Fig. 3.2d), match the modelled firm corrections obtained by Ligtenberg et al. (2011). Yet, some shelf points required more substantial corrections, to ensure consistent thickness and floating. Such anomalies can be due to errors in BM2 grounding line data, thickness, or bed data, or small deviating ice densities like non free-floating ice in narrow embayments.

Next, the consistent thickness \hat{H} is checked to match an ice mask obtained in the data, delineating grounding and floating parts. Deviations from a predefined floating criterium flc indicate incorrect grounding or floating:

$$flc = \left(z_b + \frac{\hat{H} \rho_i}{\rho_o}\right), \quad (3.4)$$

where for grounded ice, this floating criterium flc should be > 0 . For floating parts, flc should be ≤ 0 . If not, z_b is respectively heightened or lowered to match this:

$$\hat{z}_b = z_b - flc. \quad (3.5)$$

The 1 km results have to be downscaled to the different resolutions used in the ISM and BWM: 2, 5, 10 and 20 km. Four interpolation methods were implemented: direct subsampling, weighing over surrounding cells, and two hybrid approaches. In the first hybrid approach, weighing is only applied near rock outcrops to ensure smoothing; in the second, subsampling is done near the grounding line and weighing is applied elsewhere. Although the

first hybrid approach (weighing around outcrops) provided a dataset with a stable solution in the ISM, subsampling outside regions with rock outcrops leads to a loss of information between gridpoints. Therefore, the last method (direct subsampling around grounding line, weighing otherwise) was accepted as the most appropriate. The weighing preserves information in the data of all surrounding cells during the interpolation, whilst subsampling ensures a fixed grounding line between different resolutions. Weighing near the grounding line would produce an advancing grounding line over lower resolutions.

Next to the interpolation method, two fields to be interpolated had to be chosen, along with a third one left to calculate. Since a discontinuity of H near the grounding line or ice sheet margin may arise, Z_b and z_s are interpolated, and H is calculated accordingly (Bamber et al., 2013a). Consistency has to be ensured over all resolutions. Therefore, a mask is delineated from direct subsampling on the lower resolutions, and based on these, thickness and floating consistency checks are performed again. Finally, the results were adapted according to the purpose. For the ISM, a continuous ice cover was guaranteed, Lake Vostok was filled and islands were removed, whereas for the BWM only the islands are removed, since they are not considered relevant in this discussion. To perform these last adaptations, the same methodology as with previous datasets was applied (personal communication, I. Janssen).

Performance of adapted BM2 data

The adaptations are compared to the original 20 km BM2 data, focused around Amery ice shelf, a region exhibiting all possible variations of adaptation issues (Fig. 3.2). Zones over the shelf exhibit a change in z_s and H between 10 to 50 m, whereas some points near the grounding line display more significant corrections. In the grounded zone, a region can be seen where the bed was heightened to ensure grounding (red circle in Fig. 3.2). All corrections lie within the uncertainty ranges in the BM2 data, such that they may be seen as realistic firm corrections for the densities used here, or corrections of inconsistencies in the data. Differences in H and z_s are identical for the ice shelf since they represent Archimedes' law, whilst z_b and z_s adaptations are identical for grounded ice, because of constant ice thickness.

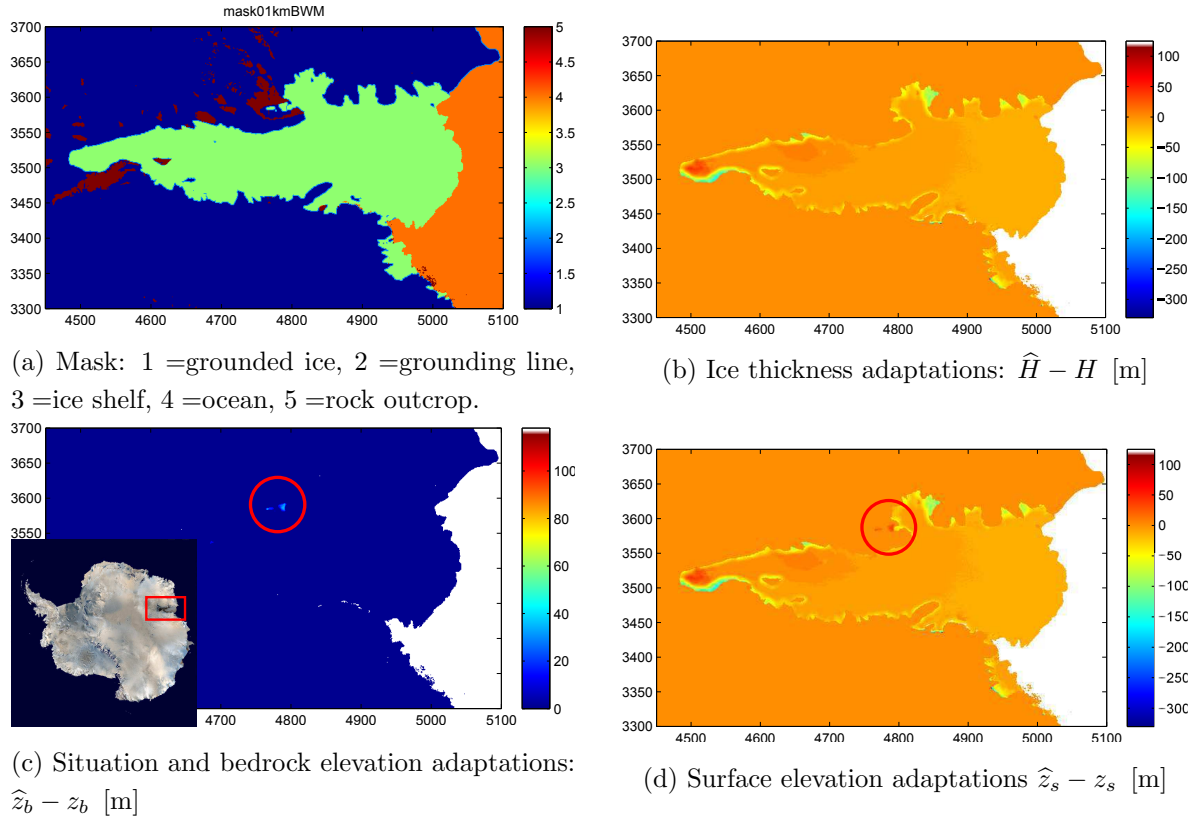


Figure 3.2: BEDMAP2: required adaptations for consistent ice thickness and floating at the Amery ice shelf.

To test the performance of the adapted dataset, an ISM experiment on a 20 and 10 km resolution was set up using a fixed grounding line, covering 50000 years, where the first 10000 years are used to relax the model to the input. Due to computational constraints, a higher resolution run of 5 km, obtained through downscaling the output from 10 km followed by a 2000-year experiment was not used further in this thesis. The difference between the output of withheld ISM experiments and the original BM2 data is shown in Fig. 4.2. As observed in previous ISM simulations, ice over Siple Coast remains too thick, possibly due to the combined effect of basal sliding and soft sediment deformation causing faster ice flow in practise. Another possible reason for this is a serious underestimation of the geothermal heat flux G in the input data, since localized volcanic activity might produce higher amounts of water at the bed (Lough et al., 2013). The ISM also might be incapable of draining ice through the Transantarctic Mountains at sufficient rates, which could be due to multiple reasons again, like underestimation of basal ice temperatures.

As the resolution increases, finer flowbands allow more ice to be carried out of the overestimated regions, causing errors to decrease. The lowest underestimation is also no longer below -1000 m. The overall spatial error pattern remains similar between resolutions. These are

relatively simple ISM runs (runtime up to 9 days), so results could improve by using other experimental setups, which is outside the scope of this thesis.

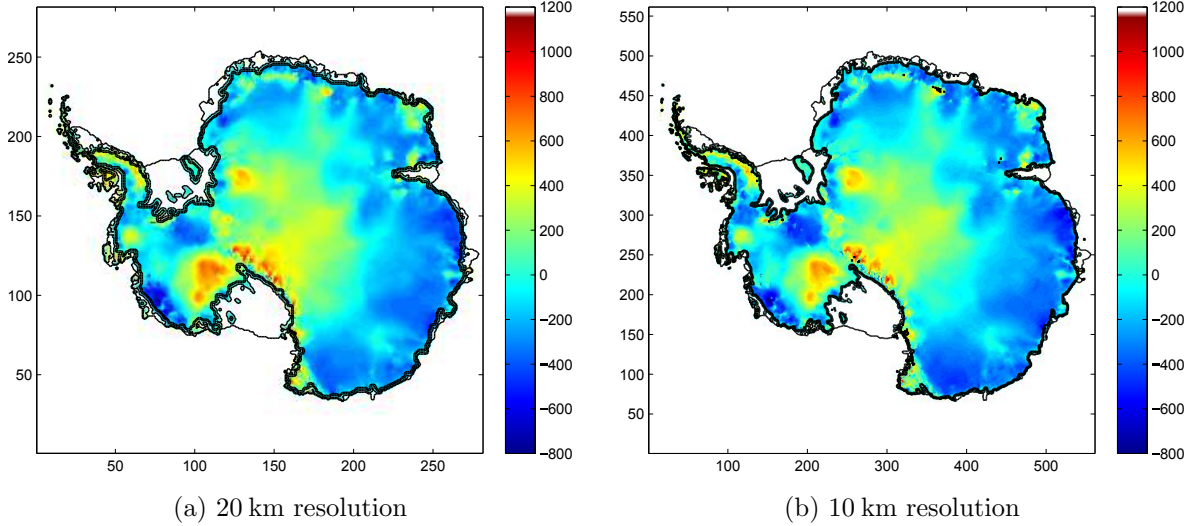


Figure 3.3: Difference between the ISM output [m] for a fixed geometry experiment, using adapted BM2 data, and the original BM2 data. Higher values indicate ISM overestimations.

3.1.2 Modelled data: basal melting rate

For estimates of the basal water system in past configurations of the ice sheet, geometric data obtained from the ISM can be used as geometric input for the BWM. As shown above, ISMs still produce significant errors in simulating ice geometry. Since we are focusing on the present state for the AIS, and the hydraulic potential is strongly steered by surface elevation gradients (Eq. 2.3), we will use the more detailed and realistic BM2 data for the BWM, instead of ISM output. However, for the basal melting rate \dot{M}_b , the only estimations available are given by ISMs through Eq. 2.4.3. The temperature T and basal velocity \mathbf{U}_b fields in this equation are obtained from simulations. It is important to keep in mind that these are based on a different geometry as the one used in the actual BWM, meaning the basal melt rates are only consistent with ISM geometries, and not with observed geometries. For the geothermal heat flux (GHF), several datasets are available, we opted for the Shapiro-Ritzwolle dataset, which is mainly used in applications of the Huybrechts' ISM (Fig. 3.4). In experiments testing the BWM and sensitivity experiments, a uniform \dot{M}_b of 1 mm/year is used, to exclude local influences of melting and routing.

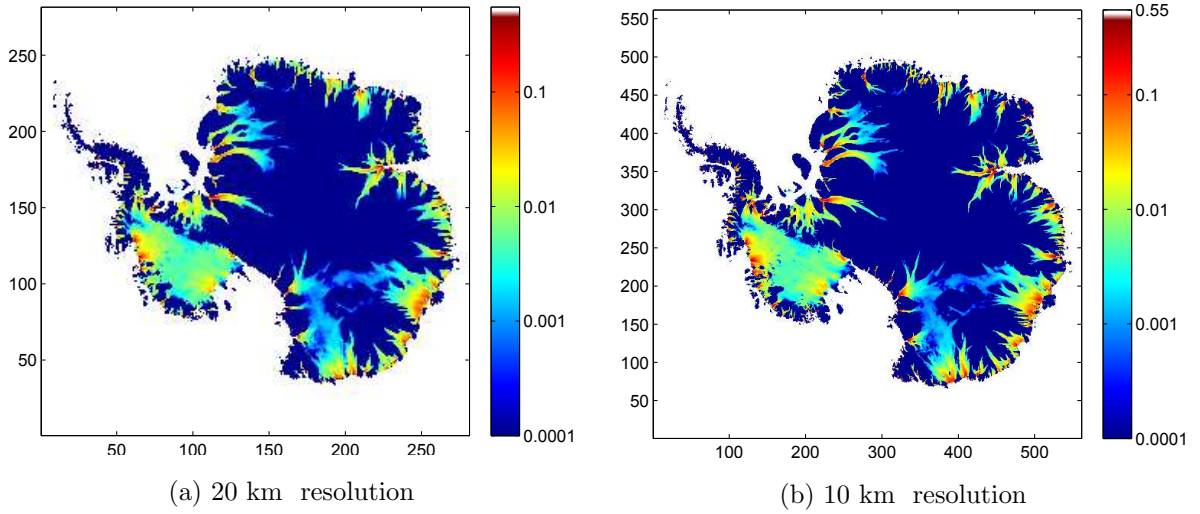


Figure 3.4: \dot{M}_b [m/ year] for Antarctica obtained with simulations using Shapiro-Ritzwoller GHF, on a 20 and 10 km resolution.

3.2 BWM experiments and results

The BWM was adapted to work on higher resolutions, since it had only been used up to 5 km previously. Some smaller adaptations were performed first:

- Changing water density, which was previously set to ocean water ρ_o , whilst Eq. 2.3 and the BWM requires fresh water density ρ_w , as land ice is being melted and not sea ice.
- Number of columns and rows, iterations, resolution variables, etc.
- Code improvements in terms of efficiency: the smoothing algorithm was implemented using less lines. This part of the code would later improve further when other methods were implemented, trying to reach convergence in depression-filling (Table 3.1).
- The random factor added to flat spots during the filling procedure was set to average 0 (by subtracting 0.5), ensuring no creation of artefacts with increasing number of iterations.

Depending on the experiment, further adaptations were made 3.2.

In order to get an overview of the BWM, typical outputs at the lowest resolution of 20 km are given in Fig. 3.5, using a uniform \dot{M}_b of 1 mm/year. Since we are considering a steady state solution, fluxes are given as an average over the entire year.

The flux or water discharge is given by Eq. 2.27. When considering a Weertman film, this water flux flows in a laminar film with thickness d (Eq.2.28) and depth-averaged velocity $\overline{\mathbf{u}_w}$ (Eq. 2.29), Water velocity is closely related to the flux (both depend strongly on hydraulic

potential gradient $\nabla\phi$), film depth is less comparable since it only depends on the potential gradient through $\sqrt[3]{\nabla\phi}$.

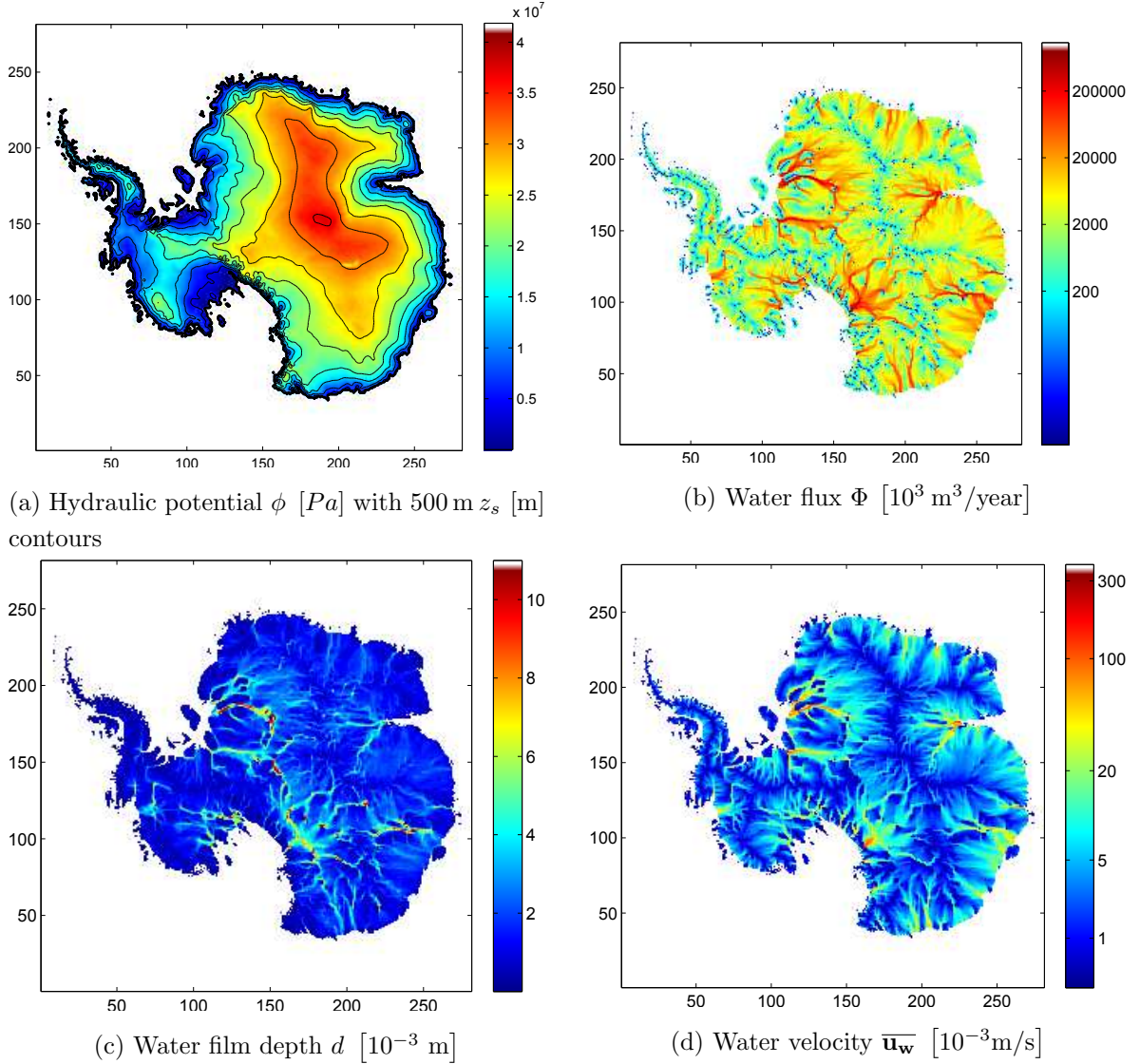


Figure 3.5: BWM output fields on 20 km resolution using adapted BM2 data and a uniform basal melting rate \dot{M}_b of 1.10^{-3} m/year.

3.2.1 Hydraulic depressions: improvements and potential lakes?

The hydraulic potential ϕ closely resembles surface elevation z_s contours in regions with flat bedrock like Siple Coast. However, in regions with high topographic variability like the Transantarctic mountains, ϕ is strongly dependent on bedrock elevation z_b . Depressions in the hydraulic potential might represent lakes underneath the AIS. As regions with high to-

pographic variability become more detailed, more depressions in the hydraulic potential are found with increasing resolution, as widely recognised in literature (Johnson, 2002). Due to the level of detail of the BM2 data, it encloses deeper depressions as compared to previous datasets, that take longer to fill using the existing smoothing algorithm (section 2.5.1), including for example Recovery glacier and the Adventure Subglacial Trench (Fig. 3.1a).

Improvements: 20 km resolution

A long quest was performed looking for a more optimal method of filling depressions, on the lowest resolution of 20 km (Table 3.1). Also given in this table are the mass imbalances, expressing the relative difference between the amount of water present at the bed, and the water reaching the ocean. Large imbalances ($> 1\%$) can arise when filling is not guaranteed (Fig. 3.8) or regions inaccessible to basal water block the flow (Fig. 3.11).

1. 4 to 8 neighbours

Initially, the number of cells for the kernel scanning for lowest neighbours and incoming fluxes was increased from 4 to 8 cells. This means neighbours are also checked in the diagonal directions, which led to faster convergence of the filling (because of lower overtopping levels), and improved flux routing. The 4-cell or Warner approach is known to produce grid orientation effects, and since grid cells are oriented N-S whilst flow is primarily radially directed for the AIS, it is better to avoid these (Le Brocq et al., 2006). The 8 cell approach also produces dispersion when flowing parallel to the grid orientation (black circle in Fig 3.6b). Using 8 cells, flow can now also be routed diagonally instead of step-wise in the 4 cardinal directions, causing local flow diversions with increasing resolution. Finally, flow pathways become slightly more concentrated, as illustrated in the colorbar for the water flux under Byrd Glacier (Fig. 3.6).

2. Pre-filling Lake Vostok

As Lake Vostok is explicitly outlined in the BM2 data, it can be filled before entering the BWM. In all cases considered, this did not improve the convergence, since most time is spent filling the hydraulic potential along the edges of Lake Vostok.

3. Planchon's algorithm

Finally, a different filling algorithm was applied beforehand, one with a very high computational efficiency. Filling depressions in DEMs has been a widely discussed problem in hydrology, but simple large-scale implementations are less common (Wang and Liu, 2006). The approach chosen is an algorithm developed by Planchon (2002), and involves ordering all potentials in a list. Potentials are heightened sequentially after sorting them, starting from the most downstream point, similar to the flooding of an area. Highest points are stored temporarily in priority lists. A 1D example is given in Fig. 3.7. An efficient C++ implementation is called in Matlab and produces a filled depression field,

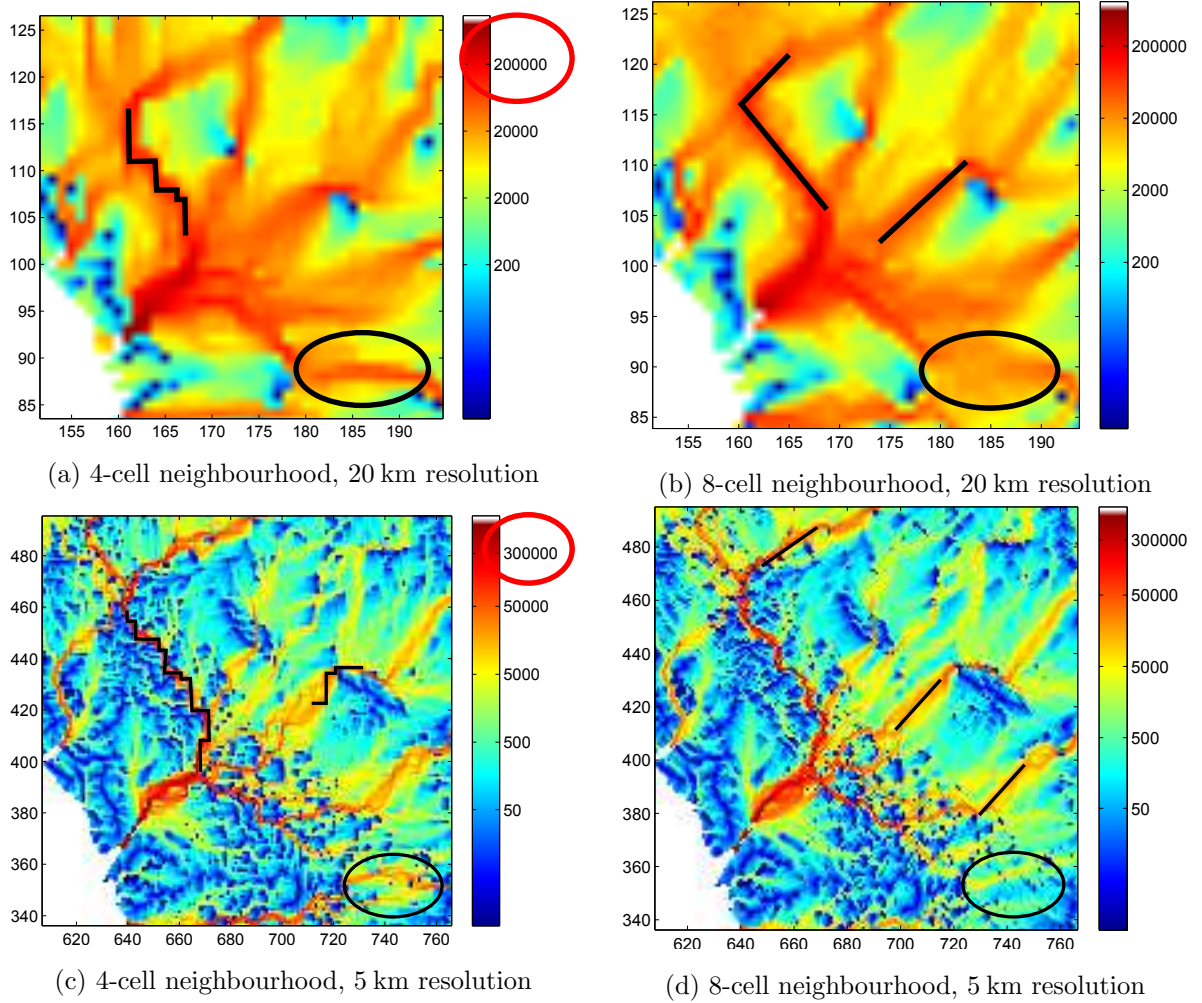


Figure 3.6: Illustration of neighbourhood size effect, water flux Φ [$10^3 \text{ m}^3/\text{year}$] on 20 and 5 km resolution, using a uniform basal melting rate \dot{M}_b of $1 \cdot 10^{-3} \text{ m/year}$. Red circles indicates a difference in maximal discharges, black lines indicate routing effects

which is then transferred to the BWM as input data. The Planchon (2002) algorithm can only be used with 8-cell neighbourhoods, since it is also based on scanning 8 neighbours. Pre-filling depressions using this algorithm ensured faster convergence of the smoothing in the BWM, especially useful on higher resolutions (Table 3.2). Computation time for the filling procedure using this algorithm is negligible compared to the previously used averaging algorithm, and the results can be used directly as estimations of potential lakes. Therefore, this method was withheld and used further in BWM applications on both Antarctica and Greenland. However, as the Planchon (2002) algorithm only produces perfectly flat filled depressions, smoothing in the BWM still involves adding a small slope to those flat regions, which might still lead to convergence problems on high resolutions (Table 3.2).

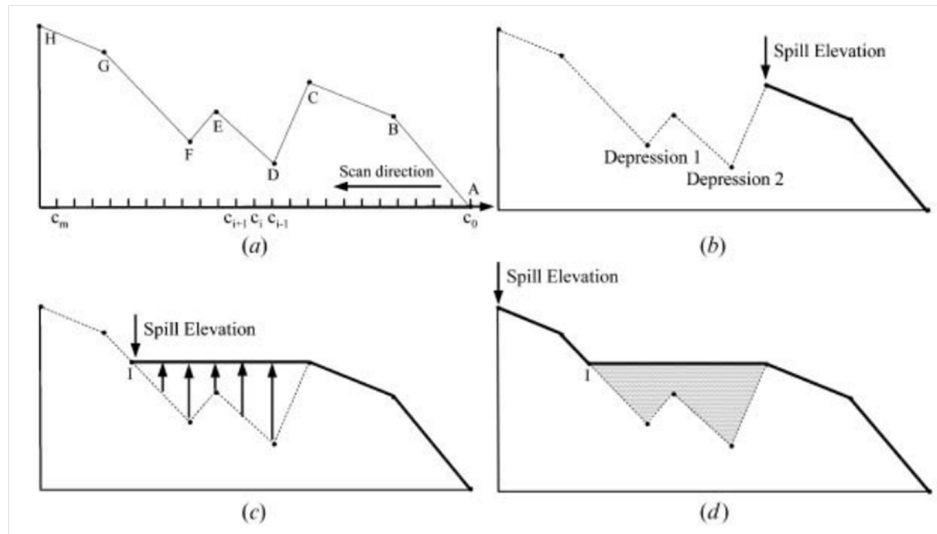


Figure 3.7: Planchon's algorithm for filling depressions, a 1D example. The potentials are prioritized and evened out from smaller to larger values (Wang and Liu, 2006).

Table 3.1: Improvements for filling depressions in the hydraulic potential, 20 km resolution, Antarctica.

Approach	iterations	mass imbalance
4 cells	89	0.194%
4 cells + Vostok	89	0.194%
4 cells + Planchon	72	0.194%
8 cells	57	0.089%
8 cells + Vostok	57	0.089%
8 cells + Planchon	22	0.089%

Improvements: higher resolutions

Upscaling this last selected approach to higher resolutions did not automatically lead to convergence with increased iterations. Using the standard approach outlined above, no convergence was obtained above 10km, with resulting mass imbalances up to a few % (Table 3.2). Therefore, from the 5 km resolution onwards, different additional changes (next to increased iterations) for the smoothing algorithm were tried:

- Different balance between random corrections and averaging: no improvement
- Higher random factor: lower mass imbalance, no convergence
- Double precision: first only random number, next all variables: no improvements

- Initial random factor added to bed: lower mass imbalance, no convergence above 5 km, but faster convergence for 10 km.

In summary, smaller mass imbalances are most easily obtained using an 8-cell method, pre-filled depressions, more iterations and adding a small random factor to the bed, which decreases difficulties in unflattening filled depressions. The locations where filling still did not converge were all located on the south edge of Lake Vostok and on the south-east edges of South Pole lake, the two largest depressions present. For Lake Vostok, the resulting erroneous fluxes cause inflow into these depressions, without allowing for outflow, leading to mass imbalance (Fig. 3.8). Since both problem regions are located in a cold-bedded zone, these errors will not occur in realistic basal melt scenarios (see 0.00363 % in Table 3.11).

Table 3.2: Depression-filling results and further improvements for all resolutions, Antarctica

Resolution [km]	iterations	mass imbalance
20	22	0.089 %
10	138	0.0021 %
5	> 200	3.28 %
5	> 6000	1.670 %
5	random factor*10,> 600	1.920 %
5	initial random factor added to bed, > 200	0.688 %
5	initial random factor added to bed, > 6000	0.521 %
2	> 6000	-1.406 %
1	> 6000	5.299 %

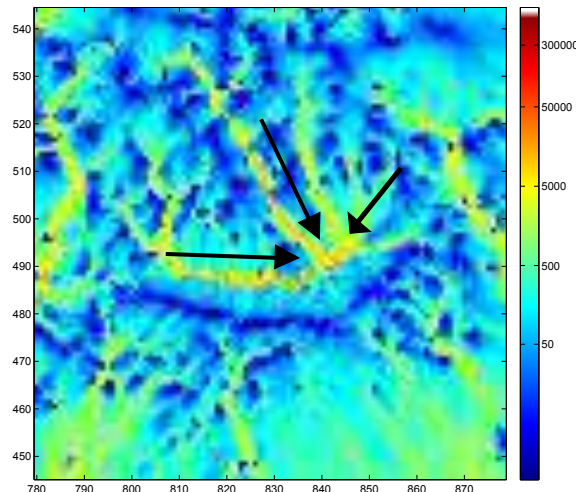


Figure 3.8: Mass imbalance around Lake Vostok, 5 km resolution. Unfilled depressions have no outflow, acting as a 'black 'hole' for water flow.

Potential lakes

Although removing these flat spots did not converge, using the Planchon algorithm, it is possible to get estimations of hydraulic depressions on the highest resolutions. Flat filled depressions now represent potential subglacial lakes, with the depth of the lakes d_l is given by:

$$d_l = \rho_w g \Delta \phi \quad (3.6)$$

As discussed above, the number of lakes increases with resolution (Fig. 3.9). These lakes are found in regions with highly variable bed or surface topography, as shown by the background z_b field or z_s contours (Fig. 3.9b, 3.9c). Depressions caused by surface elevations are abundant in the Transantarctic Mountains, whereas the flat ice surface near ice divides allows depressions to be created and outlined by bedrock features. Lake Vostok is seen, the southern edge might be outlined through the z_s gradient. The largest lake delineated is situated around the South Pole, on a presumed frozen bed. However, it is on the onset of a melting zone flowing out through the Support Force Glacier and Foundation ice stream. The positions of the lakes are compared to \dot{M}_b contours (in magenta) obtained from the ISM to indicate zones where water might be present at the bed ($T > T_{pmp}$), and thus the depressions might actually be water-filled (Fig. 3.9a, 3.9b, 3.9c). However, even without basal melt input, lakes under cold-based ice might persist (Palmer et al., 2013). Water might flow through cold-based ice (Fig. 3.11) and keep these depressions filled with water, or they might be relict lakes dating back to an advanced ice sheet in the Last Glacial Maximum (LGM) (Livingstone et al., 2013). It is again worth pointing out that these melt regions are based on a rough estimation of \dot{M}_b . Lake Vostok again for example, falls outside the melt zone, whilst in practise the water in the lake is recirculated through the melting and refreezing of overflowing ice, with an estimated average residence time for water in the lake of 13300 years (Bell et al., 2002).

3.2.2 Fluxes: resolution effect

After filling potentials as good and efficient as possible, it is interesting to look at the water fluxes Φ at different resolutions. For an increasing resolution, a refining in routing pathways and an increase in discharge in these pathways is seen, up to 5 km. For resolutions higher than 5 km, little significant improvements are seen. Several reasons can be found to explain this:

- Data resolution: BM2 was gridded on 5 km, so the additional amount of information about z_b or H starts decreasing rapidly for higher resolutions. This is especially the case for poorly covered regions (Fig. 3.1b and red circle in Fig. 3.10d).
- Depressions: complete filling of the depressions in the hydraulic potential is no longer guaranteed for resolutions of 5 km and higher (Table 3.2).

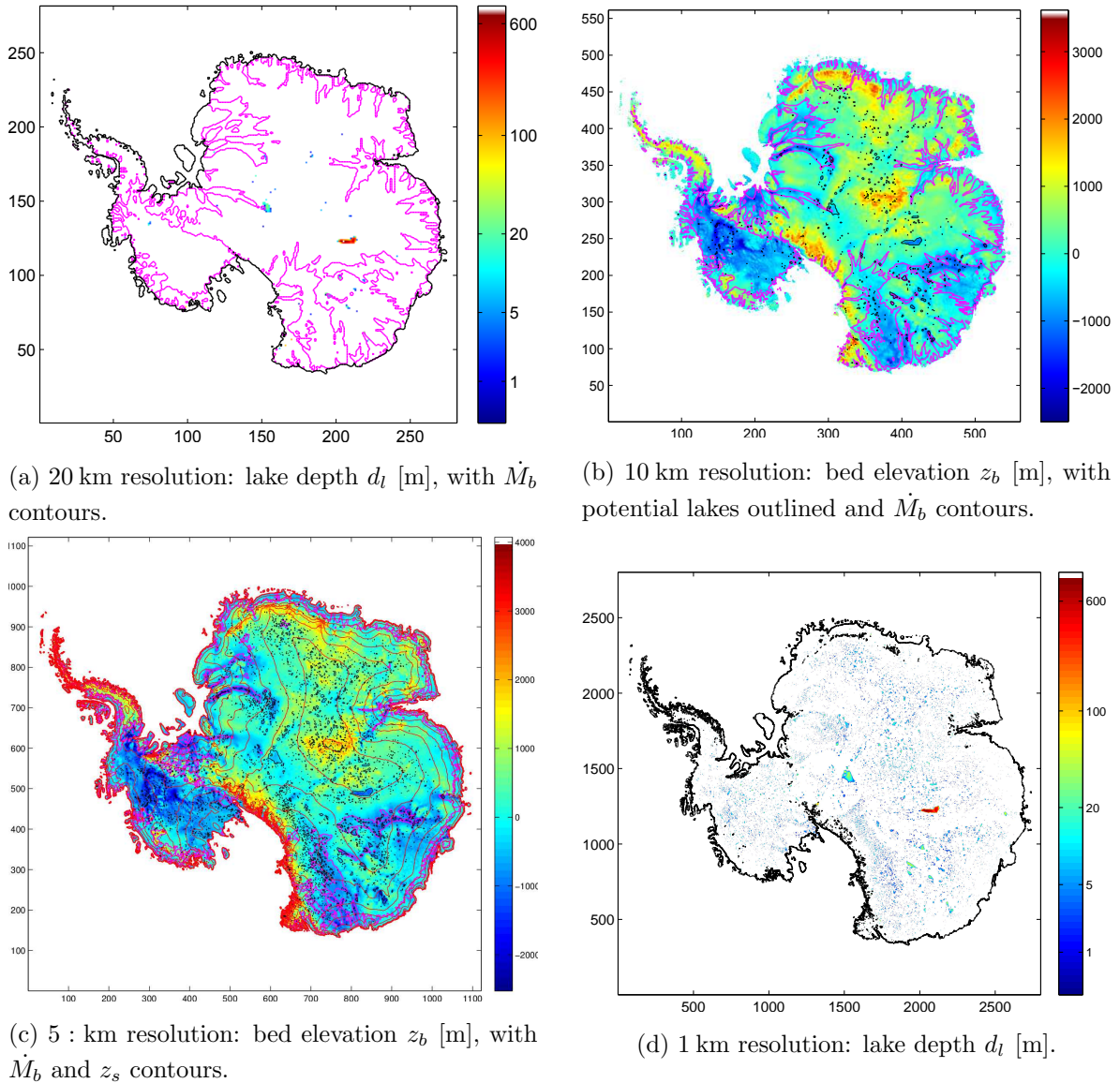


Figure 3.9: Depressions in hydraulic potential with lake depth d_l [m], together with \dot{M}_b , z_s and z_b contours for different resolutions

- Flux definition: blue zones occur more frequently, mainly scattered along the ice divides. These indicate local maxima in the hydraulic potential, where fluxes cannot be calculated, since there is only outgoing water. In the BWM, a cell that only produces outgoing water has no flux. This is again especially the case in rough, well-sampled regions like the Gamburtsev mountains (black circle in Fig. 3.10d).

Overall, similar to the analysis by Livingstone et al. (2013), several flux patterns can be seen:

- Convergent: typically near fast ice streams that lower the surface (and thus the potential) locally. This creates steep potential gradients and draws water in (Byrd Glacier, Recovery Glacier).
- Dendritic: relatively smooth zones in the hydraulic potential, where no typical controlling factor is present (EAIS).
- Parallel: a gentle sloping surface is dominant, little bed roughness (Siple Coast).

Lastly, although the flow patterns get increasingly finer, maximal discharges do not increase with finer resolution, for two possible reasons. First, since little extra data are added over 5 km, pathways remain multiple cells wide on 1 km for example. Secondly, the detail that is added is used to split pathways rather than gather them, giving the water more outflow options instead of concentrating discharges.

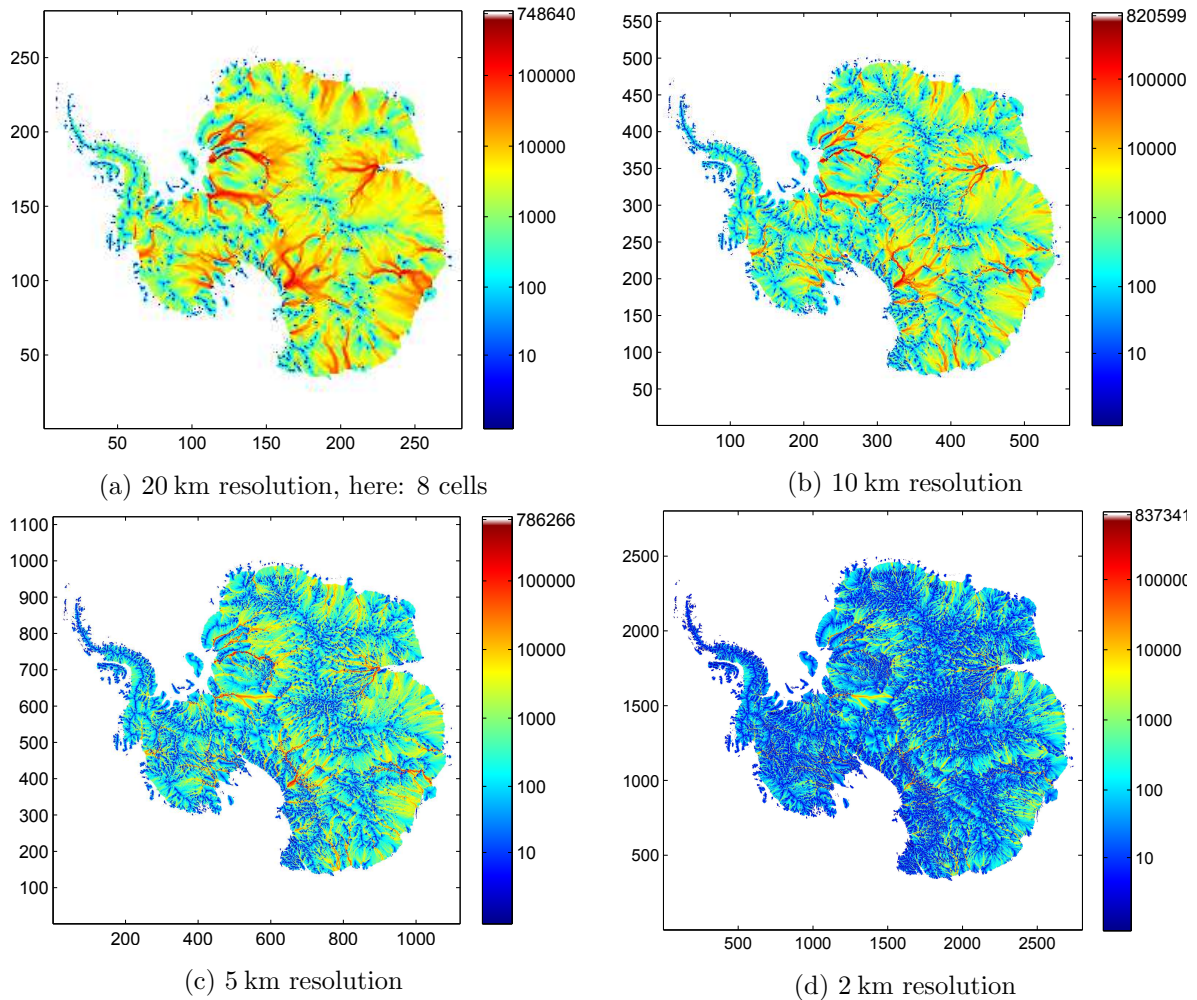


Figure 3.10: Water flux $10^3 \Phi$ [m^3/year] for different resolutions assuming a uniform \dot{M}_b of $1.10^{-3}\text{m}/\text{year}$

3.2.3 Cold vs. warm-based ice

Previously in the ISM, in order to reach a situation where all water flows to the coast, ice-covered regions where no basal melting ($\dot{M}_b = 0$) occurs are considered inaccessible to basal water, since the simulated basal temperature gradient is insufficient to melt water. This causes some water to get blocked underneath the AIS where warm-based regions are not connected to the coast. In practice, most water refreezes and forms basal accreted ice, blocking eventual pathways under cold-based ice. Some observations suggest very thin water films even under cold bedded ice (Palmer et al., 2013). Using a Shapiro-Ritzwoller GHF on a 10 km resolution (Fig. 3.4), \dot{M}_b is simulated, and a scenario was set up where the water is allowed to flow under cold-based ice in the BWM. It can be seen that some pathways through cold ice might connect warm-based zones (Fig. 3.11).

The differences between cold-based throughflow or not gives a rough estimate of the basal accretion originating from water melted at the bed of the AIS, a phenomenon also reported in literature (Bell et al., 2002). As these melt regions get narrower, because of more detailed simulated basal temperatures at finer resolutions, cold ice regions tend to be situated more in or around warm-based zones. Consequently, the amount of water flowing out from warm-based through cold-based ice regions gets larger (Table 3.3). Note that the mass imbalances are not the same as in Table 3.2, since instead of a uniform \dot{M}_b , a realistic estimate was used here. Note that serious errors were observed in the 5 km ISM run, so these results might not be reliable.

3.2.4 Coupling with ISM

Ultimately, a coupling between the ISM and BWM could potentially be interesting, considering the link between basal water flow and ice velocities. In practise, this could be done through linking an output of a BWM run, performed for every interval during which the ice sheet geometry might change significantly (decadal timescale for example), to ISM input fields governing basal sliding for example (Hewitt, SVALI, personal communication). Two factors to consider are sensitivity towards the use of ISM geometric input vs. observed geometries, and deciding on which field might be suitable for passing to the ISM. Sensitivity towards ISM

Table 3.3: Total potential water flow under cold-based ice for different resolutions, Antarctica

Resolution [km]	Mass imbalance		Difference
	Cold throughflow	No cold throughflow	
20	0.00043 %	1.673 %	1.673 %
10	-0.0269 %	3.855 %	3.876 %
5	0.00363 %	5.113 %	5.109 %

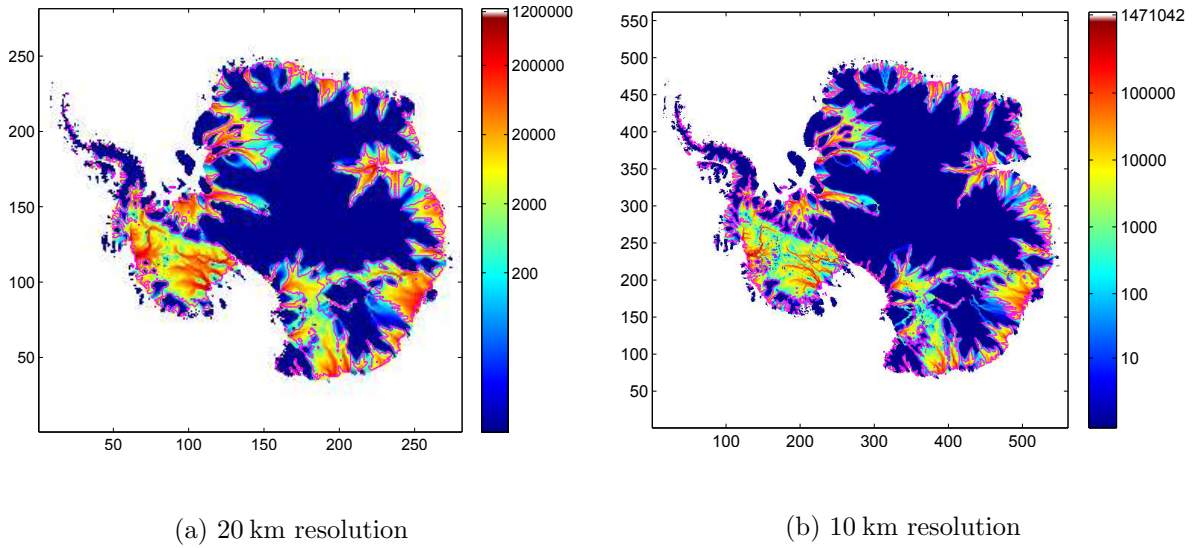


Figure 3.11: Water flux Φ [$10^3 \text{ m}^3/\text{year}$] under warm- and cold-based ice using a Shapiro GHF on 20 and 10 km resolution.

geometric input will only briefly be touched here since this was already discussed by Vanderstocken (2010). A potential link could be made between water velocities u_w and ice velocities \bar{U} , similar to the sliding slaws discussed in the first chapter.

ISM geometries

Geometries obtained from the ISM should only be used with caution to predict subglacial lakes. There is a large difference between lakes identified using the observed geometry (Fig. 3.9b vs. Fig. 3.12a). Since lakes are formed through surface or bedrock irregularities, a smoother surface means there will be less lakes using an ISM geometry. Only few remains of Lake Vostok and the South Pole lake can be seen here, since large errors z_s are present near the South Pole, and Lake Vostok was filled explicitly for ISM applications.

For comparison of drainage pathways, the 10 km experiment was used, because of some pronounced overestimations in the 5 km run (Fig. 4.2b). Water fluxes Φ and velocities $\bar{\mathbf{u}}_w$ from the geometry out of the ISM tend to spread out more than the ones obtained with modified BM2 data (Fig. 3.12b) The largest differences can be seen in regions with errors in z_s like Siple Coast or throughs like Byrd Glacier. Here, the ISM will not resolve the details of z_s that govern the water flow in reality.

Finally, water velocities or fluxes can be related to basal sliding U_b , as illustrated by the sliding laws in Chapter 2. Therefore, it is important to know basal sliding velocities \mathbf{U}_b . However, for this thesis, only ISM output is used, with basal sliding as a boundary condition. In output fields, basal sliding is calculated through multiplying vertically averaged ice velocities with a

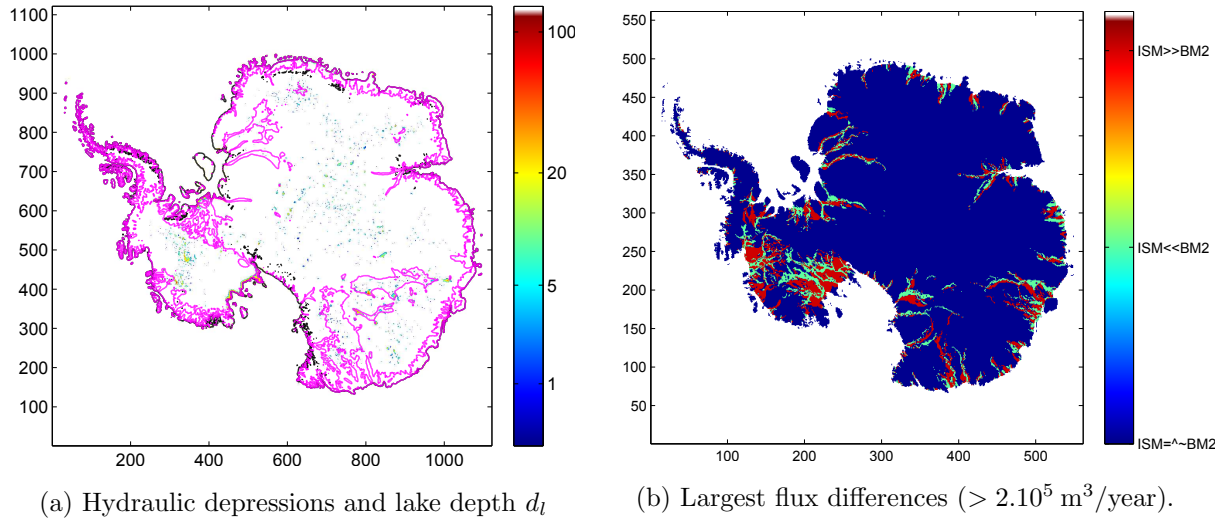


Figure 3.12: Lake prediction and differences in flux routing between BM2 input and ISM input data, on a 10 km resolution.

partitioning coefficient between basal sliding and internal deformation (Fig. 3.13). Although a clear link is seen between \mathbf{U}_b and water velocities $\overline{\mathbf{u}_w}$.

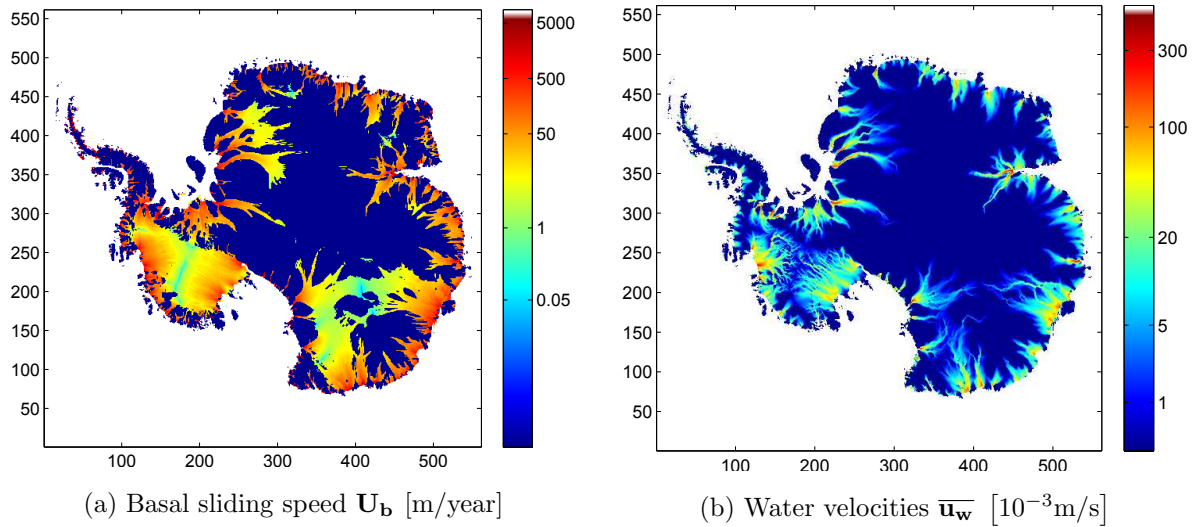


Figure 3.13: Comparing basal sliding and water velocities, using ISM geometries obtained on 10 km resolution.

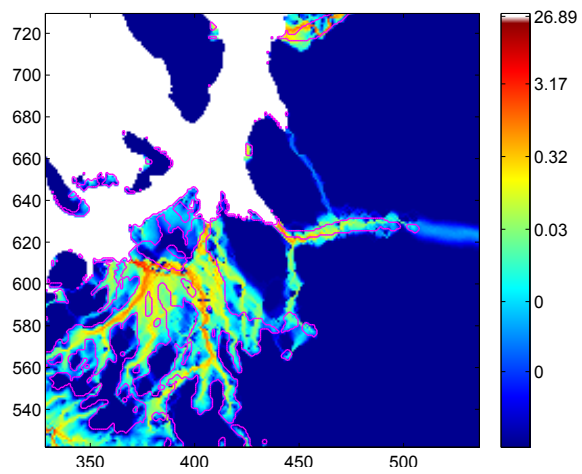
3.2.5 Realistic estimations and validation

When using \dot{M}_b obtained by the ISM (Fig. 3.4), results represent an estimation of the actual water fluxes, considering a Weertman film morphology (Fig. 3.11). Remember that for the

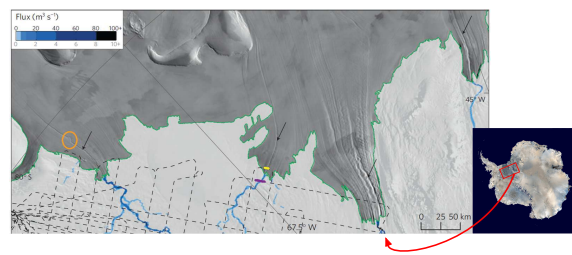
highest resolution, Lake Vostok and South Pole Lake remained unfilled. Since these are situated in a cold-bedded zone where no water flow, mass imbalance is very low (0.00363 %). When making realistic estimations of basal water fluxes, two remarks need attention again.

- The ISM produces inconsistencies, for example near Siple Coast, so that the \dot{M}_b obtained in such regions is based on a false geometry and do not agree with a realistic scenario.
- In reality, water will not flow in a continuous Weertman film. When modelling interaction between basal water and ice, understanding the governing process correctly is vital. As shown for many places in the WAIS, the sediment is soft (Clarke, 2005), which might lead to higher sliding velocities through increased sediment deformation, rather than through increased basal sliding on a thin water film over the bedrock.

Validation data for a basal water system are scarce and the subglacial processes remain uncertain. Aside from comparing lake distribution and sizes (Wright and Siegert, 2012; Livingstone et al., 2013), recent discoveries indicate channels arising under ice shelves, originating from a basal water system reaching the grounding line and melting cavities. These observed outflow locations can be compared with the drainage networks obtained from the BWM. One example used here are the ice shelf channels under the Filchner-Ronne ice shelf as recently detected by satellite images (Le Brocq et al., 2013). Here, subglacial water leaving the ice sheet interacts with local ocean currents, leading to the melt of cavities beneath the shelf. As the ice shelf advances over the grounding line, these features are expressed at the surface of the ice sheet as line-shaped depressions. The locations of these features match previous modelling work, and also this BWM proves adequate in locating them. Note that the actual discharge fluxes are smaller (up to $25\text{m}^3/\text{s}$) than the one obtained by Le Brocq et al. (2013) (up to $80\text{m}^3/\text{s}$), but here we still have outflow through multiple 5 km cells. Further work will be done estimating the fluxes needed to melt out such cavities, so more quantitative validation for basal water modelling is possible in the future, as well as understanding in how this basal water affects ice shelf dynamics.



(a) 5 km resolution BWM flux, now in m^3/s !



(b) satellite images (Le Brocq et al., 2013)

CHAPTER 4

Greenland: basal water model applications

4.1 Dataset

4.1.1 Geometric data: Bamber 2013

The Bamber 2013 dataset provides the most recent surface elevation z_s , bedrock elevation z_b and thickness H dataset covering the entire Greenland ice sheet (GrIS) (Fig. 4.1). As BM2, it is available up to 1 km resolution. z_b is calculated in this dataset, from accurate satellite altimetry z_s measurements and accurate H radar measurements. For the mountain glaciers and peripheral ice caps, no ice thickness data are included and $z_s = z_b$. Because of denser coverage, errors are smaller than for the AIS and range from 10 m near ice core sites up to 100 m in the interior part of the GrIS. Note that similar to BM2 data, the spacing between flight lines can be more than 50 km (Bamber et al., 2013a). The negative bedrock elevation in the center of Greenland indicates a potential source of instability for the GrIS, similar to the WAIS situation.

Based on these data, a mask was constructed (Fig.): 1 for the continuous ice sheet, 3 for land mass and mountain glaciers and 4 for ocean points. The mask was chosen to resemble the mask used in the BWM for Antarctica, with the bare land in Greenland treated similar to Antarctic cold-based ice. These regions are of little interest in our application, and no reliable water production field is available for these regions. Similar to the AIS, water flow can be allowed through them, in this case simulating overland flow.

Consistent thickness and floating for ice shelves and grounded ice was already ensured for this dataset. In the original data a 10 m firn correction was already applied, together with assumptions of hydrostatic equilibrium. Furthermore, specific adaptations for compatibility with the ISM were performed already, for example shifting ρ_i to 910 kg/m^3 again.

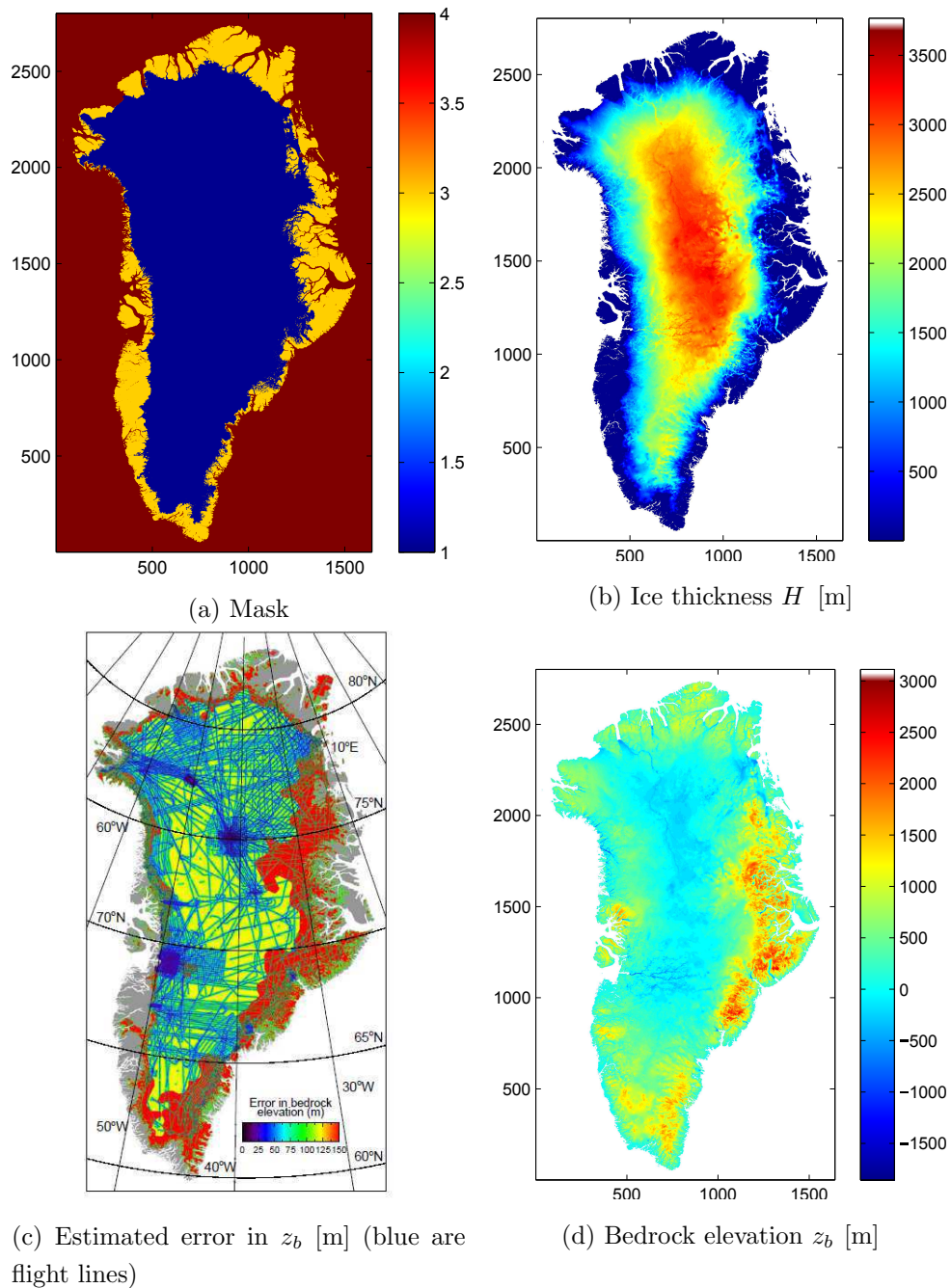


Figure 4.1: Bamber 2013 data fields on a 1 km resolution, together with constructed mask and data coverage.

To test the performance of the Bamber dataset and obtain input fields, again an ISM experiment identical to the one for the AIS was set up on 20, 10 and 5 km. Similar to the AIS, the ISM overestimates ice volumes in fast-flowing ice streams, probably again due to too slow drainage of the ice or numerical artefacts. This error declines again with increasing resolution

(Fig. 4.2). Another systematic error running N-S in South East Greenland might be due to the uncorrect simulated location of an ice divide.

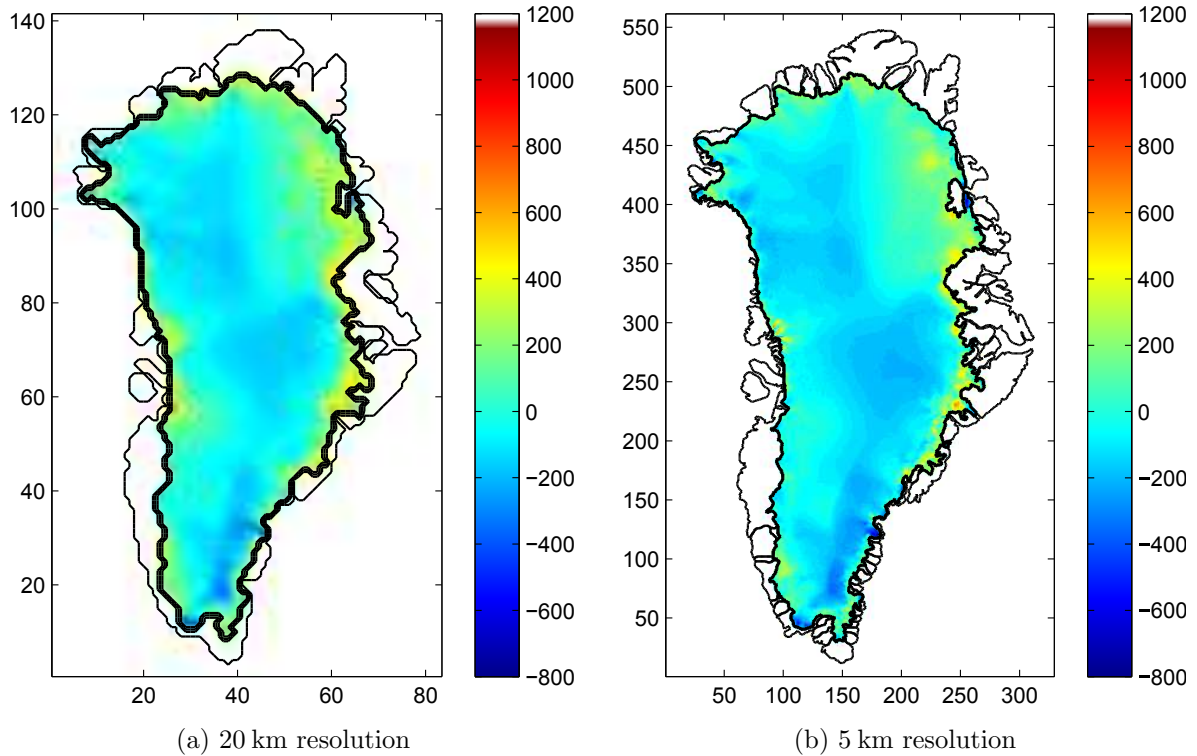


Figure 4.2: Difference between the ISM output [m] for a fixed geometry experiment, using adapted Bamber 2013 data, and the original Bamber 2013 data. Higher values indicate ISM overestimations.

4.1.2 Modelled data: basal melting rate and surface runoff

Next to the geometries discussed above, ISM simulations using the Bamber 2013 data also led to basal melting rate \dot{M}_b and runoff R estimates (Fig. 4.3). For \dot{M}_b , several estimates of the GHF are available, where we used the Shapiro estimate again based on consistency with other ISM applications. This GHF is corrected for locations around 4 ice core drilling sites where temperature profiles are known, as seen in the circular \dot{M}_b pattern in Central North Greenland, situated at and corrected for ice temperatures measured in the NGRIP ice core (Goelzer et al., 2013).

As this \dot{M}_b is calculated based on ISM geometries again, it will not be correct when applied to observed geometries, although errors for GrIS ISM simulations are more along the margins compared to AIS errors. This basal melting will produce water far inland. Near the margins, runoff is by far the dominant term in meltwater production (Fig. 4.3b).

Surface runoff R is calculated as the volume of water that is left of surface melt after storage in the snowpack, using a Positive-Degree-Day (PDD) model. Since this requires ice, runoff fields cannot be defined at locations outside the ice sheet (Fig. 4.3b). Typically, runoff occurs after melt reaches more than 60% of precipitation, which only occurs over the margins of the GrIS (Goelzer et al., 2013). Although quantitatively, these fields might be usable, in reality, melt only occurs in summer periods. Similarly, outbursts of supraglacial lakes provide a large variability in the timing of meltwater reaching the bed, varying on weekly timescales (van de Wal et al., 2008). We assume runoff reaches the bed at its point of origin, thus using an upper estimate for runoff. In practice, this is a valid assumption, considering the nearly vertical moulins and hydrofractures observed at the surface (Åström et al., 2013). Finally, it is worth pointing out that the runoff calculations are done at the beginning of an ISM experiment using observed geometries, this in contrast with the basal melt rates, calculated at the end of the simulation, based on modelled geometry again.

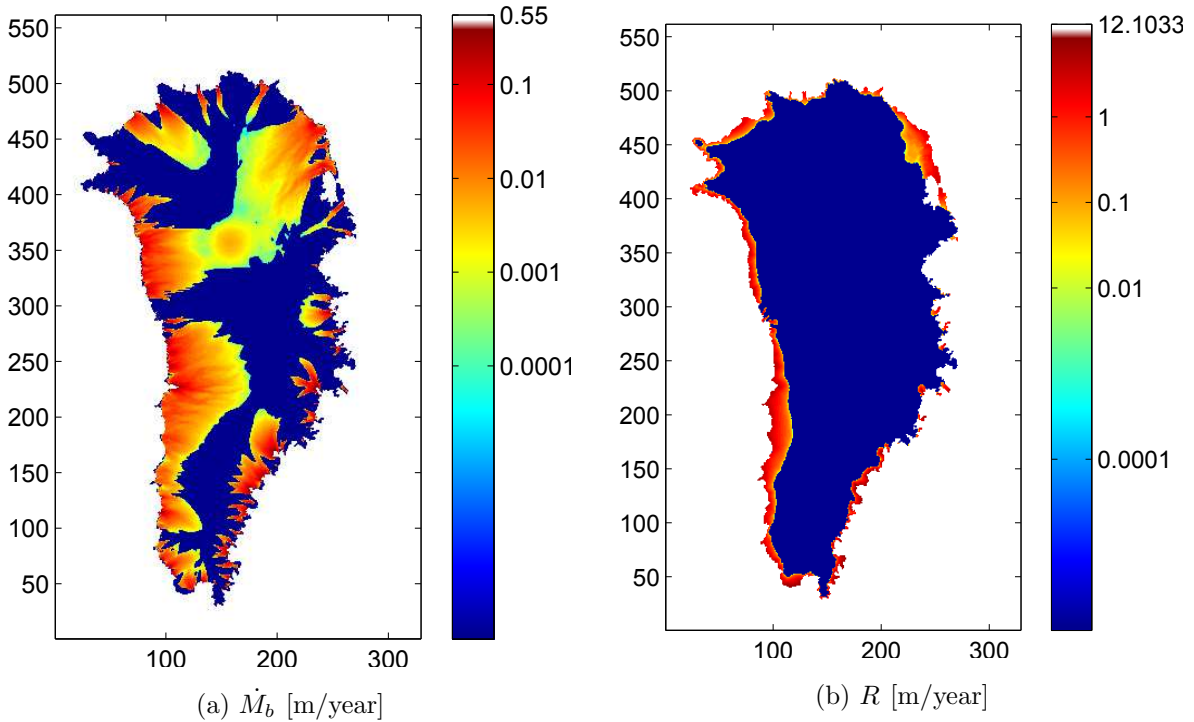


Figure 4.3: Basal melt rate \dot{M}_b and runoff R fields for Greenland obtained with simulations using Shapiro-Ritzwoller GHF, on a 5 km resolution.

4.2 BWM experiments and results

Since the BWM was only applied to Antarctica so far, some refinements were made to ensure applicability on Greenland, like changing grid sizes, masks and indexing. In a first approach

for the GrIS, a uniform \dot{M}_b of $1 \cdot 10^{-3}$ m/year was applied on a 5 km resolution, which led to water routing and flux patterns (Fig. 4.7a) very similar to ice velocity fields. The ice divides, the fast outlet glaciers, as well as the far inland penetrating NEGIS can all be seen very clearly. Since \dot{M}_b values are again uncertain, some of these features might be present or might have been in the past. The visible pathway under Jakobshavn Glacier has been suggested to be a paleofluvial feature (Bamber et al., 2013a). Note that compared to the AIS, the smaller GrIS produces up to a four times lower water flux and velocity. (compare to Fig 3.5).

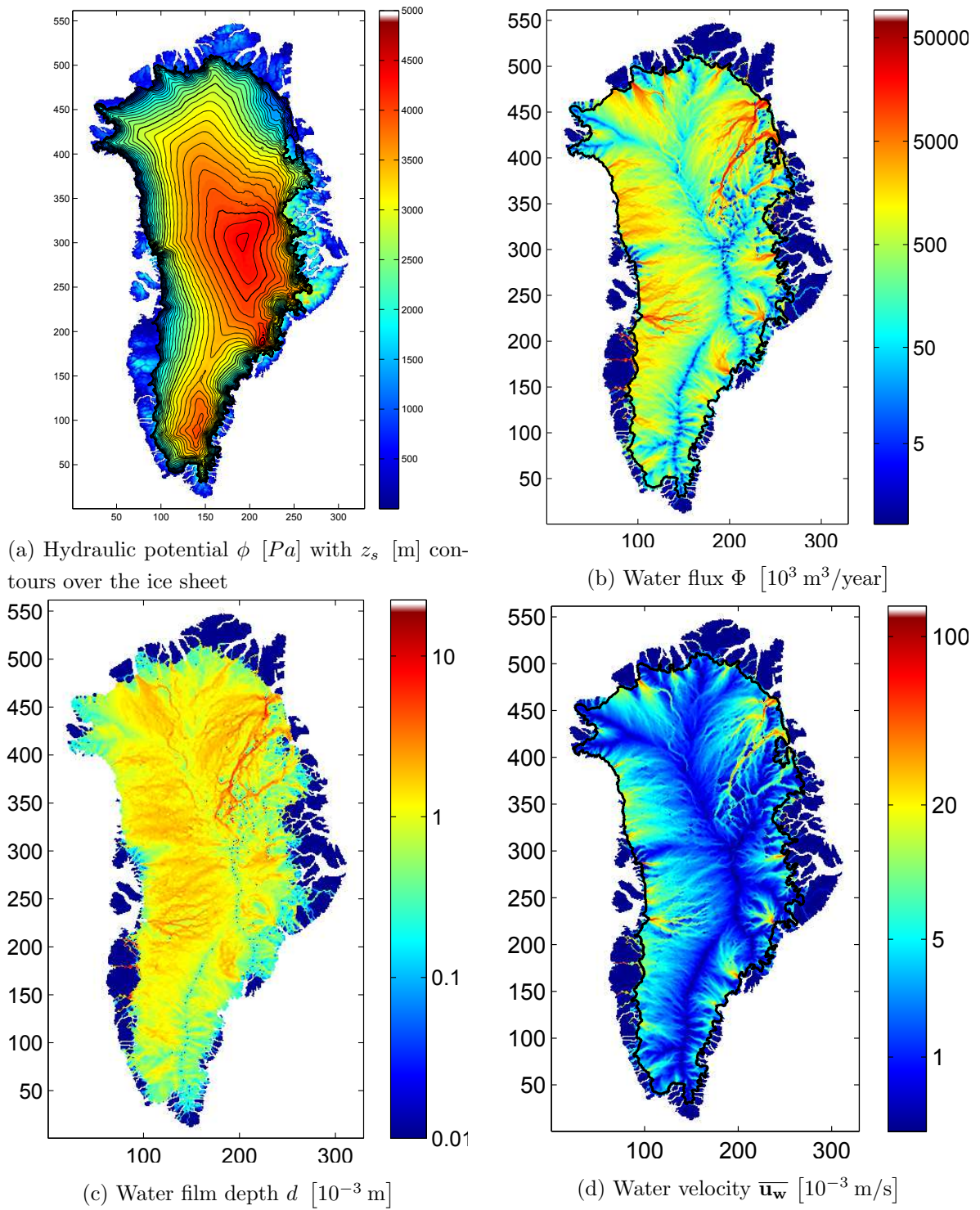


Figure 4.4: BWM output fields on 5 km resolution using adapted BM2 data and a uniform basal melting rate \dot{M}_b of $1 \cdot 10^{-3}$ m/year.

4.2.1 Hydraulic depressions: potential lakes?

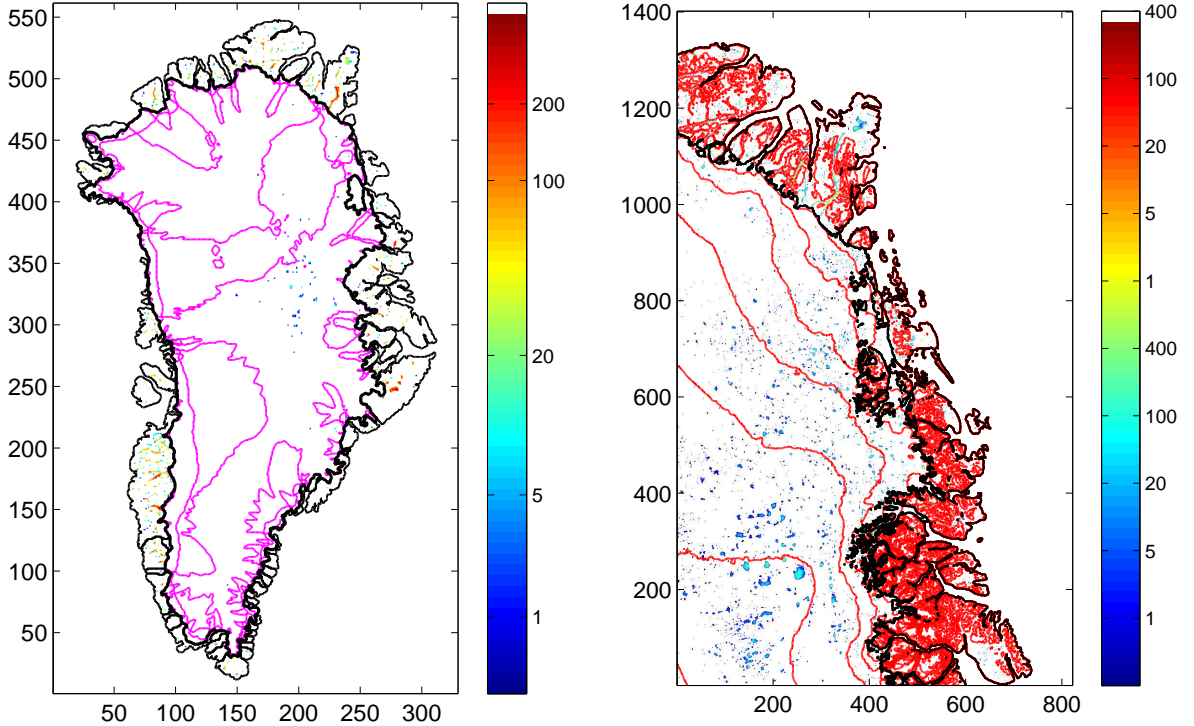
The most efficient filling algorithm is applied further here, using 8 surrounding cells and a precalculated field with the filled ϕ depressions, using Planchon's algorithm. Initially, a random factor is added to the bed again such that less problems with flat spots arise during the filling procedure. An overview for all resolutions is given in Table 4.1. Again, an increasing number of lakes was found with increasing resolution (Fig. 4.5), but because of the steeper surface gradients, water is pushed out more easily and little to no lakes on resolutions lower than 5 km are found (Livingstone et al., 2013). Most hydraulic depressions lie outside of the regions with basal melting or runoff production. For Greenland, lakes can also exist under cold-based ice through the seasonal water supply by runoff reaching the bed (Palmer et al., 2013), so excluding lakes outside a melt zone might be preliminary again. A cluster of lakes is detected on the onset of the North East Greenland Ice Stream NEGIS, possibly confirming theories and observations pointing towards meltwater-enhanced basal sliding (Keisling et al., 2013). Most potential lakes are found in North-East Greenland, due to the rough z_b that was mapped with a high degree of coverage (Fig. ??). In case overland flow should be accounted for, depressions on bare land are also filled, including some deep valleys. For the purpose of the BWM, filling depressions outside the ice sheet allows water to flow from underneath the ice sheet, all the way to the ocean. This also facilitates the prediction of some of the lakes present on the South East Greenland periphery. However, in the Bamber 2013 data, regions outside the GrIS were not mapped in detail, so it is uncertain whether these depressions exist in reality.

4.2.2 Effect of stress partitioning and surface positive feedback

As mentioned by several authors, there might be a difference between the ice overburden pressure (weight of overlying ice column) and the pressure felt at the bed (Le Brocq et al., 2006). Allowing for stress partitioning through longitudinal and bridging stresses (Fig. 2.4), the pressure felt locally at the bed might be the result of the averaged weight of the ice column

Table 4.1: Depression-filling results and further improvements for all resolutions, on Greenland

Resolution [km]	iterations	mass imbalance
20	5	-0.000124 %
10	18	0.000232 %
5	68	-0.0250 %
1	> 6000	0.350 %
1	> 60000	-0.0887 %



(a) 5km resolution: \dot{M}_b and R contours (Fig. 4.3), lake depth d_l [m].

(b) 1km resolution: lake depth d_l and z_s contours in red, NE GrIS.

Figure 4.5: Depressions in hydraulic potential, \dot{M}_b and dependency on z_s and z_b for different resolutions

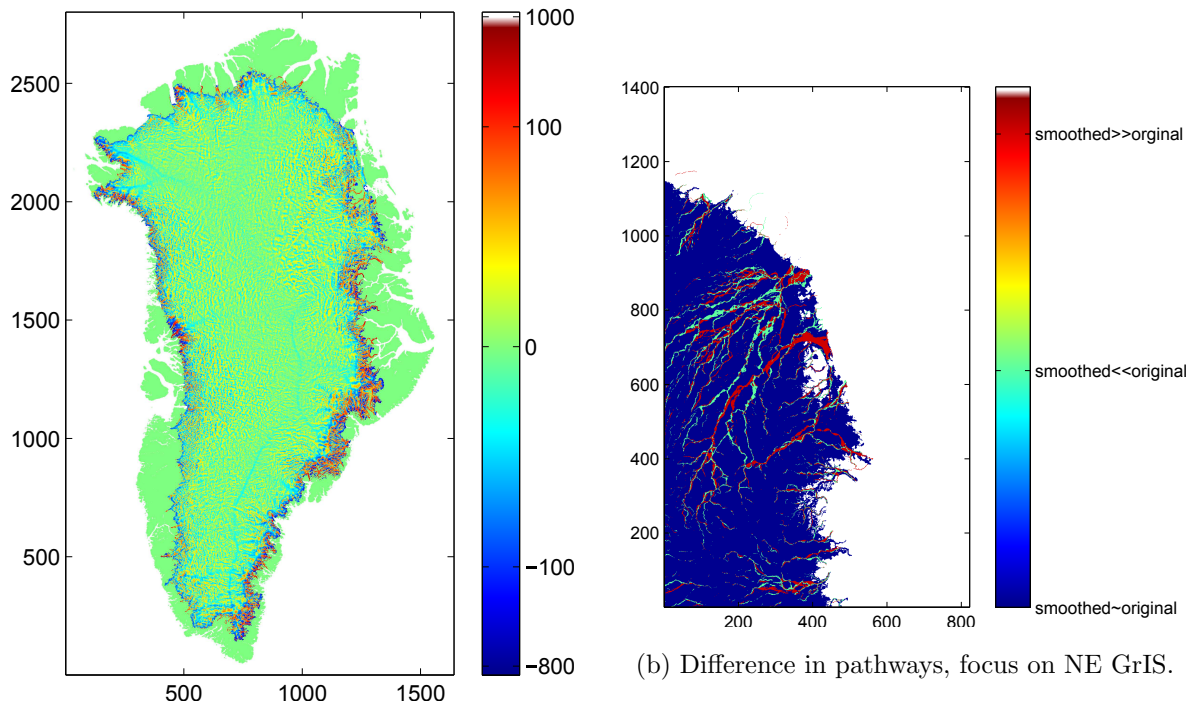
at that location. In this way, irregularities in the surfaces (ice rises for example) might not be transferred to the bed and subglacial water. Cuffey and Paterson (2006) suggested the bed only feels surface variations over a distance of 10 times the ice thickness, corresponding roughly with a 10 or 20 km resolution for Greenland.

Smoothing might also exclude a circular reasoning in identifying lakes, since a positive surface feedback exists between ice flow and subglacial lakes. As a lake is formed, the upper ice surface flattens out as the ice column floats hydrostatically (clearly observed over Lake Vostok). This could preclude the detection of the potential features that caused the hydraulic depressions in the first place (Livingstone et al., 2013). Both the stress partitioning and positive feedback can also take place over Antarctica, but since surface slopes are more dominant for basal water flow under the GrIS, the effect will be discussed here. For Antarctica, results of this experiment were similar to Fig. 3.12b, since an ISM output is also smoothed relative to the data.

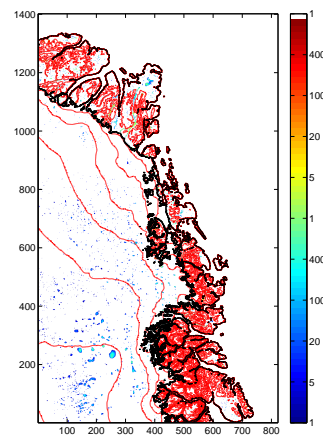
To simulate this smoothed z_s on Greenland, a Gaussian filter with a kernel size of 20 cells, thus simulating stress partitioning over 20 km was applied to z_s (done using using the GMT mapping software). Ice thickness H was recalculated from the difference between the smoothed

thickness and the non-smoothed bed. This only caused major differences close to the coast, where in practise longitudinal and bridging stresses are also greatest (Fig. 4.6a). Smaller kernels of 5 and 10 cells were also tried but presented little change, indicating this smoothing might of limited relevance for basal water flow und the GrIS.

For the hydraulic depressions (compare Fig. 4.6c and Fig. 4.5b), both lake outlines and lake depths remain similar over the GrIS, although the number of lakes decreases. Potential lakes originating from surface irregularities will not be present under the smoothed topography. When considering fluxes, a clear difference in pathways for subglacial water can be seen (Fig. 4.6b). Small changes in drainage pathways might affect ice flow significantly, as was demonstrated in the case of water piracy between Kamb and Whillans Ice Stream for Antarctica (Le Brocq et al., 2009). Next to stress partitioning, such small deviations can also be the result of errors in the data or different calculation methods (for example Fig. 3.6).



(a) Difference in z_s when smoothing is performed.



(c) Lakes and depth d_l under smoothed surface

Figure 4.6: Difference between a smoothed surface using a 20 km Gaussian kernel, and the 1 km original Bamber2013 data, and influence on routing basal water flow

4.2.3 Fluxes: resolution and partitioning basal melt and surface runoff

The resolution effect is very similar to the one observed on Antarctica. Local maxima in hydraulic potential along ice divides and rough surface regions clutter the images again, and pathways get finer in regions with good data coverage. One interesting factor is the use

of a paleofluvial canyon, delineated after the release of the Bamber 2013 dataset (Bamber et al., 2013b). This canyon is 750 km long, with a depth and width up to 800 m and 10 km respectively. It was demonstrated to be a conduit for basal water in present day-geometry and during both ice-free periods and the LGM. This conduit is also revealed here when using a uniform \dot{M}_b or when allowing for flow through cold-based ice (Fig. 4.7b). On lower resolutions, we can use simulated runoff and BMR values to illustrate realistic estimations of the basal water flow und the GrIS.

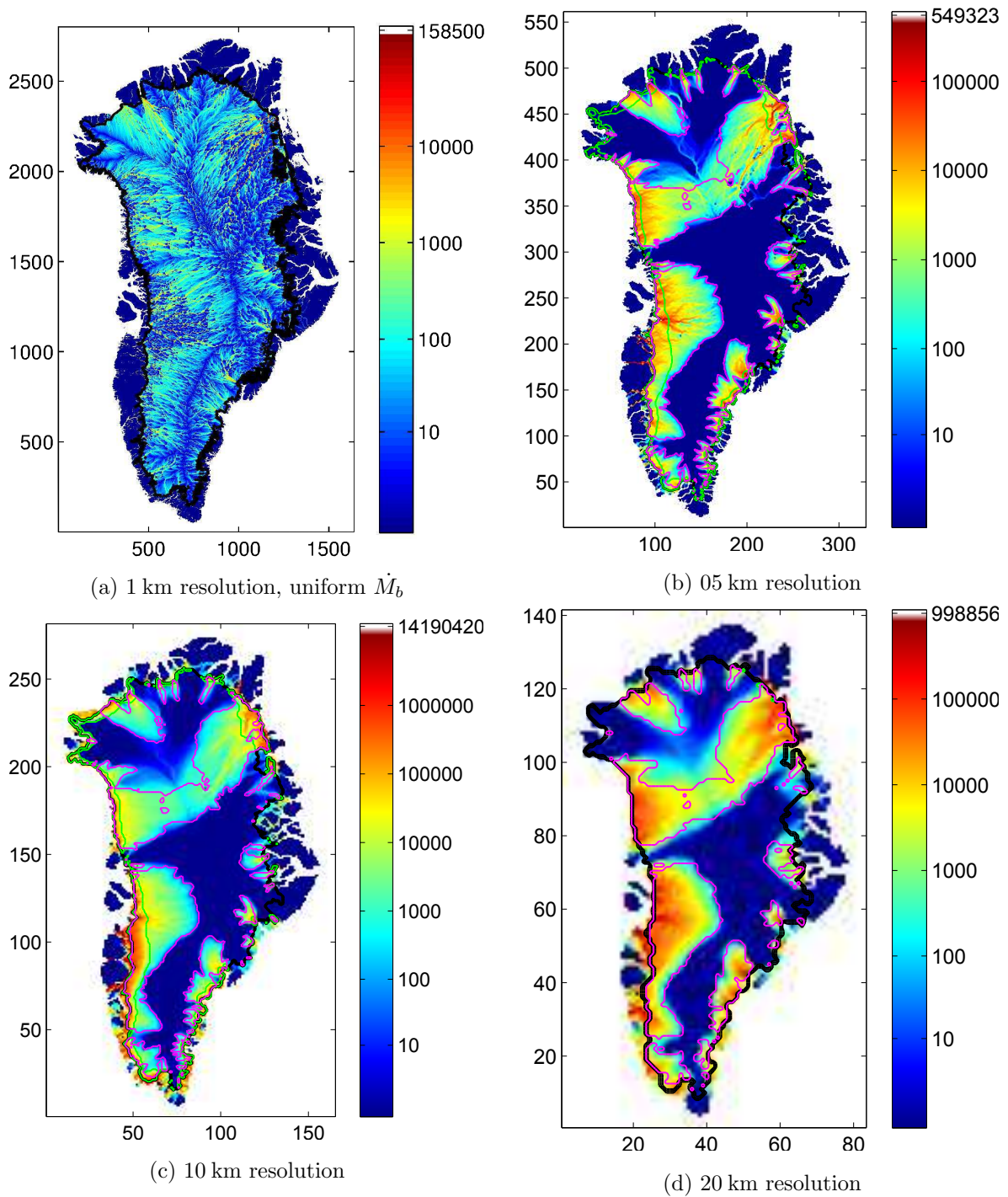


Figure 4.7: Water flux Φ [$10^3 \text{ m}^3/\text{year}$] for different resolutions assuming a realistic \dot{M}_b (inward between magenta contours) and runoff R (out towards the coast from green contours) obtained from ISM output

4.2.4 Coupling with ISM

Coupling basal water flow, derived from runoff, to ice flow would not make sense in this case. No correlation has been observed between annual ice flow velocities and annual velocity fields, in contrast to what was previously thought (Zwally et al., 2002). Meltwater production and ice flow only vary together on shorter timescales, in the order of weeks (van de Wal et al., 2008), through sudden speedups which cannot be simulated by the ISM used here.

ISM geometries

Under an ISM geometry, the same lakes on the onset of the NEGIS arise as depressions in the hydraulic potential, indicating the stability of these lakes under different ice sheet configurations. On the highest resolution of 5km, the basal water fluxes obtained using ISM input differ significantly from the ones under observed geometries. Some key features like the paleofluvial canyon remain present, and might drain water from a warm-based zone, underneath cold-based ice and out underneath the Petermann glacier. When comparing with Fig. 4.7b and similar to the AIS, pathways again get smoothed out, and discharge is generally lower in the broader water routes when using ISM geometries, confirmed by the difference between large drainage pathways (Fig. 4.8b). Because of underestimated ice flow through outlet glaciers, the thicker ice produces steeper potential gradients near the margin of the GrIS, instead stretching those gradients out further inland. This results in a water flux that is higher near the coast and does not reach far inland (see NEGIS, Fig. 4.8b).

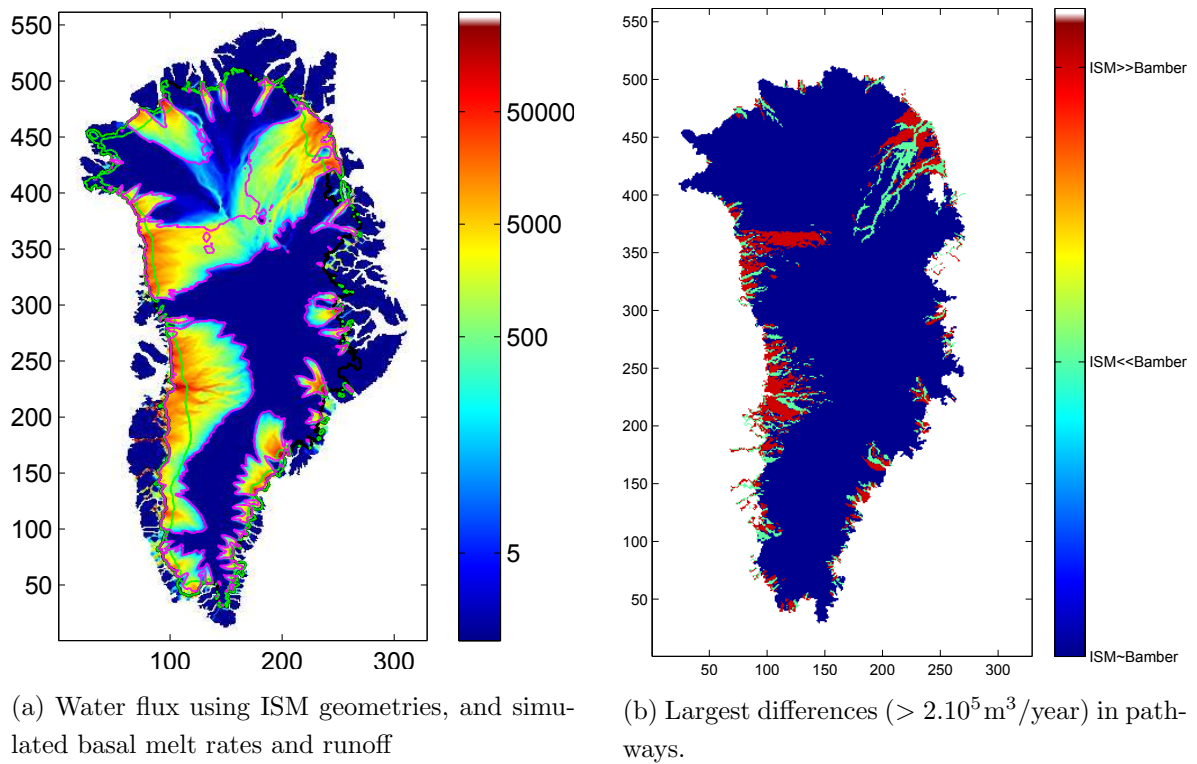


Figure 4.8: Differences in flux routing between Bamber2013 input and ISM input data, on a 5 km resolution.

CHAPTER 5

Spatially explicit channel model

5.1 Introduction

Aside from the Weertman film flow, a second widely accepted hypothesis involves channelized flow. Both mechanisms might occur simultaneously under ice sheets, and switches in drainage systems have been shown (Schoof, 2010; Irvine-Fynn et al., 2011). Therefore, an interesting way of looking at channel flow was sought, and a first spatially explicit model (SEM) for this kind of process was developed. Spatially explicit modelling involves a continuous spatial domain, where no grid or graph is used to restrict the spatial degrees of freedom. When considering discrete time steps and state, this model can be classified as an agent-based model (Baetens, 2012). The work of Hafver et al. (2014) served as a source of inspiration, as it mimics fracture propagation on a graph, with the purpose of improving fracturing techniques in deep-well gas and oil exploitation. After randomly locating starting points for fractures, gas propagates through the fractures according to the diffusion equation. When the internal pressure is sufficiently high, the fracture is allowed to grow. Intersecting fractures can only continue in one direction.

Spatially explicit modelling is a relatively new spatio-temporal modelling paradigm, of which the use is still largely confined to ecology and hydrology (Grimm and Railsback, 2013). In the framework of channel flow, the evolved network consists of connected segments that make up channels. For a given hydraulic potential field, and water sources, the model simulates channel formation in a stochastic and spatially continuous way. The spatially explicit paradigm seemed appropriate to model channel-based flow under ice sheets for several reasons.

- Firstly, the dimensions of channels are negligible compared to commonly used resolutions and available data on the hydraulic potential. In this spatially explicit modelling approach, channels lose their physical dimensions and can occupy all possible locations.

- Secondly, the governing variables of basal water flow are typically not known very well, or not available (for example bedrock elevation z_b , bed roughness, etc.). Values outside flight lines or measuring points are interpolated and can be treated in a stochastic way.
- Thirdly, exact locations of water input, such supraglacial lakes or moulins, can be delineated easily through satellite or ground observations (Fig. 5.7). This makes it feasible to follow individual channels and consider their local interactions.
- Fourthly, SEMs are ideal to account for individual variability and local interactions, which are crucial in the case of channel flow.

5.2 Implementation

The SEM was implemented in Mathematica (Version 9, Wolfram research Inc, Champaign, US). There are three main features that deserve particular attention when implementing the spatially explicit channel model, being a realistic network formation, the selection of realistic directions of growth, and keeping track of macroscopic variables that describe the network as it evolves.

5.2.1 Network formation

The network consists of separate channels or pathways P_j . These each consist of n_j segments S_j^i , to which a new segment can be added at every consecutive time step as a consequence of growth or splitting. Splitting occurs after intersection with all segments belonging to other channels. The intersections where splitting should take place are found considering the local and global geometry of the network. Locally because pathways will intersect with the ones closest, whereas a global effect involves for instance pathways that are cut off earlier, causing all downstream intersections to drain suddenly. As such, all segments can depend on each other globally, and multiple intersections can not be retrieved simultaneously, causing computational efficiency to be rather low. In a sense, the network should keep track of its flow and its intersections. Therefore, the network was implemented as a list structure, allowing for all N pathways to have different lengths, with n_1 segments for path P_1 , n_2 for P_2 , up to n_N for P_N :

$$\text{Network} = \{ \{ P_1 \{ S_1^1, S_1^2, \dots, S_1^{n_1} \} \} \{ P_2 \{ S_2^1, \dots, S_2^{n_2} \} \} , \dots, \{ P_N \} \} , \quad (5.1)$$

with

$$S_j^i = \{ \{ \{ x_{j,1}^i, y_{j,1}^i \} , \{ x_{j,2}^i, y_{j,2}^i \} , d_j^i, \text{status} \} \} , \quad (5.2)$$

with $x_{j,1}^i$, $y_{j,1}^i$, $x_{j,2}^i$ and $y_{j,2}^i$ the two-dimensional coordinates of the inlet and outlet point of a segment, d_j^i the discharge (originating from basal melt or runoff) transported through

segment i of channel j , and status being *growing*, *open* or the indices (i, j) of the channel and the segment in which the considered channel flows.

A splitting algorithm was developed, determining the most upstream intersections to be considered at every consecutive time step. The intersection selected is the one closest to the first coordinate $(x_{j,1}^i, y_{j,1}^i)$ of the most upstream segment (S_j^i with the lowest i) of a path P_j (Fig. 5.1). In theory, different routes should lead to the selection of the same intersection, as indicated by the dashed lines. The procedure is designed such that it converges towards the same intersection, irrespective of the search path (green vs. red arrows in Fig. 5.1).

It is assumed that the discharges from smaller segments flow into larger ones, as has been demonstrated for subglacial channels (Cuffey and Paterson, 2006). In Fig. 5.1, the index i of the segments, and thus the global part of the analysis is neglected, which might cause intersections with earlier segments to be neglected. In practice, this is accounted for by sorting the intersections in each channel, such that per channel considered, whereby only the most upstream intersection is withheld per investigated channel. This intersection algorithm was

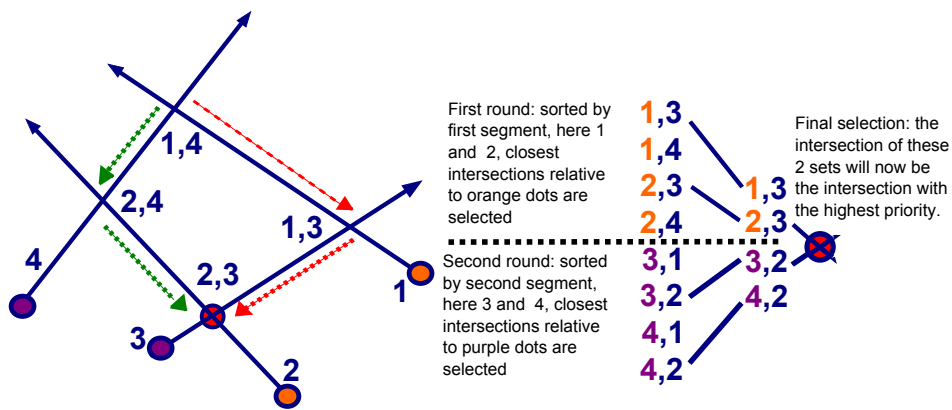


Figure 5.1: Illustration of the intersection algorithm: blue arrows indicate water flows, dots indicate coordinates and numbers represent the indices j of the pathways. The segment indices i are neglected, since the last segment of the paths path, $S_j^{n_j}$.

tested using random configurations (Fig. 5.2).

5.2.2 Selection of the growth direction

For testing the SEM, some geometries for the hydraulic potential ϕ were created, and the potential maps of the GrIS (Fig. 4.4a) were interpolated from a 1 km resolution, in order to arrive at a continuous field for the hydraulic potential ϕ . Based upon this field, a flow direction is selected, upon assuming that the probability of any flow direction is proportional to the gradient in hydraulic potential in the considered direction. The potential gradient

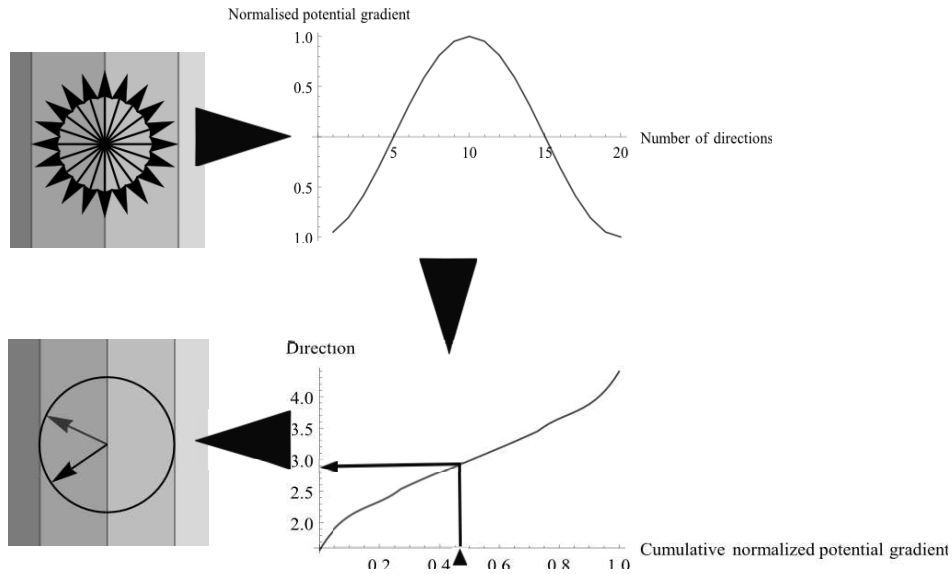


Figure 5.3: Illustration of direction sampling using a PDF of surrounding potential gradients. A value is drawn from the CDF using the inverse transform sampling method. For comparison, the red arrow gives a direction drawn from a uniform distribution with an angular tolerance of π radians.

due to intersection, and their sum (Total), representing the net number of segments added or deleted during each consecutive time step (Fig. 5.6).

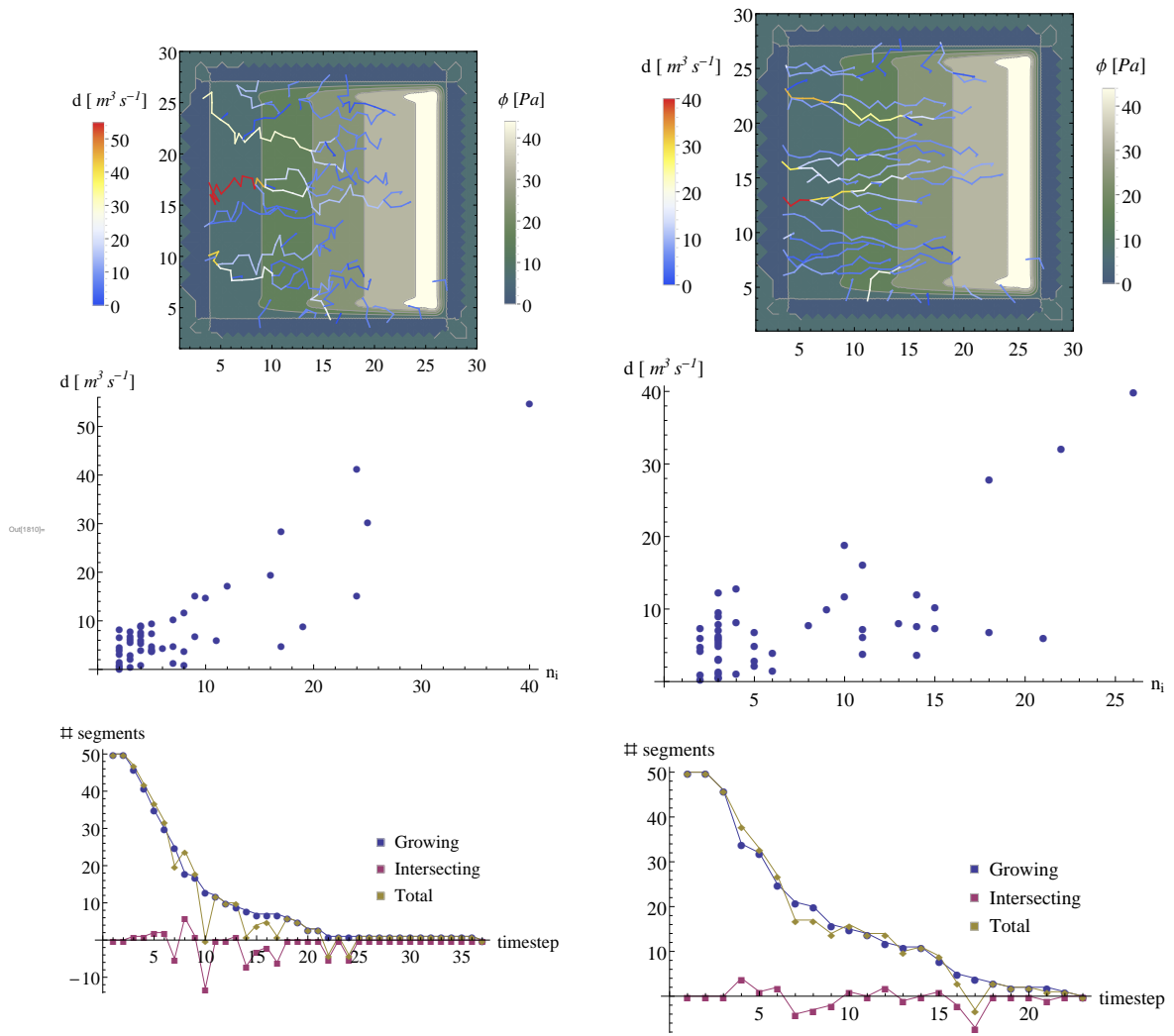
5.3 Proof of concept

A number of geometries representing a continuous hydraulic potential field was generated to verify the intersection and potential sampling algorithms. A first test geometry was a landscape that has a linear slope, providing a straightforward route for water towards the ocean (points where $\phi = 0$). At the three other sides of the region, Dirichlet boundary conditions were imposed in the sense that $\phi = 0$, also along these sides. The linear slope illustrates the intersection procedure and the convergence of channels. Due to the stochasticity in both sampling approaches, water can leave the area along the upper or side boundaries when initial channel outlets are close to these edges. The occurrence of negative values for the total net changes indicate global intersection effects, where channels are cut off and multiple downstream segments are removed from the network.

First, the uniform sampling method was considered, where the effect of different angular tolerances was tested. Through varying this angular tolerance, more or less variability can be introduced in the drainage pathways, causing more outflow along the upper and side boundaries, and less convergence of pathways towards the ocean (Fig. 5.4).

Next, the effect of varying the neighbourhood radius r is illustrated for the PDF sampling method. As r increases, segments reach the boundaries sooner, and relatively fewer pathways will fuse before reaching the sea. Intersections emerge later, since segments require more time steps to reach one another (Fig. 5.5), causing a more gradual decrease in growing and intersecting segments.

The differences between the uniform sampling and PDF sampling are addressed when comparing Fig. 5.4b and 5.5b. The uniform sampling tends to concentrate channels later, since no growth outside the $\frac{\pi}{2}$ angular tolerance occurs. PDF sampling leads to relatively more channels with a higher discharge.



(a) Angular tolerance: π radians

(b) Angular tolerance: $\frac{\pi}{2}$ radians

Figure 5.4: Linear slope, 50 randomly distributed seeds and a neighbourhood radius $r = 1$, uniform sampling effect of angular tolerance. Above: steady-state network. Center: number of growing segments, changes in number of segments due to intersection and their sum (Total), representing the net number of segments added or deleted, versus time.

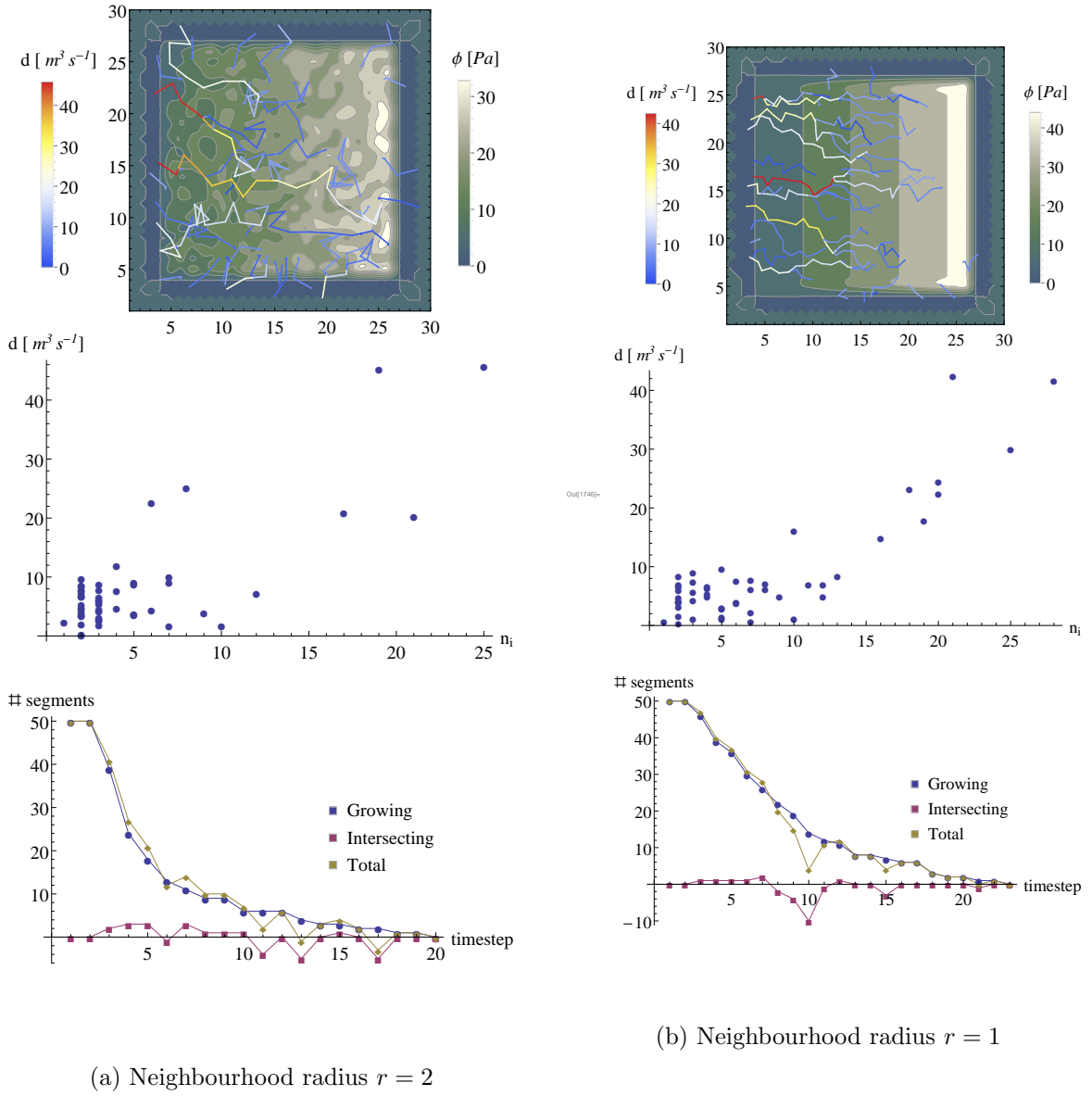
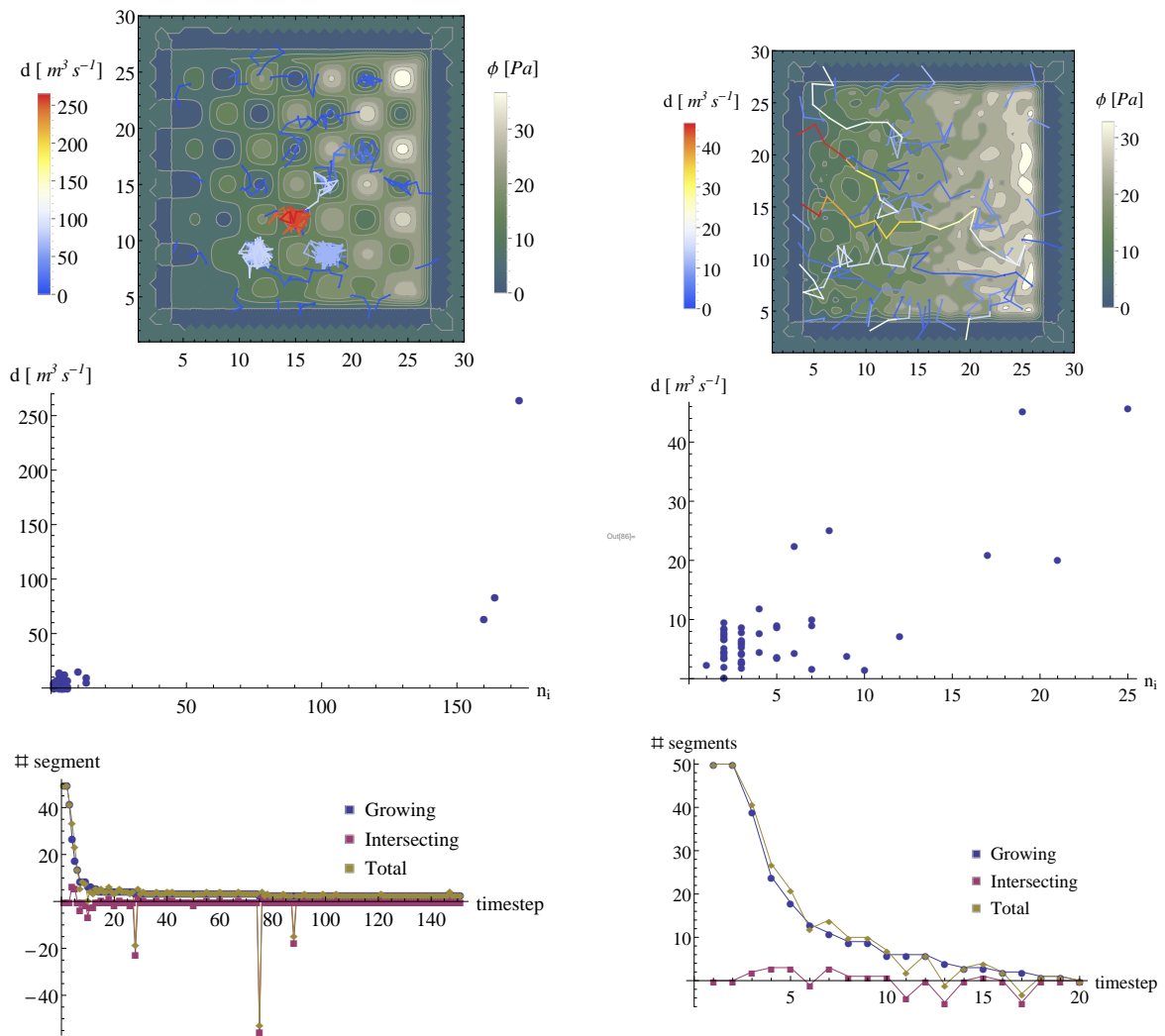


Figure 5.5: Linear slope, 50 randomly distributed seeds and a neighbourhood radius $r = 1$, effect of sampling algorithm. Above: steady-state network. Center: number of growing segments, changes in number of segments due to intersection and their sum (Total), representing the net number of segments added or deleted, versus time.

For a second test geometry, a systematic topography was added to the linear slope, given through a so-called alpine function:

$$f(x) = xy \sin(x) \sin(y) \quad (5.3)$$

In this configuration, the presence of flat regions or depressions becomes obvious from the presence of path clusters (Fig. 5.6a). In flat regions or depressions, the direction of growth is selected randomly, so it can take many iterations for the water to get out. Secondly, a shortcoming of this SEM is revealed in the sense that channels are allowed to intersect themselves, as such causing the messy clusters. A solution to avoid these local problems is increasing the radius r , effectively changing the length of the segments, allowing them to 'see' the potential gradients further away. This would make it more likely that a downward direction is found, and water drains to the ocean. The third and final landscape was generated by adding random irregularities to the linear slope. Results are similar to the ones with the alpine function. Radius r was set higher here, to avoid the clustering in hydraulic depressions as mentioned above.



(a) Alpine + linear slope, neighbourhood radius $r = 1$ (b) Random + linear slope, neighbourhood radius $r = 2$

Figure 5.6: Two other test geometries, 50 randomly distributed seeds, PDF sampling. Above: steady-state network. Center: number of growing segments, changes in number of segments due to intersection and their sum (Total), representing the net number of segments added or deleted, versus time.

5.4 Channel flow under Central West Greenland

The Central West of Greenland has fast ice flows including the Jakobshavn glacier for example, and high runoff production (Fig. 4.3b). It has been shown to be one of the most active regions in terms of ice sheet hydrology (Fig. 5.7). Many dynamic supraglacial lakes and moulines have been observed at the ice surface, indicating englacial and subglacial drainage. This abundance of water also affects seasonal ice-flow variability. In Sundal et al. (2011), 1.4 cm of surface meltwater a day, or 5.11 m/ year was proposed as the threshold above which summer ice flow rates are not longer correlated with surface melting, as confirmed by other authors (Joughin et al., 2013; Schoof, 2010). This might correspond with a transition between a continuous film flow (low melting) and discrete channelized flow (Fig. 2.3), the latter involving far less interaction with the overlying ice, as observed on alpine glaciers.



Figure 5.7: Satellite image (Google Earth, 2014) illustrating water abundance on the Central West Greenland ice surface across the area where the SEM was applied. Up north is the fast flowing Jakobshavn Glacier (red arrow).

The potential ϕ was interpolated from 1 km Bamber 2013 data, as used for the BWM applications (section 4). Also for these simulations, ϕ was set to zero for bare land and ocean. The runoff data used here were obtained from with a resolution of 10 km (Fig. 4.3b). For this study area, the runoff averages 1.48 m/year, not exceeding the critical 5.11 m/ year, but as this is not homogeneously distributed over time, channelized subglacial water flow might be present. In addition to runoff, basal melting constitutes an additional source of 0.052 m/year

on average in this region. An initial experiment using both a uniform and PDF potential gradient sampling, with a neighbourhood radius $r = 5$ km (Fig. 5.8). The network shows a realistic dendritic pattern with more pronounced convergence of flow paths in regions with a steep potential gradient, as seen near the Jakobshavn Glacier. This glacier, situated over a deep bedrock through, also attracts large amounts of water in BWM simulations. First, this was ascribed to surface meltwater drainage, but warm ocean water might play a more important role (Zwally et al., 2002; Holland et al., 2008).

Although uniform sampling provides a faster routine for selecting a flow direction, it cannot account for regions where multiple steep gradients exist, like rough sections near the edges of the ice sheet. Note also that potentials along the boundaries here are wrong due to interpolation errors, since the potential outside the ice sheet is not $= 0$ in reality.

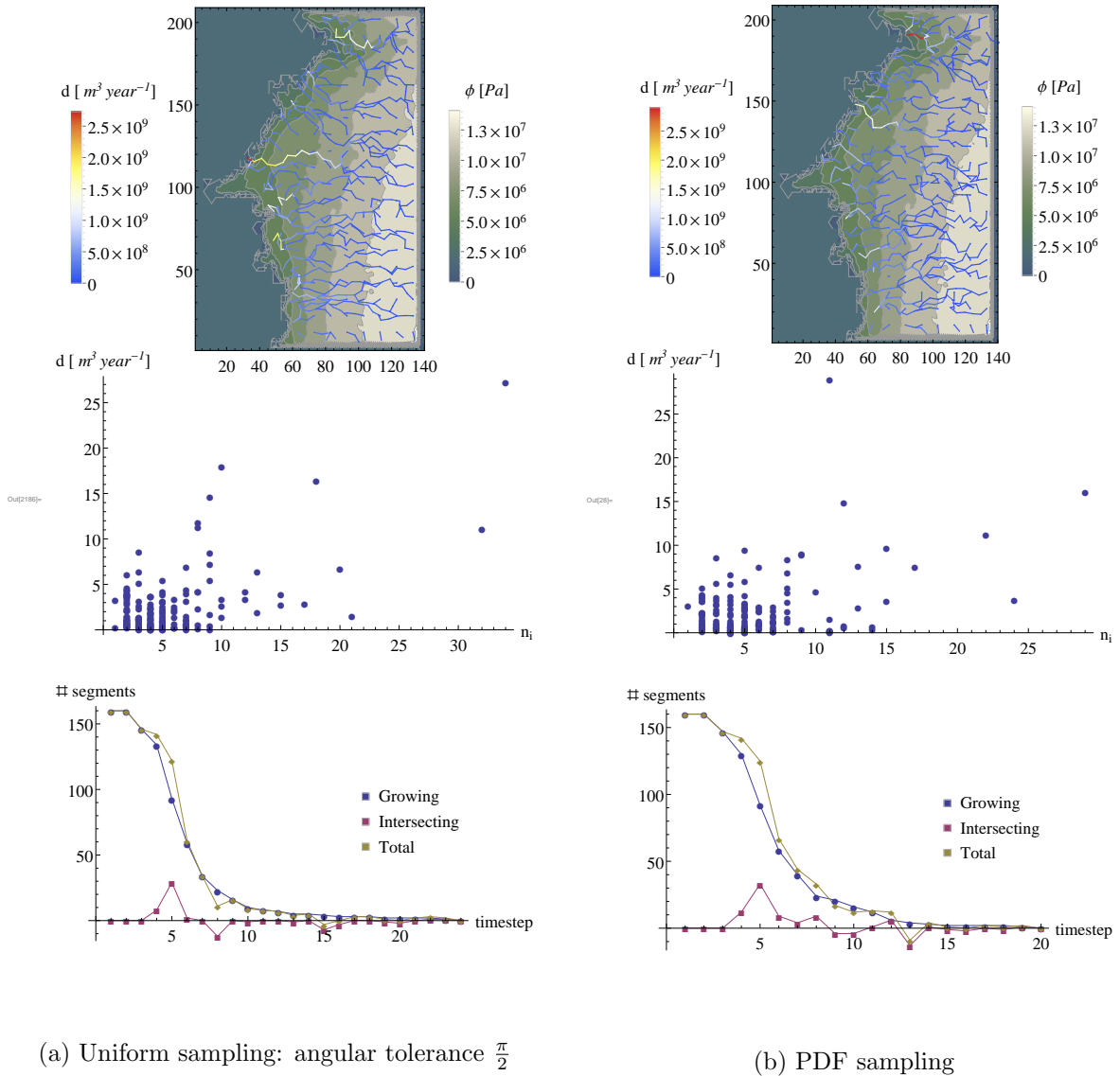


Figure 5.8: Central West Greenland, 10 km runoff fields, neighbourhood radius $r = 5$ km, different sampling algorithms. Above: steady-state network. Center: number of growing segments, changes in number of segments due to intersection and their sum (Total), representing the net number of segments added or deleted, versus time.

Also the effect of the radius is similar compared to the test configurations. As the radius decreases, channels again tend to behave more randomly in regions with smaller hydraulic potentials gradients. This might be an indication of longer residence time of the water under the ice sheet. Since the interpolated potential surface can contain depressions, the clusters could indicate zones susceptible to subglacial lake formation (Fig. 5.9).

Finally, the SEM output can be compared to the BWM output. For a realistic high 5 km

resolution runoff (Fig. 4.7b), the study area here to make comparisons (Fig. 5.10a). 1 km (Fig. 5.10b)

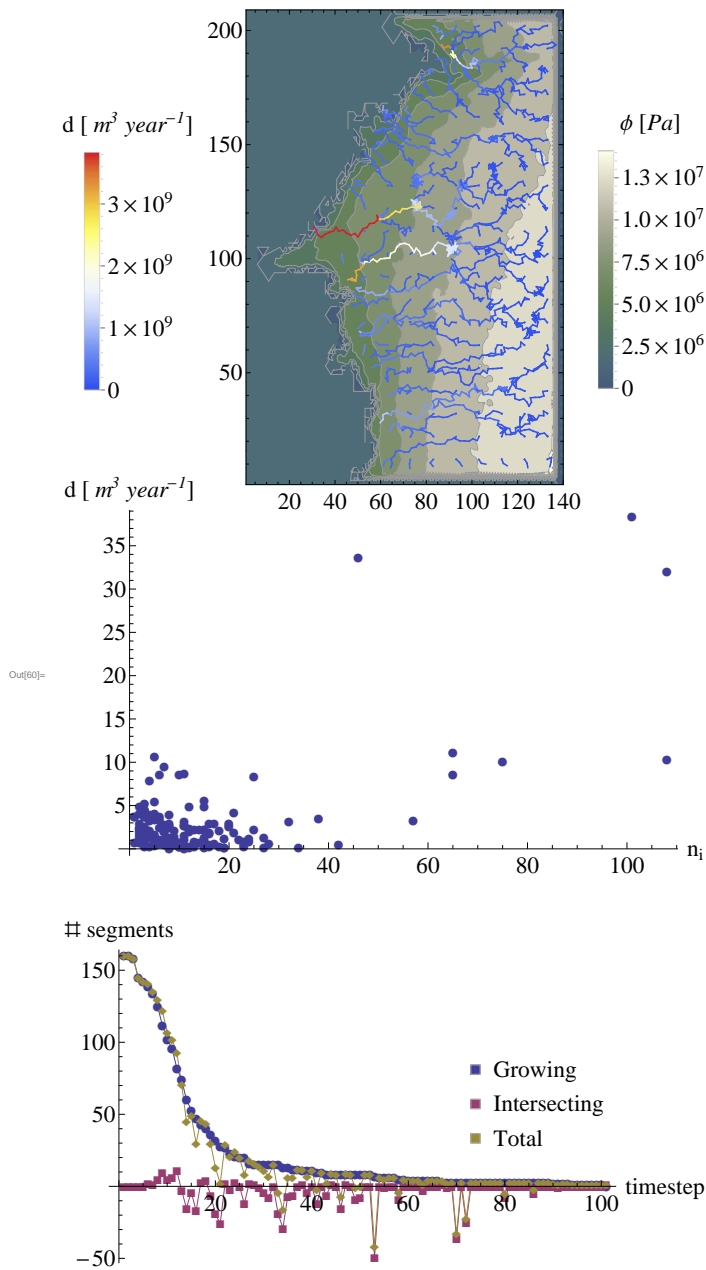


Figure 5.9: Central West Greenland, PDF sampling, 10 km runoff field, $r = 2$ km, SEM using 10 km runoff fields. Above: steady-state network. Center: number of growing segments, changes in number of segments due to intersection and their sum (Total), representing the net number of segments added or deleted, versus time.

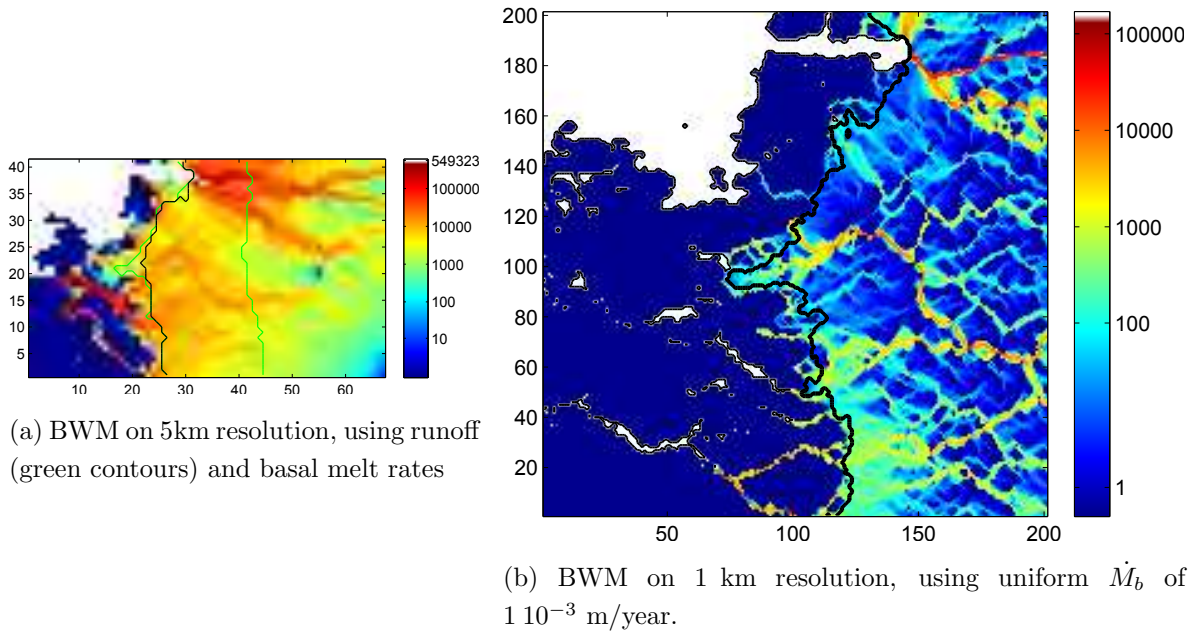


Figure 5.10: Central West Greenland, water flux Φ [$10^3 \text{ m}^3/\text{year}$]

CHAPTER 6

Discussion and outlook

This thesis has covered basal water flow under the Antarctic and Greenland ice sheets. Some common points of attention can be made, whereas the differences between both ice sheets also allow for some specific comments and suggestions. Lastly, for Greenland, the spatially explicit approach has proven to be promising.

6.1 Discussion

6.1.1 Weertman film approach and ISM coupling

For a large-scale modelling approach, the Weertman film assumptions are valid and might represent the easiest and most straightforward way of mimicking water fluxes under ice sheets. This also allows for velocities and film depths to be calculated, our focus here was mainly on the discharge of water. Since the ISM used here currently requires a resolution of at least 5km, there is no point in incorporating more spatial detail and elaborate physics when aiming at coupling the BWM and ISM. Below, some points of attention are suggested.

Hydraulic potential and depressions

When calculating the potential, it is important that the dataset has consistent ice thickness and floating. Further adaptations, like pre-filling depressions in the hydraulic potential, can be different depending on the application, which should always be kept in mind. When filled depressions are required, it might be useful to use a novel approach since this can prove computationally challenging. In the detection of subglacial lakes, the following can be concluded for the considered data fields:

- Bedrock elevation: determines the size and outline of potential subglacial lakes, making them more abundant and smaller with increasing resolution.

- Surface elevation: determines whether or not these depressions could be temporarily filled or not. Steeper ice surfaces cause steep potential gradients and consequently high water fluxes carrying the water out, with little lakes remaining.
- Basal melt rate/runoff: the presence of water will determine whether the hydraulic depressions are lakes or not. If no reliable estimate is available, or for experimental setups, a uniform water production rate can exclude local effects or uncertainties of these melt estimates.

Routing algorithm

An 8-cell approach can reproduce more realistic patterns irrespective of grid orientation. A choice can be made for allowing water flow under cold-based ice or not, which might reveal connections or relict pathways. When coupling the ISM and the BWM, it should be taken into account that water that can not enter these zones should be added as an accretion term to basal ice layers, and as such included in the ice continuity equation (Eq. 2.19).

Coupling with ice flow: since a Weertman film does not allow calculation of the basal water pressure P_w , other water flow variables could be used to enhance the amount of basal sliding and reproduce more accurate ice flow velocities, since very similar patterns can be observed. The lack of observations makes it difficult to validate the BWM output. However, more data are on the way, and coupling of the ISM and BWM could allow indirect validation by comparing with ice velocity fields, which are commonly found in literature.

6.1.2 Antarctica

A problem of the BWM resides in filling depressions at high resolutions. However, as potential lakes play a major role for the AIS, correct estimations are required for drilling programs and understanding ice dynamics. Although lakes outside basal melt zones might be considered irrelevant, they can be preserved and thus still affect ice flow. Basal accretion was calculated on several resolutions, and finally, sensitivity towards ISM input was examined again for higher resolutions.

6.1.3 Greenland

Lakes are not abundant under Greenland, although their number tends to increase with resolution. Observed lakes are fewer, smaller, and rare under the main GrIS or in a water production zone. The location and the penetration of runoff through the ice to the bed is still largely uncertain, and the output fields from the ISM only provide a rough estimate of the routing of this water to the ocean. Even more than for the AIS, it should be kept in mind on which geometries the basal melt and runoff fields are based. Here, runoff was based on

observed geometries whilst basal melt is simulated and thus based on ISM output geometries. Considering the amount of water released as runoff through surface melting is up to 10 times higher when compared to basal formed meltwater, it is important to distinguish between basal melt and runoff. Moreover, runoff influences ice dynamics on a timescale of weeks, so coupling this field to yearly steady-state ISM simulations might lead to false conclusions. For basal meltwater, a coupling similar to the AIS might be set up.

6.1.4 Spatially explicit model: a new approach to channelized subglacial water flow?

Large uncertainties surround basal water flow on a continental scale, ranging from input data over routing and resolution effects, to a lack of validation data. A stochastic and SEM might give a different view on basal hydrology.

- Model setup: network formation has been a commonly discussed topic in hydrology and other disciplines. Although a few problems were identified, the SEM has shown to produce qualitatively meaningful results.
- Tests and applications: after elaborate debugging, consistent results were obtained for test geometries. When applied to a realistic case in Central West Greenland, this fairly simple approach produced realistic water routing and concentration patterns.
- Outlook: When comparing the channel model with the physics of channelized subglacial water flow, it is clear that a lot of improvements are possible.

The lack of treating intra-channel intersections should be solved, possibly by using the formed path clusters as a means to heighten the potential locally, similar to filling depressions, to ensure outflow.

The constant radius r (and associated segment length) could be replaced by a gradient- or discharge dependent radius. In the first case, steep gradients, producing high water fluxes and rapid channel melting, should cause channels to grow faster. Low-gradient regions with low flow would only grow slowly, requiring smaller radii. Another possibility could be directly linking discharge (and thus channel melting rate). This channel melting in its turn could eventually be coupled with overlying ice closing the channel through deformation. In this way, the SEM could become a physically-based model for subglacial channelized flow.

Bibliography

- Åström, J. A., Riikilä, T. I., Tallinen, T., Zwinger, T., Benn, D., Moore, J. C., and Timonen, J. (2013). A particle based simulation model for glacier dynamics. *The Cryosphere Discussions*, 7:921–941.
- Abermann, J., Lambrecht, A., Fischer, A., and Kuhn, M. (2009). Quantifying changes and trends in glacier area and volume in the Austrian Otztal Alps (1969-1997-2006). *The Cryosphere*, 3:205–215.
- Baetens, J. M. (2012). *Discrete spatio-temporal modelling paradigms for environmental processes: SWOT analysis, application portfolio and Lyapunovian stability analysis*. Phd thesis, Ghent University.
- Bamber, J. L., Griggs, J. A., Hurkmans, R. T. W. L., Dowdeswell, J. A., Gogineni, S. P., Howat, I., Mouginot, J., Paden, J., Palmer, S., Rignot, E., and Steinhage, D. (2013a). A new bed elevation dataset for Greenland. *The Cryosphere*, 7:499–510.
- Bamber, J. L., Siegert, M. J., Griggs, J. a., Marshall, S. J., and Spada, G. (2013b). Paleofluvial Mega-Canyon Beneath the Central Greenland Ice Sheet. *Science*, 341:997–999.
- Bell, R. E. (2008). The role of subglacial water in ice-sheet mass balance. *Nature Geoscience*, 1:297–304.
- Bell, R. E., Studinger, M., Shuman, C. A., Fahnestock, M. A., and Joughin, I. (2007). Large subglacial lakes in East Antarctica at the onset of fast-flowing ice streams. *Nature*, 445:904–907.
- Bell, R. E., Studinger, M., Tikku, A. A., Clarke, G. K. C., Gutner, M. M., and Meertens, C. (2002). Origin and fate of Lake Vostok water frozen to the base of the East Antarctic ice sheet. *Nature*, 416:307–310.
- Clarke, G. K. (2005). Subglacial Processes. *Annual Review of Earth and Planetary Sciences*, 33:247–276.

- Creyts, T. T. and Schoof, C. G. (2009). Drainage through subglacial water sheets. *Journal of Geophysical Research*, 114:2156–2202.
- Cuffey, K. M. and Paterson, W. S. B. (2006). *The physics of glaciers*. Academic Press, Chippenham, 4 edition.
- Devroye, L. (1986). *Non- uniform random variate generation*. Springer-Verlag, New York.
- Flowers, G. E. (2002). A multicomponent coupled model of glacier hydrology 1. Theory and synthetic examples. *Journal of Geophysical Research*, 107:9–17.
- Fretwell, P., Pritchard, H. D., Vaughan, D. G., Bamber, J. L., Barrand, N. E., Bell, R., Bianchi, C., Bingham, R. G., Blankenship, D. D., Casassa, G., Catania, G., Callens, D., Conway, H., Cook, A. J., Corr, H. F. J., Damaske, D., Damm, V., Ferraccioli, F., Forsberg, R., Fujita, S., Gim, Y., Gogineni, P., Griggs, J. A., Hindmarsh, R. C. A., Holmlund, P., Holt, J. W., Jacobel, R. W., Jenkins, A., Jokat, W., Jordan, T., King, E. C., Kohler, J., Krabill, W., Riger-Kusk, M., Langley, K. A., Leitchenkov, G., Leuschen, C., Luyendyk, B. P., Matsuoka, K., Mouginot, J., Nitsche, F. O., Nogi, Y., Nost, O. A., Popov, S. V., Rignot, E., Ripplin, D. M., Rivera, A., Roberts, J., Ross, N., Siegert, M. J., Smith, A. M., Steinhage, D., Studinger, M., Sun, B., Tinto, B. K., Welch, B. C., Wilson, D., Young, D. A., Xiangbin, C., and Zirizzotti, A. (2013). Bedmap2: improved ice bed, surface and thickness datasets for Antarctica. *The Cryosphere*, 7:375–393.
- Fudge, T. J., Harper, J. T., Humphrey, N. F., and Pfeffer, W. T. (2009). Rapid glacier sliding, reverse ice motion and subglacial water pressure during an autumn rainstorm. *Annals of Glaciology*, 50:101–108.
- Fürst, J. (2013). *No Title*. PhD thesis, Vrije Universiteit Brussel.
- Goelzer, H., Huybrechts, P., Fürst, J., Nick, F., Andersen, M., Edwards, T., Fettweis, X., Payne, A., and Shannon, S. (2013). Sensitivity of Greenland ice sheet projections to model formulations. *Journal of Glaciology*, 59:733–749.
- Grimm, V. and Railsback, S. F. (2013). *Individual-based modeling and ecology*. Princeton University Press, Princeton, New Jersey, 1 edition.
- Gudmundsson, G. H., Krug, J., Durand, G., Favier, L., and Gagliardini, O. (2012). The stability of grounding lines on retrograde slopes. *The Cryosphere*, 6:1497–1505.
- Hafver, A., Jettestuen, E., Baetens, J. M., and Malthe-sørensen, A. (2014). Network Formation by Contact Arrested Propagation. *Physica A*, submitted:/.
- Harper, J. T., Humphrey, N. F., Pfeffer, W. T., Fudge, T., and O’Neel, S. (2005). Evolution of subglacial water pressure along a glacier’s length. *Annals of Glaciology*, 40:31–36.

- Holland, D. M., Thomas, R. H., de Young, B., Ribergaard, M. H., and Lyberth, B. (2008). Acceleration of Jakobshavn Isbræt triggered by warm subsurface ocean waters. *Nature Geoscience*, 1:659–664.
- Huybrechts, P. (1986). A three-dimensional time-dependent numerical model for polar ice sheets: some basic testing with a stable efficient finite difference scheme. Technical report, Geografisch Instituut, VUB.
- Huybrechts, P. (2002). Sea-level changes at the LGM from ice-dynamic reconstructions of the Greenland and Antarctic ice sheets during the glacial cycles. *Quaternary Science Reviews*, 21:203–231.
- Huybrechts, P. and De Wolde, J. (1999). The dynamic response of the Greenland and Antarctic ice sheets to multiple-century climatic warming. *Journal of Climate*, 12:2169–2188.
- Huybrechts, P., Payne, T. (1996). the EISMINT benchmarks for testing ice-sheet models. *Annals of Glaciology*, 23:1–12.
- IPCC (2013). Working group I contribution to the IPCC Fifth Assessment Report Climate Change 2013: the physical science basis, Final Draft Underlying Scientific-Technical Assessment A report accepted by Working Group I of the IPCC but not approved in detail . Technical report, Intergovernmental Panel on Climate Change.
- Irvine-Fynn, T. D. L., Hodson, A. J., Moorman, B. J., Vatne, G., and Hubbard, A. L. (2011). Polythermal glacier hydrology: a review. *Reviews of geophysics*, 49.
- Johnson, J. V. (2002). *A basal water model for ice sheets*. Phd thesis, B.S. University of Minnesota.
- Joughin, I., Das, S. B., Flowers, G. E., Behn, M. D., Alley, R. B., King, M. A., Smith, B. E., Bamber, J., van den Broeke, M. R., and van Angelen, J. H. (2013). Influence of supraglacial lakes and ice-sheet geometry on seasonal ice-flow variability. *The Cryosphere Discussions*, 7:1101–1118.
- Joughin, I., Das, S. B., King, M. A., Smith, B. E., Howat, I. M., and Moon, T. (2008). Seasonal speedup along the western flank of the Greenland Ice Sheet. *Science*, 320:781–783.
- Joughin, I., Smith, B. E., and Medley, B. (2014). Marine Ice Sheet Collapse Potentially Underway for the Thwaites Glacier Basin, West Antarctica. *Science (New York, N.Y.)*, 344:735–738.
- Keisling, B., Christianson, K., Alley, R., Peters, L., Christian, J., Anandakrishnan, S., Riverman, K. L., Muto, A., and Jacobel, R. W. (2013). Basal conditions and ice dynamics inferred from radar-derived internal stratigraphy of the Northeast Greenland Ice Stream. *AGU Fall Meeting Abstracts*, page /.

- Kohler, J. (2007). Glaciology - Lubricating lakes. *Nature*, 445:830–831.
- Le Brocq, A. M., Payne, A. J., and Siegert, M. J. (2006). West Antarctic balance calculations: Impact of flux-routing algorithm, smoothing algorithm and topography. *Computers & Geosciences*, 32:1780–1795.
- Le Brocq, A. M., Payne, A. J., Siegert, M. J., and Alley, R. B. (2009). A subglacial water-flow model for West Antarctica. *Journal of Glaciology*, 55:879–888.
- Le Brocq, A. M., Ross, N., Griggs, J. a., Bingham, R. G., Corr, H. F. J., Ferraccioli, F., Jenkins, A., Jordan, T. a., Payne, A. J., Rippin, D. M., and Siegert, M. J. (2013). Evidence from ice shelves for channelized meltwater flow beneath the Antarctic Ice Sheet. *Nature Geoscience*, 6:1–4.
- Lenaerts, J. T. M., van Angelen, J. H., van den Broeke, M. R., Gardner, A. S., Wouters, B., and van Meijgaard, E. (2013). Irreversible mass loss of Canadian Arctic Archipelago glaciers. *Geophysical Research Letters*, 40:870–874.
- Lewis, A. R., Marchant, D. R., Kowalewski, D. E., Baldwin, S. L., and Webb, L. E. (2006). The age and origin of the Labyrinth, western Dry Valleys, Antarctica: Evidence for extensive middle Miocene subglacial floods and freshwater discharge to the Southern Ocean. *Geology*, 34:513–516.
- Ligtenberg, S. R. M., Helsen, M. M., and van den Broeke, M. R. (2011). An improved semi-empirical model for the densification of Antarctic firn. *The Cryosphere*, 5:809–819.
- Livingstone, S. J., Clark, C. D., and Woodward, J. (2013). Predicting subglacial lakes and meltwater drainage pathways beneath the Antarctic and Greenland ice sheets. *The Cryosphere Discussions*, 7:1177–1213.
- Lough, A. C., Wiens, D. A., Grace Barcheck, C., Anandakrishnan, S., Aster, R. C., Blankenship, D. D., Huerta, A. D., Nyblade, A., Young, D. A., and Wilson, T. J. (2013). Seismic detection of an active subglacial magmatic complex in Marie Byrd Land, Antarctica. *Nature Geoscience*, 6:1031–1035.
- Magnusson, E., Rott, H., Bjornsson, H., and Palsson, F. (2007). The impact of jokulhlaups on basal sliding observed by SAR interferometry on Vatnajokull, Iceland. *Journal of Glaciology*, 53:232–240.
- Mair, D., Nienow, P., Sharp, M., Wohlleben, T., and Willis, I. (2002). Influence of subglacial drainage system evolution on glacier surface motion: Haut Glacier d’Arolla, Switzerland. *Journal of Geophysical Research: Solid Earth*, 107:1–13.
- Marcott, S. A., Jeremy, D., Shakun, J. D., and Clark, P. U. (2013). A Reconstruction of Regional and Global Temperature for the Past 11,300 Years. *Science*, 339:1198–1201.

- Marshall, S. J. (2011). *The cryosphere*. Princeton University Press.
- McMillan, M., Shepherd, A., Sundal, A., Briggs, K., Muir, A., Ridout, A., Hogg, A., and Wingham, D. (2014). Increased ice losses from Antarctica detected by CryoSat-2. *Geophysical Research Letters*, (accepted):/.
- Palmer, S. J., Dowdeswell, J. a., Christoffersen, P., Young, D. a., Blankenship, D. D., Greenbaum, J. S., Benham, T., Bamber, J., and Siegert, M. J. (2013). Greenland subglacial lakes detected by radar. *Geophysical Research Letters*, 40:6154–6159.
- Pattyn, F., Perichon, L., Aschwanden, A., Breuer, B., de Smedt, B., Gagliardini, O., Gudmundsson, G. H., Hindmarsh, R. C. a., Hubbard, A., Johnson, J. V., Kleiner, T., Konovalov, Y., Martin, C., Payne, a. J., Pollard, D., Price, S., Rückamp, M., Saito, F., Souček, O., Sugiyama, S., and Zwinger, T. (2008). Benchmark experiments for higher-order and full-Stokes ice sheet models (ISMIPHOM). *The Cryosphere*, 2:95–108.
- Payne, A., Huybrechts, P., Abe-Ouchi, A., Calov, R., Fastook, J. L., Greve, R., Marshall, S. J., Marsiat, I., Ritz, C., Tarasov, L., and Thomassen, M. P. a. (2000). Results from the EISMINT model intercomparison: the effects of thermomechanical coupling. *Journal of Glaciology*, 46:227–238.
- Pimentel, S., Flowers, G. E., and Schoof, C. G. (2010). A hydrologically coupled higher-order flow-band model of ice dynamics with a Coulomb friction sliding law. *Journal of Geophysical Research*, 115:2003–2012.
- Planchon, O. (2002). A fast , simple and versatile algorithm to fill the depressions of digital elevation models. *Catena*, 46:159–176.
- Pritchard, H. D., Arthern, R. J., Vaughan, D. G., and Edwards, L. A. (2009). Extensive dynamic thinning on the margins of the Greenland and Antarctic ice sheets. *Nature*, 461:971–975.
- Pritchard, H. D., Ligtenberg, S. R. M., Fricker, H. A., Vaughan, D. G., van den Broeke, M. R., and Padman, L. (2012). Antarctic ice-sheet loss driven by basal melting of ice shelves. *Nature*, 484:502–505.
- Rignot, E. and Mouginot, J. (2012). Ice flow in Greenland for the International Polar Year 2008-2009. *Geophysical Research Letters*, 39:1–7.
- Rignot, E., Mouginot, J., Morlighem, M., Seroussi, H., and Scheuchl, B. (2014). Widespread, rapid grounding line retreat of Pine Island, Thwaites, Smith, and Kohler glaciers, West Antarctica, from 1992 to 2011. *Geophysical Research Letters*, 41:/.
- Rignot, E., Mouginot, J., and Scheuchl, B. (2011). Ice flow of the Antarctic ice sheet. *Science (New York, N.Y.)*, 333:1427–1430.

- Rignot, E. and Thomas, R. H. (2002). Mass balance of polar ice sheets. *Science*, 297:1502–1506.
- Schoof, C. (2010). Ice-sheet acceleration driven by melt supply variability. *Nature*, 468:803–806.
- Shreve, R. (1972). Movement of water in glaciers. *Journal of Glaciology*, 11:205–214.
- Siegert, M. J. (2008). Antarctic subglacial topography and ice-sheet evolution. *Earth Surface Processes and Landforms*, 33:646–660.
- Sundal, A. V., Shepherd, A., Nienow, P., Hanna, E., Palmer, S., and Huybrechts, P. (2011). Melt-induced speed-up of Greenland ice sheet offset by efficient subglacial drainage. *Nature*, 469:521–524.
- van de Wal, R. S. W., Boot, W., van den Broeke, M. R., Smeets, C. J. P. P., Reijmer, C. H., Donker, J. J. a., and Oerlemans, J. (2008). Large and rapid melt-induced velocity changes in the ablation zone of the Greenland Ice Sheet. *Science (New York, N.Y.)*, 321(5885):111–113.
- van den Broeke, M., Bamber, J., Ettema, J., Rignot, E., Schrama, E., van de Berg, W. J., van Meijgaard, E., Velicogna, I., and Wouters, B. (2009). Partitioning recent Greenland mass loss. *Science*, 326:984–6.
- Van der Veen, C. (2013). *Fundamentals of glacier dynamics*. CRC Press, Boca Raton, 2 edition.
- Vanderstocken, T. (2010). *Determination of the routing of basal water under the Antarctic ice sheet and its meaning in the formation of subglacial lakes and the processes of basal sliding*. PhD thesis, Katholieke Universiteit Leuven.
- Vaughan, D. G. and Arthern, R. (2007). Climate change. Why is it hard to predict the future of ice sheets? *Science*, 315:1503–1504.
- Wang, L. and Liu, H. (2006). An efficient method for identifying and filling surface depressions in digital elevation models for hydrologic analysis and modelling. *International Journal of Geographical Information Science*, 20:193–213.
- Wel, N. V. D., Christoffersen, P., and Bougamont, M. (2012). The influence of subglacial hydrology on the flow of Kamb Ice Stream , West Antarctica. *Journal of Geophysical Research: Earth Surface*, 118:97–110.
- Wingham, D. J., Siegert, M. J., Shepherd, A., and Muir, A. S. (2006). Rapid discharge connects Antarctic subglacial lakes. *Nature*, 440:1033–1036.

Wright, A. and Siegert, M. J. (2012). A fourth inventory of Antarctic subglacial lakes. *Antarctic Science*, 24:659–664.

Zwally, H. J., Abdalati, W., Herring, T., Larson, K., Saba, J., and Steffen, K. (2002). Surface melt-induced acceleration of Greenland ice-sheet flow. *Science*, 297:218–22.